University of Southampton

National Oceanography Centre

Mechanisms of ocean carbon cycle variability in the 21st Century

Thesis for the degree of Doctor of Philosophy

Author:
Matthew Peter Couldrey

Supervisors:
Kevin Oliver, Andrew Yool, Eric Achterberg and Paul Halloran

12th March 2018

UNIVERSITY OF SOUTHAMPTON

ABSTRACT

FACULTY OF NATURAL AND ENVIRONMENTAL SCIENCES

Ocean and Earth Sciences

National Oceanography Centre

Doctor of Philosophy

MECHANISMS OF OCEAN CARBON CYCLE VARIABILITY IN THE 21ST CENTURY

by Matthew Couldrey

The ocean is an enormous and variable sink of carbon dioxide gas (CO_2) for the atmosphere, and a detailed knowledge of the drivers of uptake variability is needed to predict future climate change. Here, a leading-edge ocean computer model is used to attribute 21st Century ocean carbon cycle variability to underlying causal physical, chemical, and biological mechanisms.

First, North Atlantic carbon flux variability across a range of timescales is attributed to each component of the flux equation: the air-sea concentration gradient (the difference of partial pressures, ΔpCO_2), the gas transfer velocity (which quantifies how environmental factors e.g. wind enhance gas exchange, k), and the solubility coefficient (which quantifies how temperature and salinity affect gas dissolution, α). Both ΔpCO_2 and k are strong controls on interannual flux variability, but the longer decadal and multidecadal changes are dominated by just ΔpCO_2.

Next, the drivers of North Atlantic Dissolved Inorganic Carbon (DIC) inventory changes are identified. Interannual variations in temperature and preformed alkalinity cause almost all the basin's year-to-year DIC fluctuations. Decadal variability is attributed to saturation and anthropogenic carbon forcing. Multidecadal cycles and the trend up to the year 2100 are dominated by anthropogenic carbon uptake.

Finally, the global DIC inventory variance is quantified, highlighting Pacific upwelling of remineralised carbon as the main driver of interannual variability. Anthropogenic carbon is the largest single contributor to variability on longer timescales up to 2100, with other processes playing secondary or negligible roles.

Contents

List of Tables

List of Figures

Academic Thesis: Declaration Of Authorship

I, Matthew Couldrey, declare that this thesis and the work presented in it are my own and has been generated by me as the result of my own original research.

I confirm that:

1. This work was done wholly or mainly while in candidature for a research degree at this University;

.

2. Where any part of this thesis has previously been submitted for a degree or any other qualification at this University or any other institution, this has been clearly stated;

3. Where I have consulted the published work of others, this is always clearly attributed;

4. Where I have quoted from the work of others, the source is always given. With the exception of such quotations, this thesis is entirely my own work;

5. I have acknowledged all main sources of help;

6. Where the thesis is based on work done by myself jointly with others, I have made clear exactly what was done by others and what I have contributed myself;

7. Either none of this work has been published before submission, or parts of this work have been published as:
   Couldrey, M. P., K. I. Oliver, A. Yool, P. R. Halloran, and E. P. Achterberg, On which timescales do gas transfer velocities control North Atlantic CO_2 flux variability?, *Global Biogeochemical Cycles*, *30*(5), 787-802, 2016.

Signed:_____

Date:_____

Acknowledgements

Certainly, the scientific output of any individual is the product of an enormous network of support, and in my own case this is especially true. The production of this thesis has been expertly guided by my tremendously talented, inspiring and nurturing supervisors; Kevin Oliver, Andrew Yool, Paul Halloran and Eric Achterberg. At every step of the way, they have always enthusiastically offered assistance and inspiration through every success and struggle. I am unspeakably grateful to have had the privilege of being their student. My examiners, Dorothee Bakker and Bablu Sinha have earned enormous credit for their thoughtful and thorough examination of this thesis. Their sharp enquiries made for a stimulating *viva*, and I am very grateful that this thesis has benefitted from their insight. The guiding hand of my supervisory panel chair, Brian King, has been an important force in supporting this project and ensuring its effective management. Brian King is also owed additional acknowledgement for the incredible experience of open ocean scientific fieldwork aboard the RRS *Discovery* (DY040 2015/2016 RAPID/RAGNARoCC/ABCFluxes cruise) during which he showed an additional side of himself as a fantastic PI. The work described in this thesis draws upon an enormous breadth of observations and model output, and so I very gratefully acknowledge the incalculable efforts taken by all the data collectors, field scientists, technicians, ship crews, volunteers, quality controllers, software developers, archivists, publishers, model developers, IT staff and countless others who have made this wealth of resources available.

My studentship, in particular, has been incalculably enriched by being a part of the RAGNARoCC Project: I acknowledge with enormous gratitude the generous financial support of NERC that has made this thesis possible (NE/K002546/1). But beyond the very clearly critical financial support that RAGNARoCC has provided, I cannot overstate how valuable it has been to work alongside the other

members of the RAGNARoCC project across countless institutions. RAGNARoCC has provided me with a forum to grow as an early career scientist with some of the country's most esteemed and talented scientists in the field and I have greatly enjoyed being a part of such an important project. Scientific discussions with Andy Watson, Pete Brown, Alice Lebehot, Tobia Tudino, Ute Schuster, Matthew Humphreys, Elaine McDonagh, Claire Winder, Marie Jose Messias, Ian Totterdell, Nick Bates, Richard Sanders, Margaret Yelland, Liz Kent, and everyone else in the RAGNARoCC/ABCFluxes/GAUGE/GREENHOUSE community have had a huge positive impact on my studentship, and I have been continually inspired by their successes. As if this were not enough, I have also been incredibly fortunate to have benefitted from the DY040 Cruise and 2015 Summer School, both made possible through RAGNARoCC.

In a similar vein, the National Oceanography Centre, Southampton has been a fantastically nurturing environment to be a postgraduate student, and I have been fortunate to study in such a bustling ocean research institute. NOCS has provided me with a network of scientists across many oceanographic disciplines, as well as a peerless group of friends. I must name my office-mates Helen Burns and Zoe Jacobs, who have supported me through something on the order of five thousand hours of office life, as well as being dear friends. Everyone on the 256 Modelling corridor has assisted in the work that underlies this thesis in one way or another, but additional thanks are owed to Andrew Coward and Adam Blaker for their help. I am especially grateful to Jeff Blundell, whose guidance through the morass of supercomputering has been nothing short of sage-like.

With tremendous love, my family have also generously supported my study, and they absolutely are owed credit for the production of this work. That their many and generous contributions have not been scientific or technical detracts neither from their value, nor their worthiness to be acknowledged here. Lastly, I acknowledge Amelia Astley, who has given so much patience, support and inspiration through every single success and hardship of my studentship.

I should certainly not have undertaken these tedious calculations if an extraordinary interest had not been connected with them.

Svante August Arrhenius "On the influence of Carbonic Acid in the Air Upon the Temperature of the Ground", *Philosophical Magazine and Journal of Science*, 1896

Glossary

AMOC

Atlantic Meridional Overturning Circulation.

AOU

Apparent Oxygen Utilisation.

$CaCO_3$

calcium carbonate.

CCD

Carbonate Compensation Depth.

DIC

Dissolved Inorganic Carbon.

DIN

Dissolved Inorganic Nitrogen.

DOC

Dissolved Organic Carbon.

ENSO

El Niño-Southern Oscillation.

GCM

General Circulation Model.

GIN

Greenland-Iceland-Norwegian.

GLODAP

Global Ocean Data Analysis Project.

IPCC

Intergovernmental Panel on Climate Change.

MEDUSA

Model of Ecosystem Dynamics, Utilisation, Sequestration and Acidification.

NAC

North Atlantic Current.

NEMO

Nucleus for European Modelling of the Ocean.

NPZD

Nutrient-Phytoplankton-Zooplankton-Detritus.

ppm

parts per million in moles; μmol mol^{-1}.

RMS

root-mean-square.

SOCAT

Surface Ocean CO_2 Atlas.

SSS

Sea Surface Salinity.

SST

Sea Surface Temperature.

List of Symbols

Non-alphabetical

$'$	Prime, denotes deviation from long term mean
$^-$	Overline, denotes long term mean
[ ]	Concentration, molar
$^\circ$	Degree (of latitude or temperature)

Greek Alphabetical

α	Henry's coefficient of solubility, mol $m^{-3}\mu atm^{-1}$
β	Regression slope or partial differential
Δ	Finite difference
ΔpCO_2	Air-Sea CO_2 partial pressure difference, μatm^{-1}
Σ	Sum
σ	Standard deviation, also density anomaly from reference density
τ	Relaxation timescale

Latin Alphabetical

A_T	Total alkalinity, the sum of bases in solution, expressed as equivalents μeq kg^{-1}
atm	Atmospheres of pressure, 1 atm = 1.01325 bar
C	Carbon (elemental) or Concentration of dissolved inorganic carbon
CE	Common Era
D	Destruction of soft tissue carbon by ventilation (gC yr^{-1})
F	CO_2 air to sea gas flux
f	Fugacity

$f_n()$	Running mean filter with an n year window size
fft	Fast Fourier Transform
H	Horizontal advection of soft tissue carbon (gC yr^{-1})
k	Gas transfer velocity, m d^{-1}
m	Metres
mol	moles, amount of a substance
p	potential of a chemical (e.g. Hydrogen, pH), $-\log_{10}()$
p	Partial pressure of a gas in mixture, also probability in hypothesis testing (i.e. p-value)
PgC	Petagrams (10^{15}g) of Carbon
R	Redfield stoichiometric ratio of elements
r	Pearson correlation coefficient
S	Salinity, practical as (*McDougall and Barker*, 2011), unitless
s	seconds
Sv	Sverdrup, water volume transport 1 Sv = $10^6 m^3 s^{-1}$
T	Temperature, °C
t	time
Tr	Generic tracer concentration, molar
X_{CO_2}	Mixing ratio of CO_2 in the atmosphere
yr	Year
z	Depth, metres below sea surface

Chapter 1

The Carbon Cycle and the Ocean

1.1 Carbon and Earth's Climate

The carbon cycle is the name given to the dynamic system of exchanges of carbon through four planetary reservoirs; the atmosphere, ocean, terrestrial biosphere and lithosphere. The distribution of carbon between these four reservoirs forms a critical control on Earth's climate, chiefly because the amount of carbon in the atmosphere is a major factor determining the planetary radiative balance via the 'greenhouse effect'. Broadly, the sun radiates energy at short wavelengths (visible and near-visible) onto the Earth, one third of which is reflected off the atmosphere while most of the remainder is absorbed by the planet's surface; the atmosphere does not absorb much energy at these short wavelengths. The land and oceans re-emit most of the absorbed energy at longer wavelengths (infrared); some of which goes out into space and some is absorbed by the atmosphere. The amount of this outgoing energy that is absorbed by the atmosphere is therefore a crucial component of the climate system that sets the planet's surface temperature. The concentration of 'greenhouse gases' in the atmosphere (namely carbon dioxide, CO_2, methane, CH_4, nitrous oxide, N_2O, and water vapour) is thought to govern how much of the outgoing longwave radiation is absorbed by the planet (*Solomon et al.*, 2007; *Etminan et al.*, 2016). Over the past half century of climate science, carbon dioxide has been given vastly more scientific attention than the other greenhouse gases, but readers are reminded of the growing understanding of the crucial importance that non-CO_2 greenhouse gases have for Earth climate (*Ciais et al.*, 2013). However, the focus of this thesis is entirely on the role of carbon in the climate

system, and so other the other greenhouse gases and their relevant biogeochemical cycles will not be discussed further here.

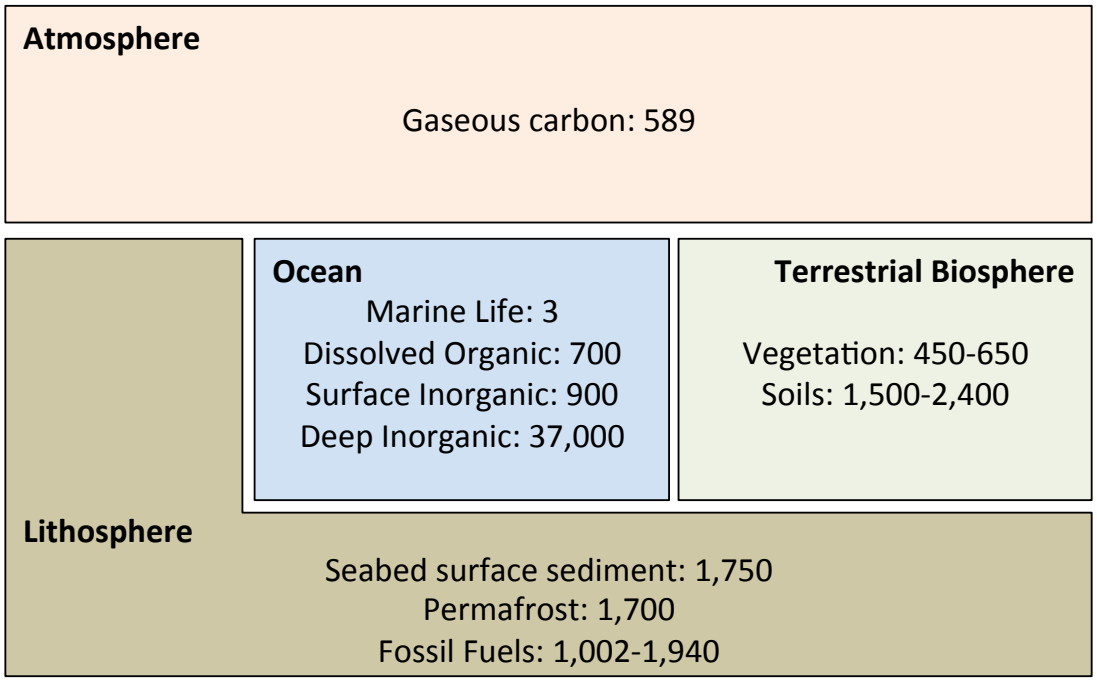

Figure 1.1: Sizes of the major preindustrial reservoirs carbon in PgC relevant to the carbon cycle on annual to multicennial timescales (1 PgC = 10^{15}gC), redrawn from (*Ciais et al.*, 2013)

In the natural climate system (i.e. before the industrial revolution in the 17$^{\text{th}}$ Century CE), the concentration of CO_2 in the atmosphere varies through geological time because fluxes exist between the other carbon reservoirs that operate on all timescales (from instantaneous to multi-millenial). Before these fluxes can be discussed, it is first helpful to briefly explore the nature of these four reservoirs in the context of the most recent interglacial period, Figure 1.1. 11,700 years ago, when the last glacial period came to an end (*Rasmussen et al.*, 2006), the Earth's climate through the ensuing Holocene epoch is estimated to have been relatively stable in comparison with glacial-interglacial variations (*Jouzel et al.*, 2007). Over the same period, palaeoclimate records indicate that the mole fraction of atmospheric carbon also showed relative stability, varying between 260-285 parts per million in moles; μmol mol^{-1} (ppm) (*Lüthi et al.*, 2008). While not known, a reasonable hypothesis is that the partitioning of carbon between the atmosphere and the other three reservoirs was approximately stable through this same period (i.e. that the carbon fluxes between them approximately balance).

The preindustrial interglacial atmosphere holds the least carbon of the four, bearing about 589 PgC as gaseous carbon dioxide. This inventory of CO_2 equates to a concentration of approximately 278 ppm, assuming 2.12 PgC ppm^{-1} (*Prather et al.*, 2012). Modern satellite-based observations of atmospheric column inventories of carbon across the entire globe show that concentrations are spatially similar to a few ppm (*Eldering et al.*, 2017). Atmospheric CO_2 concentrations are therefore relatively quickly homogenised by meteorological processes on timescales of about year, in stark contrast to the other three reservoirs. The terrestrial biosphere describes the carbon held by land vegetation (450-650 PgC) and soils (1500-2400 PgC). Note that the spread of estimates of carbon held in soils is larger than the entire atmospheric carbon store, and reflects crucial gaps in our understanding of the global carbon cycle. The world's freshwaters are included in the 'terrestrial biosphere', but comprise a very small portion of this budget. Relevant to climate science over past 200 or so years, the preindustrial lithosphere is thought to have held approximately 4,700 PgC with roughly equal portions frozen in permafrost, held in fossil fuel reserves (as coal, gas and oil), and seabed surface sediments. These oceanic surface sediments consist mostly of the pool of 1600 PgC of calcium carbonate ($CaCO_3$) that is able to chemically communicate with overlying water (*Archer et al.*, 1998) as well as a smaller pool of 150 PgC of organic carbon (*Emerson and Hedges*, 1988). The final, largest reservoir of carbon relevant to century-scale carbon cycling is the global ocean, holding about 38,000 PgC.

The vast majority of oceanic carbon exists as Dissolved Inorganic Carbon (DIC) and is stored in the deep ocean. Therefore, the length of time for which most of the ocean's carbon may remain sequestered in this reservoir is on the same order as the ventilation timescale of the global ocean; about 5000 years (*England*, 1995). The upper ocean, which communicates with the atmosphere on instantaneous to multiannual timescales, holds about 900 PgC of dissolved inorganic carbon. There is also a pool of 700 PgC of organic carbon dissolved in the global ocean that is cycled on approximately 1,000 year timescales (*Hansell et al.*, 2009). Note that living carbon in the ocean is two orders of magnitude smaller than on land.

It is thought that the partitioning of carbon between these reservoirs is dynamically linked to Earth's climate through a combination of causality and feedbacks.

Clearly, these carbon reservoirs are connected by biogeochemical processes that flux matter between them, and throughout Earth's history the balance (and imbalance) of those fluxes is closely linked to stability and changes in climate.

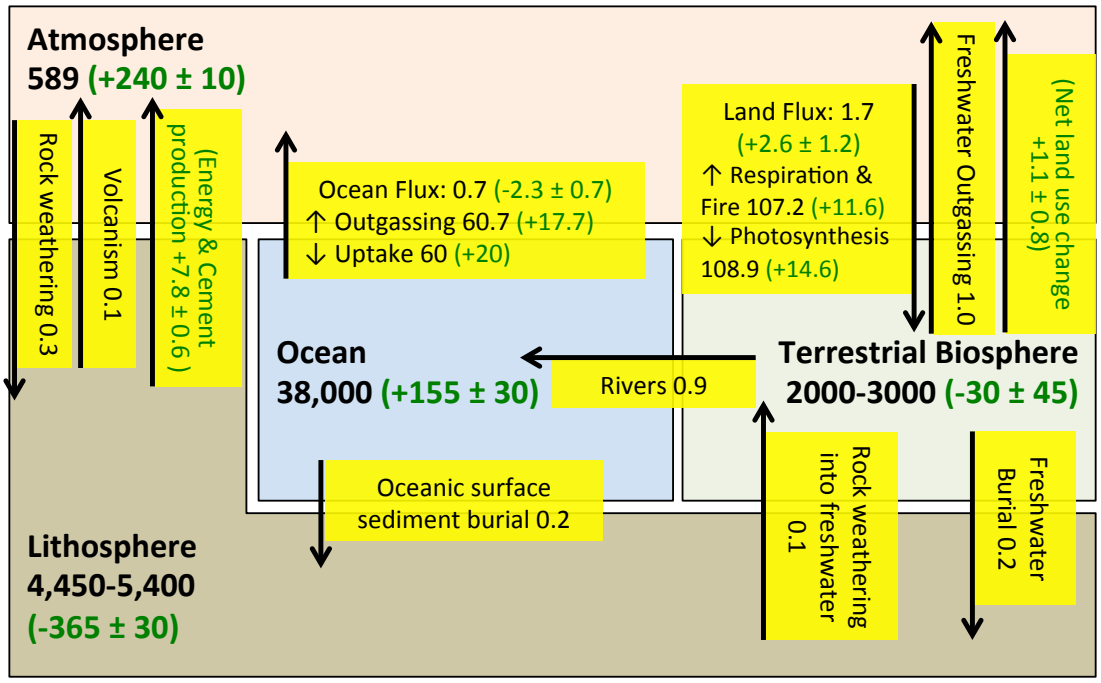

Figure 1.2: Sizes of the major fluxes of carbon between reservoirs in PgC yr^{-1} in yellow boxes, with black text showing preindustrial values and bracketed green text showing the size and sign of the anthropogenic perturbation to those fluxes. Total reservoir sizes are shown in bold numbers in PgC in black text for the preindustrial era, with the estimated anthropogenic perturbations and their signs shown in bracketed green text. The land and ocean net fluxes have been broken down into their two major opposing constituent fluxes. Redrawn from (*Ciais et al.*, 2013)

Estimates of the fluxes of carbon between reservoirs in the preindustrial era are briefly explored here (Figure 1.2) but are examined in more detail by *Ciais et al.* (2013). The chemical weathering of silicate minerals ($CaSiO_3$) draws CO_2 from the atmosphere into rocks (i.e the lithosphere) at about 0.3 PgC yr^{-1} (*Archer and Brovkin*, 2008). Volcanic activity acts in the opposite direction, fluxing 0.1 PgC yr^{-1} into the atmosphere from the lithosphere (*Archer and Brovkin*, 2008). The preindustrial ocean is thought to have been a source of CO_2 for the atmosphere, emitting about 0.7 PgC yr^{-1} (*Sabine et al.*, 2004). In addition, the global oceans sequester 0.2 PgC yr^{-1} into the lithosphere through the sinking and subsequent burial of particulate matter (*Denman et al.*, 2007). The preindustrial terrestrial biosphere is estimated to have been a large sink for atmospheric CO_2, drawing in 1.7 PgC yr^{-1}. The land sink exists because photosynthetic terrestrial vegetation draws

carbon into living organic matter, but is incompletely offset by respiration and fires. Furthermore, the world's freshwaters are estimated to outgas an additional 1.0 PgC yr^{-1}. The burial of sediment in aquatic environments fluxes 0.2 PgC yr^{-1} into the lithosphere, comparable to the global ocean except over a small fraction of the surface area. The action of mineral weathering by freshwaters adds 0.1 PgC yr^{-1} to the terrestrial biosphere from the lithosphere. Since river waters laden with carbon drain into the global ocean, there is a riverine flux of 0.9 PgC yr^{-1} from land into the marine environment. These 'natural' carbon fluxes between reservoirs represent an estimate of the 'background state' of the global carbon cycle over the last 11,700 years of the Holocene era that humans have perturbed over the most recent two and a half centuries. Note that although these fluxes originate from various sources, they are presented here as in (*Ciais et al.*, 2013), and are adjusted within their respective uncertainties to form a consistent budget. Even so, the fluxes presented in Figure 1.2 do not close with respect to the lithosphere, possibly representing omissions with regard to fluxes that operate over much longer timescales (centuries to millenia). A more detailed treatment of the lithospheric fluxes is not attempted here.

This section has set out a description of the preindustrial carbon cycle at the planetary scale. The next section presents the changes to the carbon cycle that human activities have imparted over the past two centuries.

1.2 Anthropogenic Carbon Cycle Changes

In the mid-1700s CE, the Industrial Era is considered to have begun and human activities began to have an unprecedented effect on the global carbon cycle (*Ciais et al.*, 2013). More than 120 years ago, *Arrhenius* (1896) famously identified the role of CO_2 in the greenhouse effect, and through correspondance with Arvid Högbom, pointed out that the burning of mined coal could add amounts of carbon to the atmosphere large enough to be considerable in global carbon cycle budgets. Since then, more than a century of Earth science has yielded a detailed understanding of the global carbon cycle and how human activities alter it. Humans remove carbon from the lithosphere via two main processes: 1) the extraction and subsequent

combustion of hydrocarbon fuels (coal, oil and gas) for energy generation and 2) the production of cement for construction. Furthermore, humans' changing use of land (mainly converting forest into cropland and grazing pasture) reduces land carbon storage, representing a flux into the atmosphere. Since the dawn of the industrial era to the year 2011, the Intergovernmental Panel on Climate Change (IPCC) estimated in their 2013 Assessment Report that these three anthropogenic factors have removed 365 ± 30 Pg C from the lithosphere and 30 ± 45 PgC from the terrestrial biosphere. Without human intervention, this so-called 'anthropogenic carbon' would likely have remained sequestered in the respective reservoirs for timescales on the order of millenia, and no known non-human process is capable of causing such rapid fluxes of carbon into or out of the lithosphere on an equivalent timescale (*Ciais et al.*, 2013).

For the most part, these processes have fluxed carbon into the atmosphere, causing the reservoir to accumulate 240 ± 10 PgC, mostly as CO_2 gas. This has increased the atmospheric pCO_2 from 278 ppm to 391 ppm between from 1750 to 2011 (*Ciais et al.*, 2013), and the 2016 annual mean was 402.8 ± 0.1 ppm (*Dlugokencky and Tans*, 2017). However, the existence of the biogeochemical fluxes described earlier mean that this carbon does not remain in the atmosphere. The response of the terrestrial biosphere has been challenging to constrain: the land flux is thought to have strengthened by 2.6 ± 1.2 PgC yr^{-1}, owing to an increase in photosynthesis unmatched by increases in respiration and fire emissions. However, human activities in the Industrial Era have also created a flux into the atmosphere resulting from net land use change on the order of 1.1 ± 0.8 PgC yr^{-1} (*Houghton et al.*, 2012). This flux arises through the clearance of forested land for agriculture and other uses (deforestation), and is partially offset by the intentional or unintentional growth or regrowth of vegetation on abandoned lands. Uncertainties associated with the preindustrial and modern terrestrial biospheric fluxes, and the magnitude of the reservoir's anthropogenic change are critically large, and therefore represent a facet of the global carbon cycle requiring much better constraint (*Ciais et al.*, 2013; *Regnier et al.*, 2013; *Le Quéré et al.*, 2016). The ocean has responded to the atmospheric CO_2 increase by switching from being a net source for the atmosphere to being a net sink of about 1.6 PgC yr^{-1} (*Takahashi*

et al., 2009; *Ciais et al.*, 2013). The ocean carbon reservoir has therefore increased by approximately 155 ± 30 PgC (*Khatiwala et al.*, 2009; *Ciais et al.*, 2013).

If some portion of the total anthropogenic carbon enters the global ocean then it is not able to directly contribute to the greenhouse effect, and therefore understanding the ocean flux is critical to our understanding of human-induced climate change. How much warming due to anthropogenic climate change humans can expect to encounter is therefore partly a function of emissions, but also very much dependant on the behaviour of the each of the carbon reservoirs. To determine expected warming levels over the coming decades, scientists have posed several key questions: how much carbon do the oceans absorb each year? How much does the ocean carbon flux vary from year to year? Will this flux keep pace with rising atmospheric CO_2 concentrations? For how long will oceanic anthropogenic carbon remain sequestered in the oceans? The pursuit of these types of questions has highlighted the need for a detailed understanding of the mechanisms by which the oceans store and exchange carbon: the ocean carbon cycle and the underlying carbonate chemistry.

With a description of the anthropogenic perturbation to the Earth system and the global cycle established, the following section examines the fundamental chemistry of the ocean inorganic carbon sink.

1.3 Ocean Carbonate Chemistry

One of the main pathways by which CO_2 enters or leaves the oceans is through its surface in contact with the atmosphere. As with any tracer at a fluid interface, CO_2 constantly exchanges between the atmosphere and ocean surface by diffusion. If a CO_2 concentration gradient is present across the air-sea boundary then a net flux across that boundary arises until an equilibrium is reached. The exchange of gas across a gas-liquid interface is not instantaneous, and depends on the rate at which diffusion may occur and the solubility of the gas in the liquid phase. All these quantities are related through the flux equation (1.1), where F (mol m^{-2} d^{-1}) is the net flux, $p\mathrm{CO_2}^{air}$ (μatm) and $p\mathrm{CO_2}^{ocean}$ (μatm) are the concentrations of CO_2 (as partial pressures) in the air and seawater respectively, k (m d^{-1}) is the

gas transfer velocity and α (mol m^{-3} μatm^{-1}) is the solubility coefficient:

$$F = (p\mathrm{CO}_2^{air} - p\mathrm{CO}_2^{ocean}) \times k \times \alpha \tag{1.1}$$

The flux equation (1.1) is explored in more detail in Section 2.1, but it is briefly introduced here as it relates to the wider context of ocean carbon cycling. The difference between the CO_2 partial pressure in the air ($p\mathrm{CO_2}^{air}$) and seawater ($p\mathrm{CO_2}^{ocean}$) determines the direction of the gas flux. Under this sign convention, air-ocean difference of partial pressures of CO_2 ($\Delta p\mathrm{CO}_2$) is defined with positive values corresponding to flux into the ocean and negative values out of the ocean. The gas transfer velocity (k) is a parameter that accounts for the variable rate at which CO_2 diffuses through a 'thin' surface layer of the liquid into the more homogenous sublayer below (*Liss and Slater*, 1974). The gas transfer velocity is highly sensitive to both the thickness and dynamics of this 'surface film' (*Wanninkhof et al.*, 2009). Exchanges of momentum between the air and water rework the surface film and affect k. In the context of the oceans, the action of winds blowing over the water surface is the main process that perturbs the surface film and is therefore a key control on k. Air-sea buoyancy fluxes (*McGillis et al.*, 2004) and the presence of surfactants that modify the surface tension of seawater (*Sabbaghzadeh et al.*, 2017) are also critical environmental variables controlling k. The effect of CO_2 solubility in modifying the flux is quantified through α. The variable solubility effect arises due to the considerably non-ideal behaviour of CO_2 gas, and is a function of temperature and salinity (*Weiss*, 1974).

$$\mathrm{CO_2 + H_2O \leftrightharpoons HCO_3^- + H^+} \tag{1.2}$$

$$\mathrm{HCO_3^- + H^+ \leftrightharpoons CO_3^{2-} + 2H^+} \tag{1.3}$$

In the atmosphere, under common temperature and pressure conditions, CO_2 does not show a tendency to change its form; it is at thermodynamic equilibrium. When CO_2 dissolves into seawater, it ceases to be at thermodynamic equilibrium, and reacts with seawater (H_2O) to form different carbon species. Some of the dis-

solved CO_2 will remain as aqueous CO_2 (CO_2(aq)). Another portion of dissolved CO_2 reacts with seawater to form bicarbonate (HCO_3^-) and a proton or hydrogen ion (H^+), equation (1.2). Bicarbonate in seawater will react with free protons (H^+) to form carbonate (CO_3^{2-}) and two additional protons, equation (1.3). Dissolved CO_2 in seawater exists as these three main species: aqueous CO_2, bicarbonate and carbonate (although a very minor fraction exists as carbonic acid, H_2CO_3). The exact partitioning that carbon takes in a given sample of seawater (i.e. what proportion exists as each of the three species) depends on the concentration (or more precisely, the activity) of protons in solution. In seawater carbonate chemistry, the role of active protons is commonly expressed as the potential of hydrogen, pH, which is quantified as the negative of the decimal (or base 10) logarithm of hydrogen ion activity. If one were to acidify a seawater sample to a pH below approximately 6 (higher H^+ concentrations), most of the total CO_2 would exist as CO_2(aq), while at pH greater than about 9 (lower H^+ concentrations), thermodynamic equilibrium favours the formation of CO_3^{2-}. At weakly alkaline pH levels that are typical of seawater (pH $\approx$ 8.2) most carbon exists as HCO_3^-. The total amount of these three dissolved carbonate species, or Dissolved Inorganic Carbon (DIC) (or simply C) is expressed as the sum of all three concentrations, equation (1.4).

$$\mathrm{DIC} = \mathrm{C} = \sum \mathrm{CO_2} = [\mathrm{CO_2}] + [\mathrm{HCO_3^-}] + [\mathrm{CO_3^{2-}}] \tag{1.4}$$

The dissolution of carbon dioxide clearly has implications for the acidity of seawater, since the reaction releases hydrogen ions. The anthropogenic release of large amounts of CO_2 into the atmosphere therefore raises concerns about widespread changes in ocean pH, which could have profound effects on marine ecosystems. The ocean acidification aspect of climate science and the carbon cycle (and its downstream consequences on biology) is an important frontier of modern science that is not addressed in this thesis. The scope of this work is on the underlying drivers behind the ocean response to rising atmospheric CO_2 levels, rather than a comprehensive assessment of its consequences.

Now that the basics of ocean carbonate chemistry have been established, the next section will explain the large-scale physical, chemical and biological processes

that exchange carbon in the global ocean.

1.4 The Ocean Carbon Cycle

While the view of the ocean as a singular, large reservoir of carbon is useful to understand global biogeochemical cycles, the oceans are of course highly nuanced and variable on a broad spectrum of spatial and temporal scales. The marine environment is a dynamic fluid medium in which a diverse range of physical, chemical, biological, and geological processes interact to modify carbon concentrations locally and, hence, globally. Before examining the much more complicated ocean carbon cycle in the real world, it is helpful to create a schematic view of a simplified ocean to introduce key biogeochemical concepts.

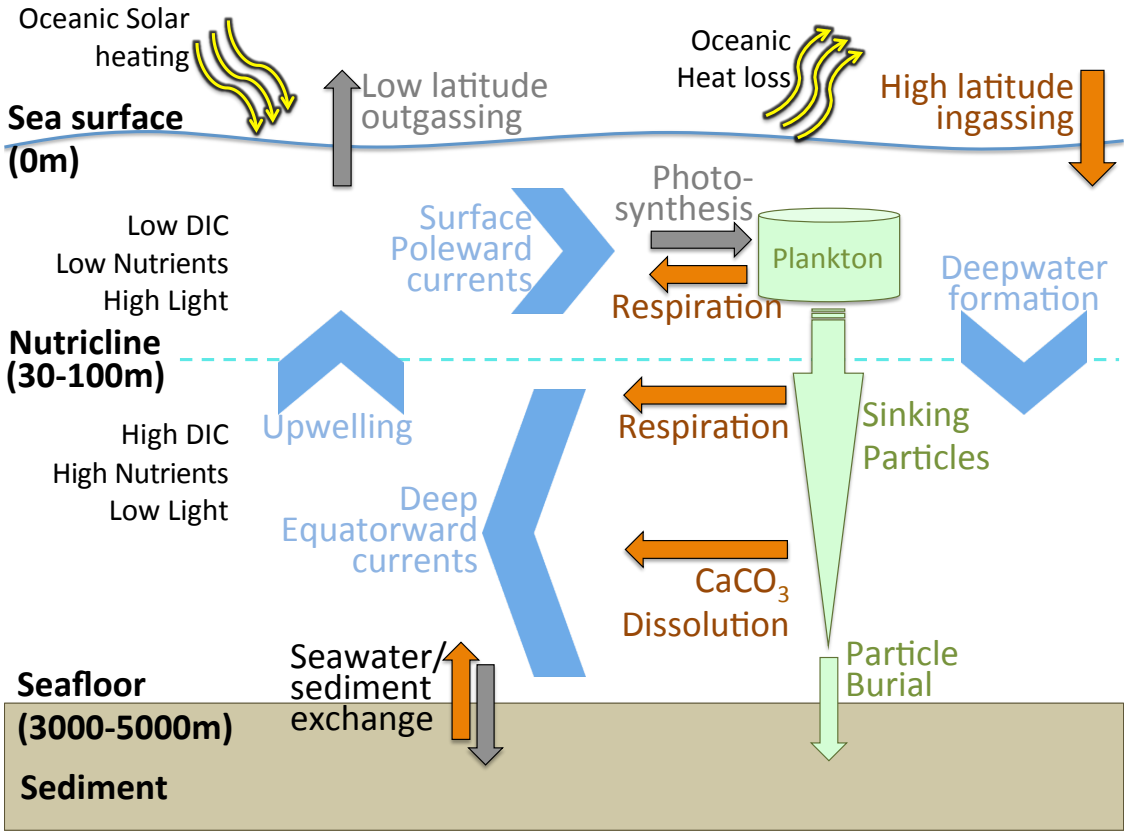

Figure 1.3: Schematic view of the ocean carbon cycle. Orange arrows indicate processes which add DIC to seawater and grey arrows show processes that remove it. Blue chevrons indicate the movement of DIC around the oceans by physical redistribution. Green shapes indicate the connection between the marine biosphere and the carbon cycle

Near the equator, oceanic surface heating increases local seawater buoyancy

while at high latitudes the oceans lose heat (and buoyancy) to the overlying atmosphere (yellow arrows in Figure 1.3). This differential buoyancy flux results in surface poleward currents, equatorial upwelling, high latitude deepwater formation, and a deep interior equatorward flow (blue chevrons in Figure 1.3). This meridional overturning circulation sets up a large scale pathway by which carbon can be advected around the oceans. In equatorial regions of strong solar heating, warming of ocean surface waters reduces the solubility of CO_2 in seawater and so drives net annual low latitude outgassing (*Takahashi et al.*, 2009). By contrast, while the oceans lose heat to the atmosphere along the poleward paths of western boundary currents, CO_2 becomes more soluble and CO_2 influx results (*Follows et al.*, 1996). Changes in CO_2 solubility between high and low latitudes and the resultant downwelling of cold waters drives the 'solubility pump' of carbon (*Volk and Hoffert*, 1985).

Biological processes play a critical role in the ocean carbon cycle. In the sunlit photic zone of the surface ocean, photosynthetic organisms fix DIC from seawater into their bodies, driving down local DIC concentrations. Heterotrophic (and autotrophic) organisms consume organic matter and add CO_2 to seawater through respiration. The balance of the opposing actions of photosynthesis and respiration determines whether biological activity either enriches or depletes local seawater DIC. In highly productive regions such as the surface subpolar North Atlantic during springtime, biological CO_2 fixation stimulates ocean CO_2 uptake by decreasing pCO_2 in the mixed layer (*Takahashi et al.*, 2009; *Sanders et al.*, 2014). The time mean effects of high annual biological productivity in addition to the solubility pump effect along the northward-flowing North Atlantic Current make the North Atlantic basin a particularly strong annual mean sink of CO_2. Note that elsewhere in the ocean, for example in the equatorial Pacific, the solubility and biological pumps can act in opposition to one another (e.g. *Turk et al.*, 2001). Away from the ocean surface, sunlight strongly limits photosynthesis, but heterotrophs may still consume organic matter and drive CO_2 into solution by respiration. Organic matter rains downward from the surface ocean as particles of detritus. Heterotrophs consume some portion of this sinking organic material, causing a balance of net respiration below the photic zone that enriches deep seawater with DIC. The

fixation of inorganic carbon by photosynthesisers in the surface ocean followed by its subsequent remineralisation at depth is called the 'biological' or 'soft tissue' pump (*Volk and Hoffert*, 1985).

Sinking organic matter has an additional affect on interior carbon concentrations via the carbonate pump. Calcifying organisms in the upper ocean such as coccolithophores draw DIC into their bodies to form $CaCO_3$ shells. In the deep ocean, the pH may be lower than in the open surface ocean where $CaCO_3$ is insoluble (*Takahashi et al.*, 2014). This vertical pH contrast means that sinking $CaCO_3$ particles may pass a depth horizon, the Carbonate Compensation Depth (CCD), beyond which $CaCO_3$ begins to dissolve. When $CaCO_3$ particles dissolve, they add carbonate back into solution and increase local DIC (*Volk and Hoffert*, 1985).

The raining down of organic matter from the photic zone of the ocean therefore enriches deep waters in DIC via the soft tissue and carbonate pumps. Since there are no large scale processes which remove DIC from the ocean interior, waters accumulate carbon with age since ventilation. However, not all sinking particles remineralise in the water column, and some portion reach the seabed. Surface seabed sediments and the benthic communities within them may interact with overlying seawater with important effects on global biogeochemical cycles (*Kriest and Oschlies*, 2013; *Yool et al.*, 2017). This can mean that surface sediments may remineralise back into or seawater, or they may be buried for millenia (*Archer et al.*, 1998; *Ridgwell and Zeebe*, 2005). Burial of sinking marine particulate matter (*Keil*, 2017) and of terrestrial organic matter (*Berner*, 2003) is a critical process in global carbon cycling over geological timescales, and may be the long term sink to match volcanic and geological sources of carbon .

Note that this schematic does not describe the role of Dissolved Organic Carbon (DOC). A broad range of compounds make up DOC, with a variable degree of availablity as energy sources for marine microorganisms (*Repeta*, 2015). Compounds like sugars and amino acids are produced and consumed on timescales of days, and support a vast pool of heterotrophic microorganisms (*Hansell*, 2013). These short-lived compounds amount to around 0.2 PgC globally and are less important for global biogeochemical cycles than the 660 PgC of DOC that are either

too recalcitrant (*Hansell and Carlson*, 2015) or too dilute (*Arrieta et al.*, 2015) to be readily bioavailable, and remain stored in the ocean for decades to millenia. The extent to which the global DOC pool has changed through geological time (and therefore modulates climate) is poorly understood and represents an important scientific frontier relevenant to multicentennial and longer climate cycles (*Ridgwell and Arndt*, 2015).

With a summary of the main biogeochemical background of the ocean carbon cycle established, the aims and scope of this thesis can next be addressed.

1.5 Thesis Structure and Scope

The global ocean represents an important part of the climate system as a sink of carbon for the atmosphere. A wide range of processes is known to be important in controlling the strength of the oceanic carbon sink, yet there is an incomplete knowledge of how these processes will change under anthropogenically driven climate change. Presently, there is a clear understanding that the global ocean is a sink for atmospheric carbon (*Ciais et al.*, 2013), and that the air-sea carbon flux shows substantial variations with time (*Landschützer et al.*, 2016). However, the combination of large uncertainties and year-to-year variability of the net ocean carbon flux, make the detection of trends challenging (*Wanninkhof et al.*, 2013; *McKinley et al.*, 2016). This means that the future of the ocean carbon sink is critically uncertain for the purposes of the prediction of future climate change (*McKinley et al.*, 2017). This thesis explores the causes of carbon flux variability and carbon inventory variability over different timescales to pinpoint which processes appear to be important. A broad range of processes affect the variance in the ocean carbon sink (for example, as in Figure 1.3), and important efforts are being made to measure all of them with ever-reducing uncertainty. This thesis takes a different approach, and instead asks whether all processes are important for all timescales of variability. If some processes are minor or negligible contributors to variability, then the uncertainties associated with predicting those processes become unimportant. Specifically, this thesis investigates which components of gas exchange and the ocean carbon cycle set variability at the North Atlantic and

global scale.

This first chapter to this point has provided a brief introduction to the role of carbon in climate, the global carbon cycle and finally the role of the ocean within that cycle. The next sections provides a brief description of ocean modelling in general, the considerations behind the selection of an ocean model, and a description of the model chosen. This introductory chapter is followed by three research chapters, each of which addresses related but distinct scientific questions. Therefore, each research chapter is motivated by different scientific literature, makes use of its own set of methods and produced separate results. As a consequence, the three research chapters are written as three distinct scientific reports, each inspired by the previous.

The second chapter investigates air-sea CO_2 gas transfer in the North Atlantic, identifying the relative importance of the interfacial concentration gradient and the gas transfer velocity in governing interannual gas flux variability. The work presented in the second chapter was published as a peer-reviewed manuscript (*Couldrey et al.*, 2016), and is reproduced here with exactly that content (although there are a handful minor changes to wording and corrections of typographical errors). The third chapter follows from the finding of the second that variability in oceanic carbon concentrations (rather than gas transfer velocities) strongly control multiannual carbon flux variability. Chapter three explores the roles of solubility, the soft tissue pump, the carbonate pump, carbon disequilibria and anthropogenic carbon in controlling North Atlantic carbon concentrations. With a detailed analysis of the North Atlantic carbon inventory variability established, the fourth chapter proceeds to identify which processes control inorganic carbon variability in the global ocean as a whole. The final chapter ties together the three research chapters together and highlights the scientific questions that have remained or emerged.

1.6 Choice of Modelling Approach

The global ocean carbon cycle is challenging to study, requiring observations of its physical, chemical and biological states on a wide range of time and spatial scales. Carbon observations are the most numerous at the sea surface, and data

compilations such as Surface Ocean CO_2 Atlas (SOCAT) (*Bakker et al.*, 2016) and the LDEO surface carbon database (*Takahashi et al.*, 2014) aim to compile the ever expanding collection of measurements of surface pCO_2 in a common, quality-controlled format. These data collation projects add enormous value to already extant data, and make it possible to study the ocean carbon cycle on a much larger scale than ever before. Direct oceanic pCO_2 measurement is presently not feasible on platforms with global coverage such as Argo floats or satellites, and consequently data are patchy. As a result, these sparse observations are typically interpolated and extrapolated by mapping them onto better-sampled variables before they can be used for large scale analysis of changes in the ocean carbon sink (*Rödenbeck et al.*, 2014; *Landschützer et al.*, 2016).

Ocean carbon observation coverage in the subsurface is more limited than at the surface. Similar to the SOCAT dataset, the Global Ocean Data Analysis Project (GLODAP) is a 3D (longitude, latitude and depth) compilation of biogeochemical and physical parameters (*Key et al.*, 2015; *Olsen et al.*, 2016). While highly accurate and precise surface pCO_2 measurements can be made autonomously on underway commercial ships, the types of data curated in GLODAP are more labour-intensive to produce, and so are only collected during infrequent, targeted scientific research expeditions. Our understanding of changes in ocean carbon content at scales larger than fixed point observatories is therefore limited to a handful of locations where repeated occupations of hydrographic sections have been undertaken (e.g. *Humphreys et al.*, 2016). As with SOCAT, GLODAP greatly facilitates the use of biogeochemical observations at space and time scales never before possible. However, basin-wide quantification of year-on-year biogeochemical changes is presently beyond the scope of datasets like GLODAP alone.

The global ocean carbon reservoir is spatially and temporally undersampled for the purposes of understanding interannual to multidecadal variability, and so different approaches must be used to study beyond the coverage of the data. Numerical models can provide unique insight into an incompletely observed system by drawing upon a theoretical understanding of that system's functioning. Models necessarily are simplified representations of reality. When building or using models, researchers must consider carefully the level of simplification appropriate for

the questions being pursued. Fundamental design choices tend to give rise to loose classes of models, and it is useful to appraise oneself of these when deciding exactly which example to use. A few examples of the major types of models encountered in the context of ocean carbon cycling are discussed.

1. Box Models. A computationally lightweight and highly conceptual class of model, that typically considers the Earth system component of interest in terms of small numbers of homogenous reservoirs (boxes) with simple exchanges between them. These are useful to study the Earth at a very broad scale or with reduced dimensionality, allowing for fluxes between reservoirs or bulk inventories within reservoirs to be calculated. A classic example of such a model is that of *Oeschger et al.* (1975), which consists of four boxes representing the atmosphere, terrestrial biosphere, the upper ocean and deep ocean. Although it is now possible to solve much more computationally complex models, the box model is still a relevant and useful tool; *Halloran et al.* (2015) recently used box modelling to help distil the output of a large ensemble of coupled climate simulations into a more digestible, mechanistic understanding of the system's functioning.

2. Idealised Models. Two or three dimensional models that conceptually represent the real world, but strip away much of the system's complexity. This allows for the selected dynamics of interest to be modelled in a great degree of detail (for example at high resolution) and in a degree of isolation from confounding dynamics, without attempting to completely describe the entire system. For example, *Munday et al.* (2014) describe a model that considers the global ocean as a longitudinally narrow sector, with a simple biogeochemical model and with a wind-driven southern overturning, to describe how Southern Ocean ventilation impacts global storage of carbon in the ocean and atmosphere. The simplicity of the domain and biogeochemistry allows relatively high spatial resolution, such that the role of mesoscale eddies can be studied. In addition, idealised models can be useful to generate ensembles of simulations, or to model very long time periods.

3. Three-Dimensional Global Ocean Models. These endeavour to represent a

wide range of processes in a moderate level of complexity. Ocean biogeochemical models (which themselves range in complexity) may be coupled to 3D ocean models, adding computational expense. Such models can be forced with observation-based products and used to probe recent ocean change. In addition, ocean-only models can be forced with output from atmospheric models, allowing for simulation of the future (*Yool et al.*, 2013b). Ocean-only models are easy for users to run, and computationally less expensive than coupled ocean-atmosphere models.

4. Regional Models. These models seek to represent smaller geographical areas in a high level of detail or at reduced computational expense. They are useful in applications where local geographical details are important, such as coastal wave and tide modelling. Regional models must be forced with boundary conditions at the edges of their domains (e.g. *Arruda et al.*, 2015), or they may be nested into global simulations that use lower resolutions (e.g. *Böning et al.*, 2016). Regional models become particularly useful when the theoretical challenges of assigning boundary conditions are outweighed by the benefits of higher resolution or increased complexity, for example in operational forecasting where computational cost is critical.

5. Earth System Models. This class of model couples together physical models of the atmosphere, ocean, terrestrial biosphere, cryosphere, as well as chemical models of the atmosphere and oceans, and is used to study the interaction between these systems. They are the main tool for climate projection because the feedbacks between system components are critical. They are very computationally expensive, and therefore each component will typically be represented at coarse resolution and with heavily simplified dynamics in comparison with what is possible with each individual model, yet they provide more holistic insight into the Earth system. Earth System Models are most useful in the study of feedbacks between systems like the ocean, atmosphere and terrestrial biosphere (*Collins et al.*, 2011; *Taylor et al.*, 2012).

Each of these approaches provides a different perspective on the ocean carbon cycle, and so careful consideration must be taken to choose the correct tool for

a given research question. This thesis primarily investigates global ocean carbon cycle variability on interannual to multidecadal timescales, with a focus on the role of the North Atlantic ocean. Of particular interest is the response of the global ocean to climate change driven by anthropogenic emissions of greenhouse gases. Therefore, a model must be chosen that is capable of simulating the global ocean as a whole, over a centennial timescale covering the industrial era to the year 2100CE (a commonly used terminal date in climate forecasting e.g. by the IPCC).

Three dimensional ocean models do not necessarily include more detailed dynamics than many Earth System Models, and instead benefit from higher resolution than would be possible for the same computational expense. Deconvolving the drivers of change in complex, coupled systems is challenging, but a standalone ocean model allows for more direct diagnosis of those drivers. An ocean model forced only with observation-derived products results in more a realistic physical ocean state, making analysis more directly applicable to the real world, but reveals little about potential future changes. An ocean model forced with atmospheric output from a different atmosphere-ocean simulation has the benefit of vastly reduced computation versus a fully coupled simulation, but lacks the ability to study atmosphere-ocean feedbacks. Furthermore, uncoupled ocean models cannot be spun up with a fully consistent atmosphere.

The main advantages of an uncoupled ocean simulation lie in its practicality, and so this setup allows for more rapid investigation of the drivers of ocean carbon cycle changes. Findings derived using this setup are therefore unlikely to be holistic or complete. However, this type of setup will be of the greatest value when used to guide the interpretation of much more complicated simulations such as Earth System Models, or more 'standard' ocean simulations forced by observation-derived products.

1.7 An Overview of NEMO-MEDUSA

The General Circulation Model (GCM) chosen is version 3.2 of the Nucleus for European Modelling of the Ocean (NEMO) (*Madec*, 2008). The name NEMO describes a framework of interconnected sub-models that together represent the

ocean. The ocean dynamics and thermodynamics are managed by software called OPA (Océan PArallélisé) (*Madec et al.*, 1998). The sea ice submodel is version 2 of the Louvain-la-Nueve Ice Model, LIM2 (*Timmermann et al.*, 2005), although other submodels may be used. TOP (Tracer in the Ocean Paradigm) is the system that manages the handling of tracers, particularly for biogeochemical submodels. These components alone may be used to study physical research questions, or they may be coupled to a biogeochemical model such as Model of Ecosystem Dynamics, Utilisation, Sequestration and Acidification (MEDUSA) (*Yool et al.*, 2011, 2013a).

NEMO is a highly versatile model, readily deployable to a range of applications in various configurations. NEMO is very widely used in the global scientific community, with a large community of registered users contributing to more than 180 projects and about 300 publications worldwide (*NEMO*, 2017). An exhaustive description of NEMO configurations is not attempted here as it would be enormous, with new developments continually expanding such a list. The standard global domain ORCA-family of grids encompasses horizontal resolutions from 4° to 1/4° grid cell sizes, with various vertical grids (*Madec*, 2008). Higher resolutions and alternative (e.g. regional and idealised) domains also exist, but are not discussed here. These very high resolution simulations are typically only feasible when run without computationally expensive biogeochemical models.

The configurations described in this thesis were run using a horizontal resolution of 1°, using the ORCA1 grid based on the grid described by *Madec and Imbard* (1996). This grid is not sufficient to resolve the mesoscale, and employs the common *Gent and McWilliams* (1990) eddy parameterisation scheme. Horizontal resolution is finer at low latitudes; about 1/3° of latitude at the equator to better represent equatorial upwelling. The grid has 292 × 362 horizontal points. The choice of resolution is a tradeoff between computer run time and grid cell size. In some respects, higher resolution produces more realistic fields (*Yool et al.*, 2015), but at much higher computational expense. The 1° resolution (rather than the 1/4°) offers, for the purposes of this study, a suitable compromise between practicality and model performance.

NEMO users may also choose from a range of vertical resolutions. The model

may be run using z-level (depth) bathymetry whose slopes resemble the steps of staircases or s-level (terrain-following) density coordinates of variable vertical thickness. In addition, the ocean surface may be represented as a 'fixed lid' surface, or a nonlinear free surface that can change in volume. In this study, the 64 z-level configuration with a fixed lid was used, which has thinner layers at the surface (the thinnest being ∼6m) that increase with depth (to ∼500m thickness). The choice of vertical coordinate affects the representation of features such as downslope cascades of dense waters and vertical mixing.

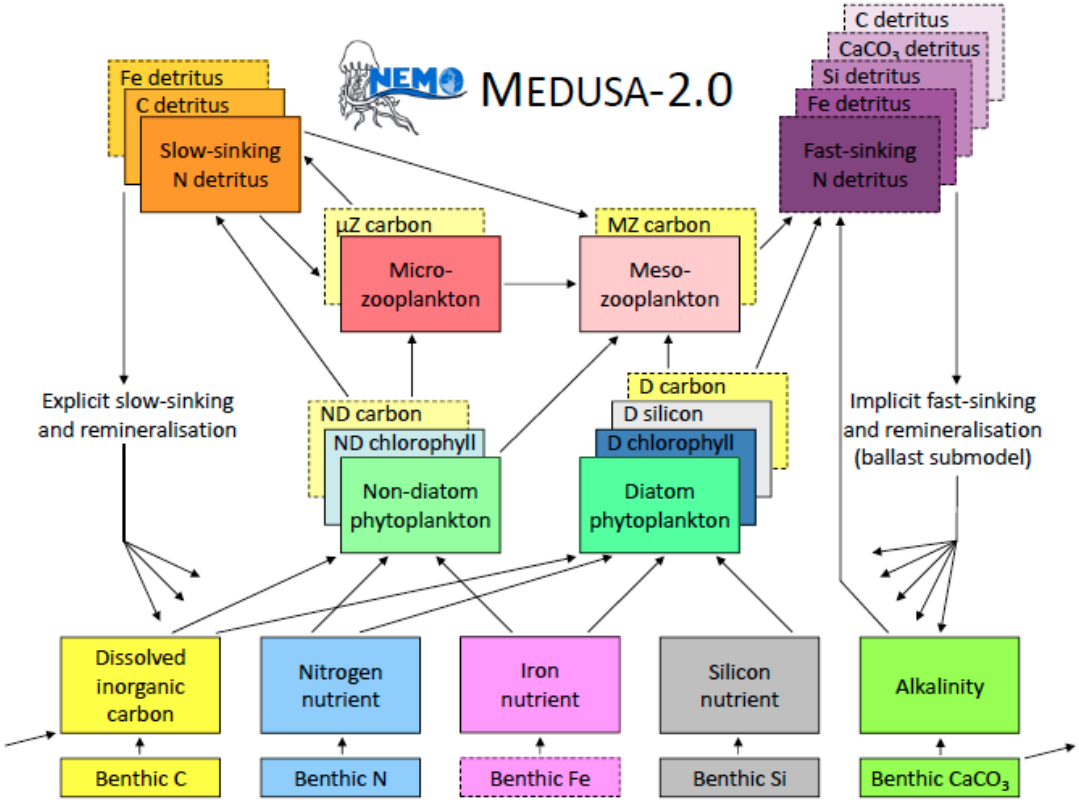

Figure 1.4: Schematic view of the major variables and their exchanges in MEDUSA-2, reproduced from (*Yool et al.*, 2013a). Boxes with solid lines show explicitly modelled state variables, while dashed borders show implicitly modelled properties. Overlapping boxes indicate components comprised of multiple currencies (which may be explicitly or implicitly modelled). Smaller boxes at the bottom show 2D (lacking depth) benthic reservoirs of chemicals. This diagram does not show the model treatment of oxygen for visual clarity. Diagonal arrows on the bottom left and right corners indicate that the dissolution of benthic $CaCO_3$ releases both DIC and alkalinity

The biogeochemical module used in this study is MEDUSA-2, the second version of an intermediate complexity representation of ocean biology and nutrient chemical cycling (*Yool et al.*, 2013a). MEDUSA-2 was designed for the study of the effects

of anthropogenic climate change on ocean biology and associated biogeochemistry. It includes three-dimensional state variables (solid line boxes in Figure 1.4) for phytoplankton and zooplankton, sinking detritus, and chemical tracers: nutrients, oxygen (not shown in schematic), and carbon. MEDUSA-2 considers two functional types of primary producers: diatom and non-diatom phytoplankton. The oceanic nutrients for these primary producers are modelled as 3D tracers of generic dissolved inorganic nitrogen (DIN, an aggregation of all nitrogenous species like nitrate, ammonia, etc.), silicic acid, and iron (second from bottom row, Figure 1.4). Heterotrophic zooplankton feed on these phytoplankton are represented according to two size categories, micro- and mesozooplankton. MEDUSA-2 can be viewed as a conjunction of two linked but size-distinct Nutrient-Phytoplankton-Zooplankton-Detritus (NPZD) models. Both phytoplankton and zooplankton produce explicitly modelled slow-sinking detritus, or non-living particulate organic matter (top left, Figure 1.4). There are tracers for slow-sinking detrital carbon and nitrogen to account for the roles of slowly sinking organic matter in cycling these chemicals. The model also implicitly includes fast sinking detritus (top right, Figure 1.4), whose remineralisation is parameterised exponentially as a function of depth using a *Martin et al.* (1987)-type curve. The final 3D tracers included are DIC, oxygen and alkalinity. These state variables allow for details about the carbon cycle such as pH, air-sea CO_2 flux and carbon content to be modelled. There are also two dimensional fields of organic nitrogen and carbon, inorganic silicon and inorganic calcium carbonate to represent pools of biogenic material in the seafloor (bottom boxes, Figure 1.4).

The carbon cycle in NEMO-MEDUSA can be described as a system of carbon exchanges between biotic and abiotic reservoirs in response to physical, chemical, and biological processes. The previous paragraph describes how MEDUSA-2's ecosystem structure allows for carbon (and other chemical tracers) to be exchanged between seawater (as DIC), phytoplankton, zooplankton, and sinking detrital matter. Seawater DIC varies in response to air-sea gas exchange according to the flux equation, (1.1). The wind speeds at 10m above sea level from the atmospheric forcing set at every time step are used to calculate fields of gas transfer velocities using the *Nightingale et al.* (2000) gas transfer velocity and the Schmidt number

of *Wanninkhof* (1992). Fields of DIC and alkalinity are used to calculate oceanic pCO_2 for the flux equation, since those two components of the carbonate system are modelled directly. The model does not use fugacity for gas exchange calculations, and instead uses partial pressure for simplicity. The only biogeochemical processes that vary alkalinity in MEDUSA-2 are calcium carbonate production, dissolution and benthic calcium carbonate dissolution, (*Yool et al.*, 2013a), their equation 14. A complete representation of the alkalinity cycle (e.g. *Wolf-Gladrow et al.*, 2007) would introduce substantial computational cost, for example requiring explicit modelling of calcifying classes of organisms, separate tracers of nitrogenous species (rather than a bulk DIN pool) etc. MEDUSA-2 does not include representations of dissolved organic species. The implementation of carbon system equations in MEDUSA-2 follows the standard Ocean Carbon Cycle Model Intercomparison Project (OCMIP, http://ocmip5.ipsl.jussieu.fr/OCMIP/) procedure, and is very similar to existing software implementations (*Lewis et al.*, 1998). The constants used are summarised in Table 1.1.

In addition to explicitly modelled aspects of the carbon cycle, there are implicitly modelled tracers and processes. For example, a generic iron nutrient in seawater is included as a 3D tracer in the model (but there is no detailed treatment of iron speciation). However, iron in detritral organic matter (either fast or slow sinking) becomes rigidly coupled to nitrogen by assuming it exists at a fixed stoichiometric ratio to nitrogen. Abiotic calcium carbonate ($CaCO_3$) is not modelled directly, because to do so would require a more detailed plankton ecosystem, and because of uncertainties in ecological cycling; see Section 2.3.9 in (*Yool et al.*, 2013a). Calcium carbonate formation is parameterised as a function of the production of sinking material, and proceeds only if the saturation state of calcite favours calcification. If the saturation state at a particular location favours dissolution, then dissolution occurs. MEDUSA-2 uses carbonate ion concentration (calculated from DIC) and calcium concentration (parameterised as a global mean seawater value scaled by salinity) to calculate the calcite saturation state. The model assumes all $CaCO_3$ is the more stable calcite polymorph, and has no treatment of aragonite for simplicity. This sinking $CaCO_3$ is the input to the explicitly modelled 2D field of benthic CaCO3.

Table 1.1: CO_2 Equilibrium Coefficients in MEDUSA-2

Coefficient	Reaction	Reference
K_0	$[CO_2{}^*]/pCO_2$	(*Weiss*, 1974)
K_1	$[H][HCO_3]/[H_2CO_3]$	(*Millero*, 1995) after (*Mehrbach et al.*, 1973)
K_2	$[H][CO_3]/[HCO_3]$	(*Millero*, 1995) after (*Mehrbach et al.*, 1973)
K_B	$[H][BO_2]/[HBO_2]$	(*Millero*, 1995) after (*Dickson*, 1990)

To study changes to the ocean carbon sink under climate change, a model must be able to simulate changes to the 'carbon pumps' described in Section 1.4. The solubility pump depends on the physico-chemical state of the oceans; how its temperature, salinity and alkalinity will affect the tendency for CO_2 to dissolve into seawater. To understand how future CO_2 solubility varies and evolves, biogeochemical models therefore need reasonably detailed representations of carbonate chemistry and alkalinity cycles. Furthermore, the two biological pumps (the soft tissue and carbonate pumps) depend on processes such as the supply of carbon and nutrients by ocean circulation, ecosystem structure, variable stoichiometry of sinking detritus, mixed layer physics and many others. Therefore, a biogeochemical model that is able to explicitly model plankton communities, nutrient cycles, carbon and alkalinity cycles, and sinking detrital matter is needed. MEDUSA-2, therefore, is a tool well suited to the study of the ocean carbon cycle in a changing climate.

1.8 Simulation Initialisation and Drifts

This section describes details about the running of the simulations that are not directly pertinent to the main results of the thesis, but give a more complete account of what was done. All of the initialisation methods described in this section (unless otherwise specified) were devised and performed by Andrew Yool, and so do not constitute the work performed by the student in pursuit of the doctoral thesis. This thesis focuses on two different sets of simulations; the experiments described in Chapter 2 comprise one set, distinct from the experiments reported in Chapters 3 and 4. The simulations described in Chapter 2 were performed entirely by Andrew Yool, and those described in Chapters 3 and 4 were carried out by the student with guidance from Andrew Yool and Kevin Oliver. The majority of the

initialisation and forcing of simulations is common to all simulations.

All fields of DIN, silicic acid and oxygen were initialised using January values from the World Ocean Atlas (*Garcia et al.*, 2010a,b). The iron nutrient field was initialised using a field from a long duration simulation of a different model (*Parekh et al.*, 2005; *Dutkiewicz et al.*, 2005). DIC and alkalinity were initialised using a modified form of the GLODAPv1 climatology (*Key et al.*, 2004). Large regions that have no data in GLODAPv1 (the Arctic, the Caribbean Sea, the Mediterranean Sea) were filled using multiple linear regression (MLR) of unknown properties (DIC, alkalinity) on better known fields of temperature (*Locarnini et al.*, 2010), salinity (*Antonov et al.*, 2010), DIN, phosphate, silicic acid (*Garcia et al.*, 2010b) and oxygen (*Garcia et al.*, 2010a) in immediately neighbouring regions. Further details of the MLR method are included in (*Yool et al.*, 2013a). Other 3D model tracers for which no suitable global datasets exist (plankton and detritus) were initialised to very small values. The 2D benthic reservoirs of biogeochemicals were initially set to zero. Additional tracers for preformed alkalinity and DIN were used in Chapters 3 and 4. The initialisation procedures for these nutrients is described in the respective chapters, and comprise a significant part of the original research undertaken in pursuit of this doctoral thesis.

The choice of initialisation procedure will always affect the numerical outcome of ocean circulation simulations when the spin up duration is short relative to the overturning timescale. When there is a mismatch between the initial condition of a simulation and the equilibrium state that the model would adopt due to its own internal processes, the model state will 'drift' from the former to the latter. Time series of global mean DIC in a 240 year unperturbed control simulation illustrate this phenomenon clearly, but many other properties could also be used to the same end, Figure 1.5a. Ideally, several overturning cycles (tens of thousands of years) are necessary to eliminate the modelled ocean's 'memory' of its initial conditions, but such durations are not always practical. In general, however, shallow water properties quickly evolve according to the model's own behaviour (rather than maintain a mismatched initial state) because surface ocean processes operate on much shorter (up to instantaneous) timescales than the deep. In the case of surface DIC, there are larger drifts in the initial decades, then a much more gradual longer term trend

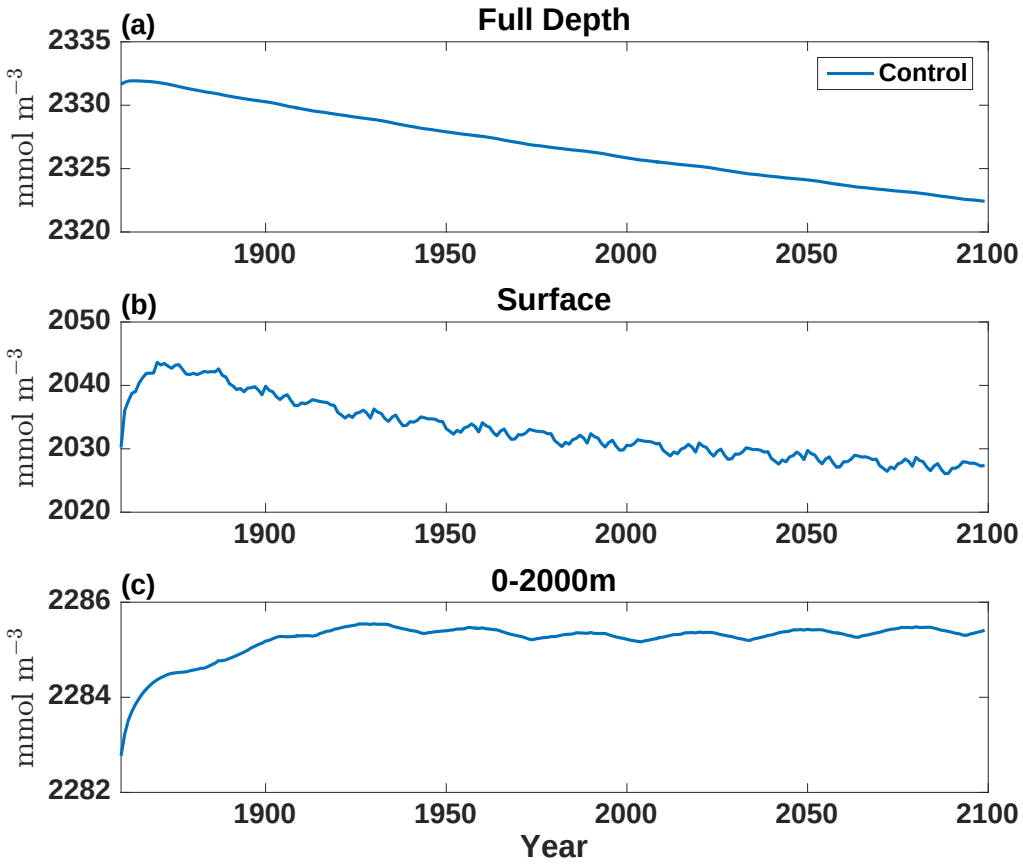

Figure 1.5: Mean ocean DIC concentration averaged over different depth domains for the control simulation spanning years 1860-2099 used in Chapter 2, showing model drift from initial conditions; the full depth (a), surface gridcells only (b) and the upper 2000m (c)

that diminishes over time, Figure 1.5b. Researchers can use this tendency to their advantage by choosing research questions carefully. For example, since most of the carbon cycle variability relevant to this thesis occurs in the upper hundreds of metres of the ocean, thousands of years of spin up are not necessary to eliminate most of the drift introduced by initial fields, Figure 1.5c. Furthermore, the use of control simulations allows for model drifts to be quantified and accounted in variability analyses. The process of subtracting model drifts from control simulations means that existance of drifts does not erroneously influence the interpretation of model results.

Different elements of the model system are forced (i.e. the model is run and calculations are performed) at different intervals to optimise computation time. The model in all experiments described in this thesis is forced mainly with output from

an Earth system model, HadGEM2-ES. The model is run using hourly timesteps for both dynamics and tracers. NEMO is forced at monthly intervals for precipitation, daily for radiation (shortwave and longwave) and six-hourly for turbulent variables (air temperature, humidity and wind velocity). In the surface gridcells, the biogeochemical model calculates gas fluxes contemporaneously with the turbulent variables, at six-hourly timesteps. Away from the sea surface, carbonate chemistry calculations are only performed monthly to improve model performance. The aeolian dust deposition of iron forcing set (*Mahowald et al.*, 2005) has an annual cycle but does not vary from year to year.

1.9 Physical Model Performance

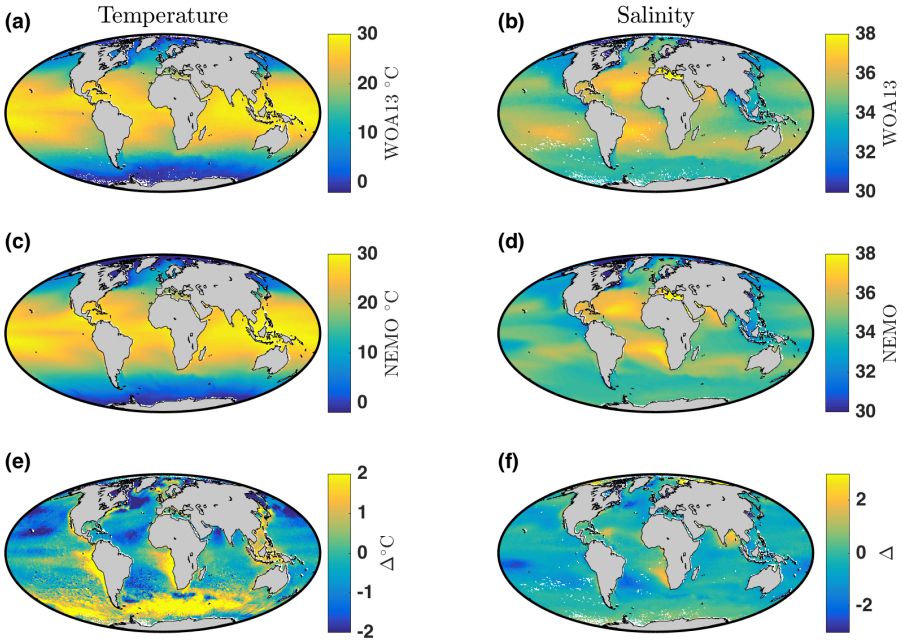

Figure 1.6: Comparison of climatological mean sea surface temperature, left, and salinity, right, from the World Ocean Altas (WOA13, top) (*Locarnini et al.*, 2013; *Zweng et al.*, 2013) and the 1980-2015 average from NEMO simulations used in Chapter 2 (middle). The bottom row shows the model field minus the observations (Δ), where positive values indicate high model bias

This section contains a brief discussion of the physical model performance. The aim here is to highlight general systematic performance issues common to NEMO when forced in ocean-only mode that are not specific to particular experiments. More detail about the simulations (validation, setup and forcing) are included in

their respective chapters. The model's Sea Surface Temperature (SST) and Sea Surface Salinity (SSS) fields are compared against the World Ocean Atlas (WOA13v2) climatological fields of temperature (*Locarnini et al.*, 2013) and salinity (*Zweng et al.*, 2013), Figure 1.6a, b. The model output was regridded from its nonlinear tripolar grid (*Madec and Imbard*, 1996) to the linear one-by-one degree grid of the observations for the calculation of the difference (Δ) between the two. To first order, the model's large scale SST patterns resemble the observations', showing strong low to high latitude contrast, as well as westward-positive temperature gradients at low and mid latitudes, Figure 1.6a,c. The difference between modelled and observed SST, Figure 1.6e, reveals high biases in the Southern Ocean, Arctic Ocean and the upwelling regions off the eastern South American and African continents. These features may be associated with the inability of the model grid to capture subgrid-scale features (such as mesoscale eddies) that are likely to be important here. Prominent low biases are found in the northern subpolar gyres, and are likely due to model's failure to represent fine scale features such as boundary currents and realistic dense water formation pathways. In the North Atlantic, these low bias regions correspond to the main source regions of the model's North Atlantic Deep Water. Shallow coastal waters show strong biases of both signs, reflecting the configuration's lack of optimisation for smaller scale seas away from the open ocean.

The model's SSS fields show first order agreement with the observations, including low latitude maxima in the subtropical gyres and poleward-negative salinity gradients, Figure 1.6b,d. The effect of the mislocated North Atlantic Current results in the low bias off eastern Canada, Figure 1.6f. The same problems in upwelling regions are evident as high biases in salinity, especially off the west coast of Africa. The Arctic shows high salinity biases along its coastal margins. In general, many of the most poorly represented regions in terms of SSS correspond to known problem areas for one degree simulations: western boundary currents, upwelling regions and active eddy fields.

The model's Atlantic Meridional Overturning Circulation (AMOC) is too weak, varying between 6 and 12 Sv (1 Sv $= 1 \times 10^6 \mathrm{m}^3\mathrm{s}^{-1}$) at 26°N in the configurations used in this thesis. The real world AMOC strength is estimated to be 17.5 Sv

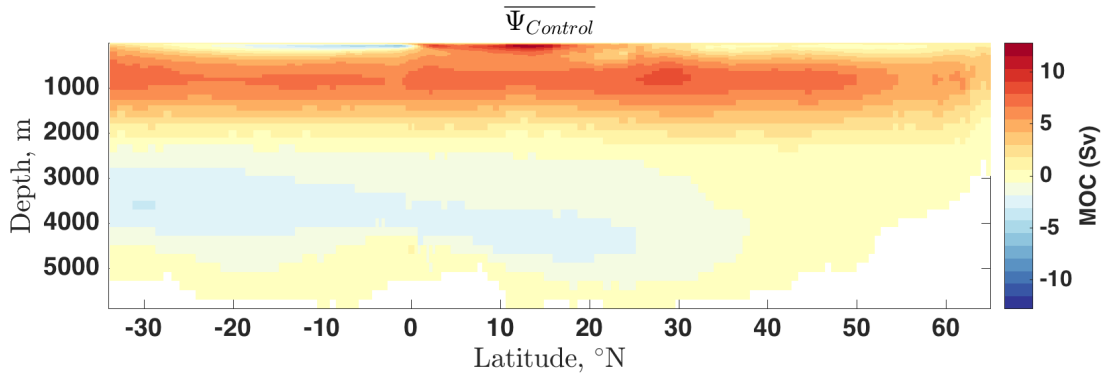

Figure 1.7: Zonally averaged meridional overturning streamfunction (Ψ) for the Atlantic, averaged over a 240 year control simulation

at 26°N, varying between 12.9 and 20.1 Sv between 2004 and 2011 (*Smeed et al.*, 2014). The maximum overturning depth at 26°N in the model is slightly too shallow, typically occuring around 750m (Figure 1.7) rather than the 1000m depth indicated by observations (*Smeed et al.*, 2014).

The sea ice module, LIM2 produces Northern hemisphere sea ice that agrees well with observations (*Gloersen*, 2006), Figure 1.8a,b. The prominent features of strongest coverage toward the Canadian archipelago and Greenland with more marginal cover around coastlines at lower latitudes are generally captured well. The seasonal ice zone generally corresponds to regions with incomplete coverage in the annual mean. Key differences are that ice cover is generally erroneously strong in the Northern hemisphere, resulting in slightly more expansive sea ice, especially off eastern Greenland and towards the Eurasian coast. Southern hemisphere sea ice coverage is biased low in the model, featuring an ice edge that is generally too close to the Antarctic coastline, Figure 1.8c,d.

In general, the regions showing the strongest temporal variability in sea ice cover correspond to locations where mean sea ice cover is partial. This manifests as variability in the extent of the ice edge, as well as the fraction of coverage poleward of the ice edge. These features are generally well captured in the northern hemisphere the model, with key sites of variability around Svalbard, and the ice edges, Figure 1.9a,b. The erroneously high sea ice coverage poleward of the Bering Strait and toward the Eurasian side of the Arctic mean that sea ice cover is relatively stable and therefore much less variable in the model than the real world. The magnitude of coverage variability in the Southern ocean is approximately correct, in spite of

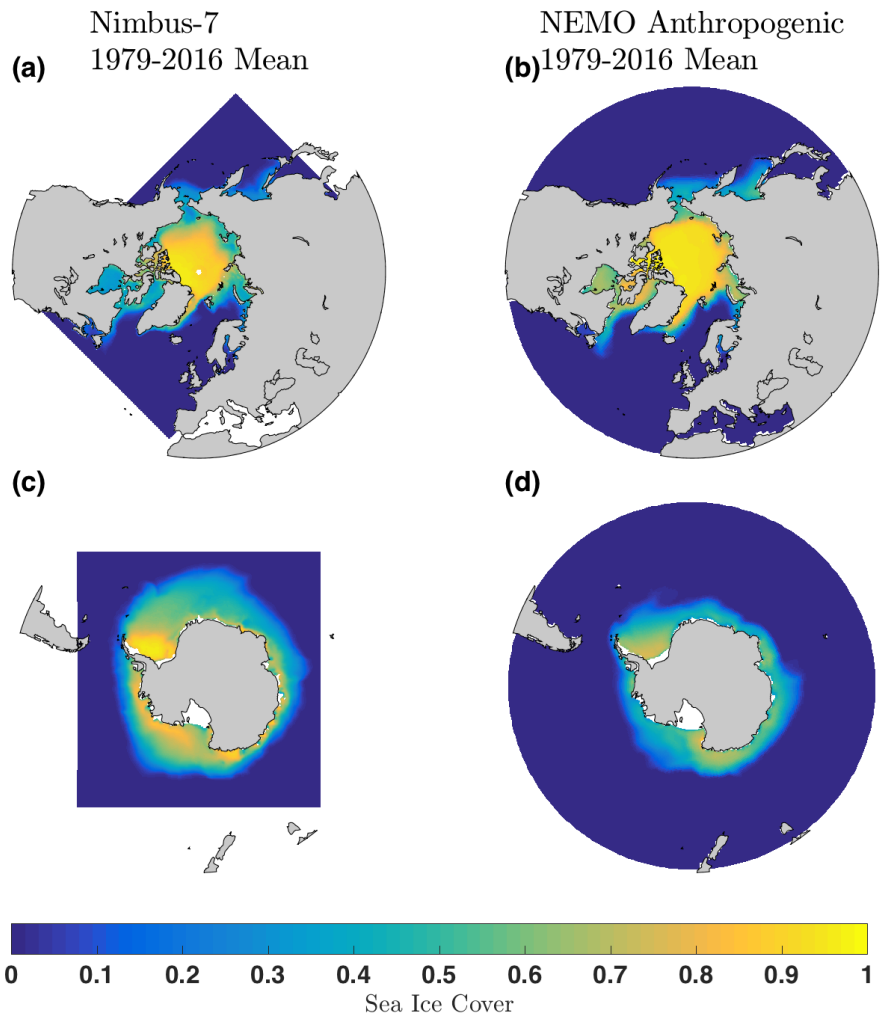

Figure 1.8: Mean sea ice cover calculated over 1979-2016 from Nimbus-7 satellite data (*Gloersen*, 2006), left, and the NEMO-MEDUSA Anthropogenic simulation described in Chapter 2, right, for the Northern (a and b respectively) and southern (c and d respectively) hemispheres

the problems with ice extent, Figure 1.9c,d.

Many of the main features identified here are common to global simulations with relatively coarse grid sizes. Although the ocean-only setup used here is quite different from the coupled Earth System Models used in the Fifth Coupled Model Intercomparison Project (CMIP5), it is interesting to note there are many shared weaknesses. These common issues likely stem from the fact that the atmospheric model used to force NEMO is HadGEM2-ES, one of the CMIP5 models. In particular, cold biases in the subpolar North Atlantic and warm biases in the Southern Ocean are linked to weaker Atlantic overturning (*Wang et al.*, 2014). Reduced pro-

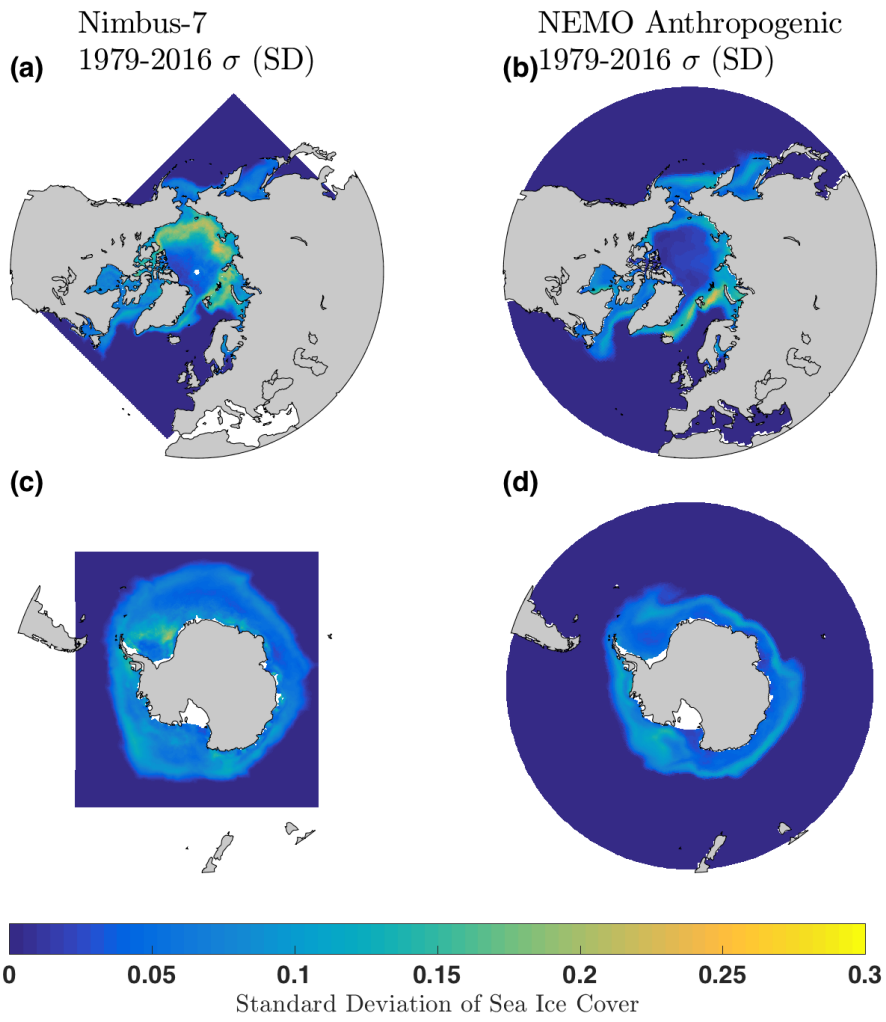

Figure 1.9: Sea ice cover variability calculated as the standard deviation of annual mean cover over 1979-2016 from Nimbus-7 satellite data (*Gloersen*, 2006), left, and the NEMO-MEDUSA Anthropogenic simulation described in Chapter 2, right, for the Northern (a and b respectively) and southern (c and d respectively) hemispheres

duction of dense North Atlantic Deep Water in models is associated with stronger production of Antarctic Bottom Water, allowing southern-sourced waters to penetrate more deeply into the global ocean. The enhanced convective mixing in the Southern Ocean (which results from coarse horizontal grids) results in surface warming because subsurface Southern Ocean waters are warmer than the surface. This is likely to be a key driver of the diminished southern sea ice in the model. Furthermore, the warm and cold biases in the tropical oceans are linked to problems in the representation of the monsoon (*Wang et al.*, 2014). The main biases reported here are therefore common to these types of climate simulations, and do not arise as a result of any particular peculiarity of the setup. As a consequence, these

biases cannot be readily avoided by making simple changes to the configuration or using a different model.

Other work (*Collins et al.*, 2011; *Martin et al.*, 2011) has performed much more thorough and broad-reaching evaluations of the atmospheric forcing set than could be performed within this thesis, and these are summarised here. Note, however, that firsthand validation of the wind fields as they relate specifically to CO_2 flux variability is included in Section 2.3. Multiannual mean fields of key tropospheric variables including geopotential height, zonal winds and temperature show good agreement with observations and reanalysis products, with reasonable performance in pressure at mean sea level and meridional winds (*Martin et al.*, 2011). The main problem troposphere variables are total cloud amount, humidity and precipitation, especially in the tropics, which are difficult to resolve without more robust in situ observations (*Martin et al.*, 2010). The Northern Hemisphere winter storm track activity shows that atmospheric variability in the subpolar North Atlantic is captured well by HadGEM2, Figure 4 in (*Martin et al.*, 2011). The North Pacific storm track is reasonably well modelled in terms of strength and spatial pattern, although it extends too far east, Figure 4 in (*Martin et al.*, 2011). Large scale climatic modes of variability such as El Niño-Southern Oscillation (ENSO) are notoriously difficult to model and remain a high priority of model development (*Martin et al.*, 2011). HadGEM2 features a high bias in westerly wind stress in the western tropical Pacific (*Martin et al.*, 2011). The frequency of large El Niño events, and the magnitude of variability is underestimated, which may stem from an unidentified problem in the process of ENSO phase change (*Collins et al.*, 2008, 2011). Furthermore, ocean-atmosphere feedbacks will not be represented robustly in the ocean-only model used in this thesis, and so conclusions relating to the tropical Pacific must be drawn with appropriate care.

Chapter 2

On which timescales do gas transfer velocities control North Atlantic CO_2 flux variability?

2.1 Introduction

The work described in this chapter is available as a published manuscript in Global Biogeochemical Cycles, see *Couldrey et al.* (2016). All of the technical and analytical elements of the work presented in this chapter are that of the author of this thesis, except the model simulations which were performed by Andrew Yool. All sections of text were written by the author of this thesis, with coauthors of (*Couldrey et al.*, 2016) providing guidance on the interpretation of results, and comments on the text. The content of this chapter hereafter is almost entirely the same as what is presented in (*Couldrey et al.*, 2016), with some minor changes (corrections of typographical errors and small changes of wording to add clarification). Because the chapter is derived from a publication, there are minor differences in language between this chapter and the rest of the thesis (such as a shift in the use of pronouns and American-English spelling conventions).

Since the onset of the industrial era in the middle of the 18th Century, human activities have altered oceanic and atmospheric chemistry, affecting the climate system. Fossil fuel consumption, changes in land use and cement production rapidly release carbon as carbon dioxide (CO_2) gas from geological reservoirs into the atmosphere, oceans and terrestrial biosphere. This adds large amounts of 'anthro-

pogenic carbon' to the biogeochemically and/or radiatively active 'natural carbon' pool. The effects of CO_2 on the Earth system are numerous and complex, but as a 'greenhouse gas' it is a prominent control on climate (*Myhre et al.*, 2013). Of the 555 ± 85 petagrams of carbon emitted to the atmosphere between 1750 and 2011 by human activities, about half has remained in the atmosphere while 28% ± 5% has been taken up by the oceans, with the remainder taken up by the terrestrial biosphere (*Ciais et al.*, 2013).

The flux equation, (2.1), describes the net exchange of CO_2 between the air and the ocean (F). Here, ΔpCO_2 is the disequilibrium between the partial pressures of CO_2 in the air and ocean (pCO_2^{air} - pCO_2^{ocean}). Under this sign convention, an excess of CO_2 in the air gives positive ΔpCO_2 and F, driving exchange into seawater. If pCO_2^{ocean} is greater, outgassing occurs. pCO_2 in seawater is primarily a function of temperature (T), and dissolved inorganic carbon (DIC), but salinity (S) and alkalinity also affect this. The gas transfer velocity, k, is a parameterization of how several aspects the physical environment enable CO_2 flux. Wind velocity is the main variable affecting k (increasing winds increases k), but ice, surfactants, bubbles and other factors also play important roles (*Wanninkhof et al.*, 2009). The Schmidt number (the ratio between kinematic viscosity and molecular diffusion) also affects k, varying with water temperature. α is Henry's constant of CO_2 solubility in seawater (*Weiss*, 1974), quantifying how temperature, salinity and pressure affect solubility.

$$F = \Delta pCO_2 \times k \times \alpha \tag{2.1}$$

CO_2 flux is difficult to measure directly due to the need for high temporal resolution measurements of pCO_2 and small scale turbulence (*McGillis et al.*, 2001), and so a more common approach is to measure or estimate each quantity on the right hand side (RHS) of equation (2.1). α is the most straightforward to determine, varying primarily with temperature, but also with salinity. α's contribution to flux variability is generally well-constrained, and found to be minor on interannual timescales (e.g. *Doney et al.*, 2009). ΔpCO_2 and k, however, present distinct challenges for ocean carbon research. The primary challenge with studying global

ΔpCO_2 variability is to place as many measurement systems in as many locations as possible, and to maintain those observations through time. The Surface Ocean CO_2 Atlas (SOCAT) is an example of a global effort to compile measurements of ocean surface CO_2 gathered by autonomous underway systems on commercial vessels and research cruises (*Bakker et al.*, 2014).

The main difficulties in quantifying gas transfer velocity stem from its dependence on several elements of the physico-chemical environment. The main variable used to derive a gas transfer velocity is wind speed, but k is also dependent on the smoothness of the sea surface (i.e. the presence of breaking and non-breaking waves (*Frew et al.*, 2007)), bubble entrainment, rain, buoyancy generated turbulence, surfactants and other factors (*Wanninkhof et al.*, 2009). Given the large range of variables, and poor constraints of their effects on k, field measurement of gas transfer velocity is difficult. In attempts to refine these uncertainties, several parameterizations have been proposed, derived using a number of techniques, but there is no consensus which is the most accurate (*Bender et al.*, 2011). Instead, authors tend to attempt to quantify k uncertainty in two ways: the uncertainty inherent to a particular parameterization (resulting from the spread of datapoints about the polynomial fitted) and the variation in derived k from the use of different parameterizations. Published uncertainties relating to k are often not statistically sound, and represent ad-hoc best estimates of error (*Wanninkhof*, 2014). The result is that considerable CO_2 flux uncertainty originates from uncertainties in the gas transfer velocity.

While the whole global ocean represents a large net sink of CO_2 for the atmosphere, its uptake is not uniform spatially or temporally. The tropical oceans are net CO_2 outgassing regions, whereas at higher latitudes there is net uptake by seawater (*Takahashi et al.*, 2009; *Landschützer et al.*, 2014). The major upwelling regions are outgassing zones, and the strongest sites of ocean CO_2 uptake are areas of deep water formation. In the North Atlantic, the combination of deep water formation and high biological carbon fixation create ideal physical and biogeochemical conditions for strong ocean CO_2 uptake, distinguishing it from other basins (*Sabine et al.*, 2004; *Khatiwala et al.*, 2009). It is therefore an important focus region in the ocean carbon cycle.

The evolution of the North Atlantic carbon sink on decadal and longer timescales is unclear, yet its quantification is necessary for future climate change prediction (*Halloran et al.*, 2015). *Bates* (2007) and *Takahashi et al.* (2009) call attention to this gap in knowledge, highlighting that a major limitation to our ability to understand this variability stems from limited spatiotemporal coverage of CO_2 observations. Although datasets with large spatial coverage exist (e.g. SOCAT (*Bakker et al.*, 2014)), they lack the temporal duration required to study long timescales (*Halloran et al.*, 2015). Equally, the long timeseries sites with sufficient data to quantify multiannual variability, such as the Bermuda Atlantic Time Series (BATS) and others reviewed recently by *Bates et al.* (2014) may not necessarily represent the systems at the basin scale (*McKinley et al.*, 2004). Given these temporal and spatial data gaps, numerical modelling studies provide unique insight into an incompletely observed system.

It is necessary to understand where observational uncertainties limit our ability to confidently predict future climate change. Previous work investigating global ocean carbon flux interannual variability has found both ΔpCO_2 and k to be important drivers (*Doney et al.*, 2009; *Long et al.*, 2013). Other work has found that North Atlantic multidecadal CO_2 flux variability is controlled chiefly by the contribution from ΔpCO_2 (*McKinley et al.*, 2011). Therefore, on these multidecadal timescales, uncertainty in gas transfer velocity variability does not considerably limit estimates of flux variability, because the contribution from k is minor. On some intermediate critical timescale between interannual and multidecadal, flux variability transitions from a regime that is k- and ΔpCO_2-controlled to purely ΔpCO_2-controlled. Presently, neither the magnitude of this critical timescale nor its spatial structure are known, yet both are needed to understand where uncertainties in ΔpCO_2 and k add uncertainty in derived fluxes.

Here, we attribute CO_2 flux variability to contributions from all flux equation components on a range of timescales, to identify the timescales where k becomes unimportant. We hypothesise that on interannual and shorter timescales, both k and ΔpCO_2 will both be important in controlling flux variability, but that for longer term variability, ΔpCO_2 will be the dominant contributor. We examine 150 years of ocean biogeochemical model output, forced with two scenarios: 1)

sharply rising, following historical measurements and Representative Concentration Pathway 8.5 (RCP8.5) (*Riahi et al.*, 2011) and 2) fixed preindustrial atmospheric CO_2 concentrations. First, we determine that our setup is appropriate to test our hypothesis, comparing observed and modelled variability. Next, we compare our model's representation of interannual flux variability with those of previous studies, before expanding our methodology to examine more specific timescales of variability. We then identify which long timescales of flux variability, if any, are driven entirely by the ΔpCO_2 contribution, with negligible influence from k. Finally, we examine how successfully one can estimate flux variability with only a very limited knowledge of the contribution of k.

2.2 Methods

2.2.1 Model Setup

We investigate the controls of ocean carbon flux variability on different time scales using a numerical ocean general circulation model (GCM); version 3.2 of the Nucleus for European Modelling of the Ocean (NEMO) physical ocean model (*Madec*, 2008). This model includes sea-ice; version 2 of the Louvain-la-Nueve Ice Model (LIM2, (*Timmermann et al.*, 2005)). NEMO was run with a 1° horizontal resolution using the ORCA-1 grid (*Madec and Imbard*, 1996). This grid is not sufficient to resolve the mesoscale, but has a finer scale of about 1/3° of latitude at the equator to better represent equatorial upwelling. The grid has 292 × 362 horizontal points and 64 vertical levels (with smaller spacing at the surface, increasing with depth).

NEMO is coupled with an intermediate-complexity ecosystem model, Model of Ecosystem Dynamics, Utilisation, Sequestration and Acidification (MEDUSA) 2.0 (*Yool et al.*, 2013a). MEDUSA 2.0 separately simulates "large" organisms (mesozooplankton and microphytoplankton like diatoms) and "small" ecosystem members (to represent the microbial loop). MEDUSA 2.0 resolves nitrogen, silicon, iron, carbon, alkalinity and oxygen cycles. The model includes representations of sinking of detrital matter and benthic interactions. The *Nightingale et al.* (2000) gas transfer velocity parameterization is used, with the Schmidt number of *Wannink-*

hof (1992). This parameterization is commonly used as it is considered to be one of the more robust; the function shows a high proportion (82%) the variance of dual-tracer release data explained by wind speed (*Ho et al.*, 2011).

Output from the HadGEM2-ES Earth system model is used as the atmospheric forcing set (*Yool et al.*, 2013b). HadGEM2-ES includes physical models of the ocean and atmosphere, the terrestrial and ocean carbon cycles, tropospheric chemistry and aerosols (*Collins et al.*, 2011). The surface fluxes of heat, momentum and freshwater, and atmospheric chemistry from HadGEM2-ES were used to force NEMO at 6-hourly intervals. The atmospheric forcing set for the 'anthropogenic' run prescribes concentrations of atmospheric CO_2 (and other greenhouse gases: methane, nitrous oxide and halocarbons) following RCP8.5 (*Jones et al.*, 2011). Since this model setup lacks a component to simulate changing greenhouse gas emissions, the system is instead forced with greenhouse gas concentrations from a commonly used projection characterized by large population growth and minimal reductions of emissions. RCP8.5 is a high greenhouse gas concentration scenario, with atmospheric pCO_2 exceeding 900ppm by the year 2100 (*Riahi et al.*, 2011) (Figure 2.1a, green curve). This prescribed anthropogenic source of greenhouse gases into the atmosphere increases planetary radiative forcing by 8.5 Wm^2 by the year 2100 and causes a net rise in global temperatures, including SST (Figure 2.1b). The integration was run for 240 years.

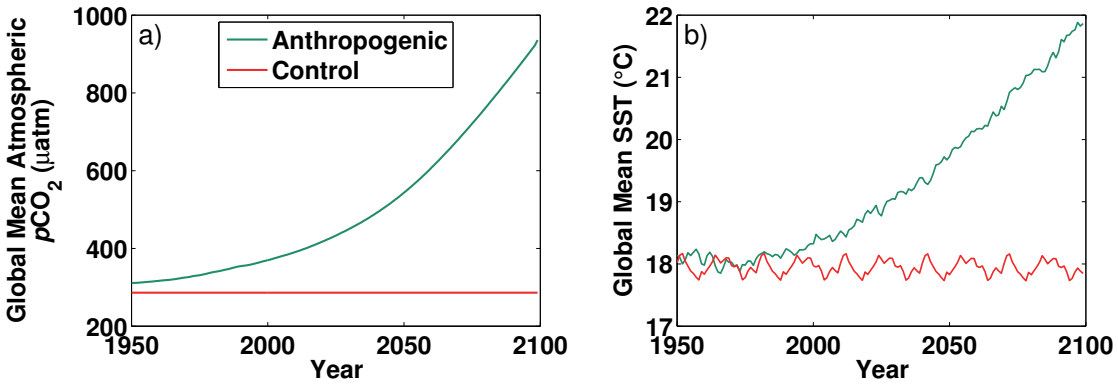

Figure 2.1: Annual mean atmospheric pCO_2 (a) and Sea Surface Temperature (SST, b) for the anthropogenic (green) and control (red) runs, for 1950-2099 (model year 1 is 1860)

A control run was also generated using a very similar setup to the experimental run, except with a different atmospheric pCO_2 scenario. In this run, atmospheric

pCO_2 is held at a preindustrial value of 286 ppmv (Figure 2.1a, red curve). Only 30 years of this forcing set (i.e. output from HadGEM2-ES run with fixed preindustrial atmospheric CO_2) were available to force NEMO-MEDUSA. Therefore, to obtain a comparable 240 year control run, NEMO-MEDUSA was forced with eight repetitions of the forcing set. The control provides insight into the system's internal variability, without forced changes in the radiation budget (observable in global mean SST: Figure 2.1, right panel) and global biogeochemistry. Internal variability in the control run on timescales longer than 30 years is evident as small drifts (e.g. in SST as subtle deviations from the repeating 30 year cycles, Figure 2.1, red curve), but given the forcing setup of this run, it is not included in our analysis.

2.2.2 Decomposition of CO_2 Flux Variability

To explore the drivers behind CO_2 flux variability, we use a Reynolds decomposition to separate the time-varying (y') and time-mean ($\bar{y}$) components of monthly averaged model output, as in equation (2.2). The time-varying component is therefore the monthly anomaly from a time mean, representing non-seasonal variability.

$$y = y' + \overline{y} \tag{2.2}$$

The flux of CO_2 is the product of three variables, equation (2.1). Therefore, a Reynolds decomposition for three forcing components is needed. The generalised decomposition for three components and its expansion is shown in equations (2.3-2.5), where a, b and c are the forcing components, corresponding to the three RHS variables in equation (2.1).

$$\begin{aligned} y &= abc & (2.3)\\ y' + \bar{y} &= (a' + \bar{a})(b' + \bar{b})(c' + \bar{c}) & (2.4)\\ &= \bar{a}\bar{b}\bar{c} + a'\bar{b}\bar{c} + \bar{a}b'\bar{c} + \bar{a}\bar{b}c' + \bar{a}b'c' + a'\bar{b}c' + a'b'\bar{c} + a'b'c' & (2.5) \end{aligned}$$

The time-mean component, $\bar{y}$, is time mean of each of the RHS terms in equation (2.5), as in equation (2.6). Terms in equation (2.6) containing the time means of two forcing components ($\overline{a'\bar{b}\bar{c}}$, $\overline{\bar{a}\bar{c}b'}$ and $\overline{\bar{a}\bar{b}c'}$) always have values of zero, giving equation (2.7).

$$\begin{aligned}
\bar{y} &= \overline{\bar{a}\bar{b}\bar{c}} + \overline{a'\bar{b}\bar{c}} + \overline{\bar{a}\bar{c}b'} + \overline{\bar{a}\bar{b}c'} + \overline{\bar{a}b'c'} + \overline{a'c'\bar{b}} + \overline{a'b'\bar{c}} + \overline{a'b'c'} && (2.6)\\
&= \overline{\bar{a}\bar{b}\bar{c}} + \overline{\bar{a}b'c'} + \overline{a'c'\bar{b}} + \overline{a'b'\bar{c}} + \overline{a'b'c'} && (2.7)
\end{aligned}$$

We subtract $\bar{y}$ from both sides of equation (2.5) to solve for the time-varying component of y, equations (2.8-2.9). This gives an expression for y' in terms of the contributions from separate components, equation (2.10). Note that $\overline{\bar{a}\bar{b}\bar{c}} = \bar{a}\bar{b}\bar{c}$, so the difference between the two terms cancels to zero in equation (2.10).

$$\begin{aligned}
y' &= y - \bar{y} && (2.8)\\
&= (\bar{a}\bar{b}\bar{c} + a'\bar{b}\bar{c} + \bar{a}b'\bar{c} + \bar{a}\bar{b}c' + \bar{a}b'c' + a'\bar{b}c' + a'b'\bar{c} + a'b'c')\\
&\quad -(\overline{\bar{a}\bar{b}\bar{c}} + \overline{\bar{a}b'c'} + \overline{a'c'\bar{b}} + \overline{a'b'\bar{c}} + \overline{a'b'c'}) && (2.9)\\
&= a'\bar{b}\bar{c} + \bar{a}b'\bar{c} + \bar{a}\bar{b}c' + (a'b'c' - \overline{a'b'c'}) + (a'b'\bar{c} - \overline{a'b'\bar{c}})\\
&\quad +(a'\bar{b}c' - \overline{a'c'\bar{b}}) + (\bar{a}b'c' - \overline{\bar{a}b'c'}) && (2.10)
\end{aligned}$$

We arrive at an equation for flux anomalies by expressing anomalies in the flux equation (2.1) using the expansion in equation (2.10):

$$\begin{aligned}
F' &= \underbrace{\Delta pCO_2'\bar{k}\bar{\alpha}}_{term1} + \underbrace{\overline{\Delta pCO_2}k'\bar{\alpha}}_{term2} + \underbrace{\overline{\Delta pCO_2}\bar{k}\alpha'}_{term3} + \underbrace{(\Delta pCO_2'k'\bar{\alpha} - \overline{\Delta pCO_2'k'\bar{\alpha}})}_{term4}\\
&\quad + \underbrace{(\Delta pCO_2'\bar{k}\alpha' - \overline{\Delta pCO_2'\alpha'\bar{k}})}_{term5} + \underbrace{(\overline{\Delta pCO_2}k'\alpha' - \overline{\overline{\Delta pCO_2}\ k'\alpha'})}_{term6}\\
&\quad + \underbrace{(\Delta pCO_2'k'\alpha' - \overline{\Delta pCO_2'k'\alpha'})}_{term7} && (2.11)
\end{aligned}$$

The physical interpretation of these terms is the anomaly in CO_2 flux from a long term monthly mean produced by variability in ΔpCO_2 (term 1), in k (term 2)

and in α (term 3) and through non-linear interactions between components (terms 4 to 7). Rather than consider each of the cross terms (terms 4 to 7) in equation (2.11) separately, we consider their sum as one term. This is because the role of the cross terms (even when added together) in controlling F' is minor, demonstrated in section 2.4.1. When summed, the decomposed contributions reliably reconstruct monthly mean fluxes, suggesting that the decomposition is not compromised by covariances between components of the flux equation and synoptic scale variability.

To investigate how much each term in equation (2.11) contributes to variability in F', we regress the values of terms 1, 2 and 3 at each gridpoint for each month against the monthly flux anomaly at that gridpoint. This method is detailed further by *Doney et al.* (2007) and *Doney et al.* (2009). For example, to solve for the change in y' due to the first forcing component $a'\bar{b}\bar{c}$, we regress the former against the latter:

$$\frac{\partial y'}{\partial a'\bar{b}\bar{c}} = \beta_a \tag{2.12}$$

This yields a slope, β, which quantifies how strongly a given RHS term in equation (2.11) contributes to anomalies in the CO_2 flux. In equation (2.12), the subscripted a denotes that in this example, β_a signifies the change in y' with respect to variability in the forcing component, a. β close to one indicates that a term contributes strongly to the value of F', whereas a slope of 0 shows that F' is insensitive to that term. Values of β may be less than 0 if a term is anticorrelated with F'. In such cases, one or more terms will have slopes greater than 1 to compensate for a different β being smaller than 0. In general, $\Sigma\beta = 1$ (i.e. the linearity assumption of the regression) does not hold due to cross-correlations, but we find that the sum of all slopes is predominantly in the range $0.8 < \Sigma\beta < 1$. This suggests that the assumption of linearity in the response of y' to its predictors is effectively met.

2.3 Validation

Previous work has compared output from MEDUSA 2.0 to biogeochemical observations on global and regional scales in more detail (*Yool et al.*, 2013a), which we briefly summarise before elaborating our own validation. In general, the model

captures much of the spatial and seasonal patterns of primary productivity, but shows a low bias in the subtropics, a high bias in high nutrient/low chlorophyll regions and underestimates the strength of the North Atlantic spring bloom. MEDUSA 2.0 tends to show 'higher highs' of surface DIC than the GLODAP (*Key et al.*, 2004) fields ((*Yool et al.*, 2013a), their Figure 16), but the broader spatial patterns are well reproduced. Similarly, air-sea ΔpCO_2 seasonal highs and lows are somewhat exaggerated, particularly the North Atlantic winter ((*Yool et al.*, 2013a), their Figures 21 and 22). While these findings are useful to bear in mind, our study focuses on carbon flux variability on interannual and longer timescales that has not been thoroughly validated.

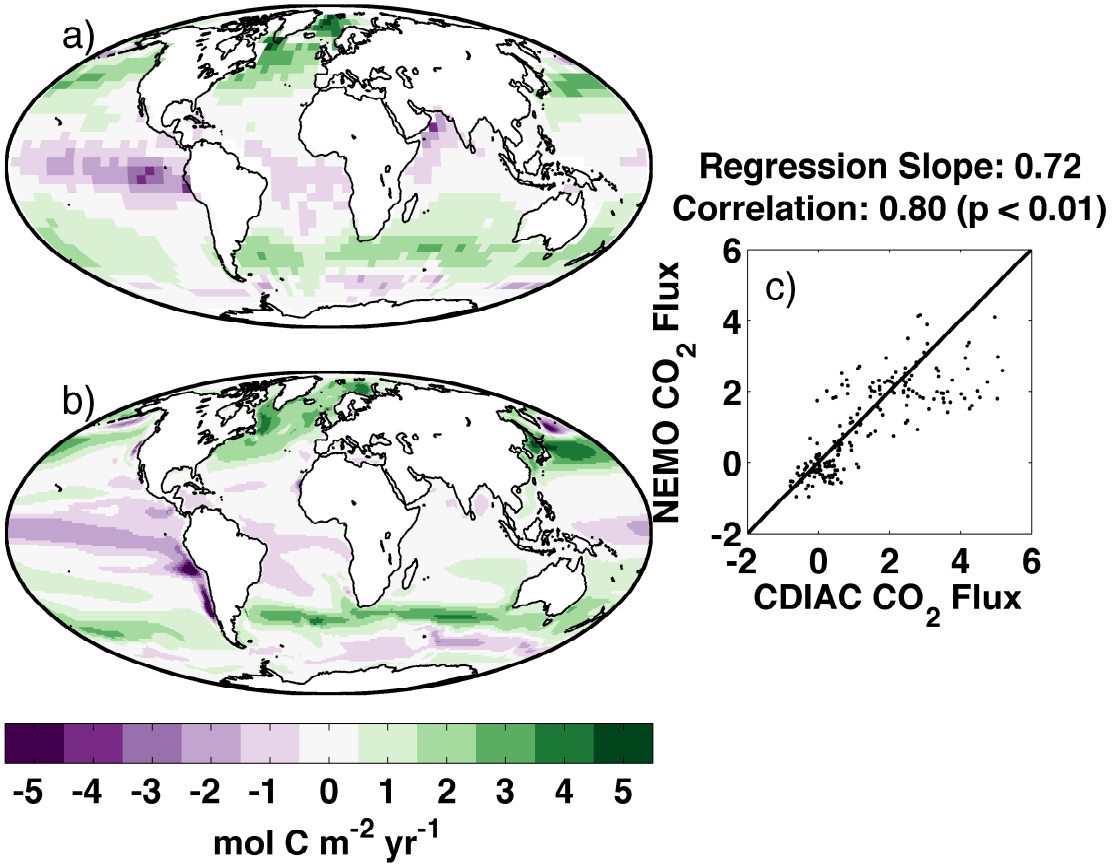

Figure 2.2: a) LDEO climatological flux of CO_2 into the ocean for the reference year 2000, positive values indicating ocean uptake of gas, (*Takahashi et al.*, 2009), b) Modelled mean CO_2 flux over 1995-2005 for the anthropogenic run, c) LDEO versus modelled North Atlantic climatological CO_2 flux (mol C m^{-2} yr^{-1})

We first assess the ability of our setup to reproduce the major spatial features of the climatological CO_2 flux by comparing observational time-mean fluxes (the Lamont-Doherty Earth Observatory, or LDEO flux climatology (*Takahashi et al.*, 2009)) with model output (Figure 2.2). The most prominent large-scale features

are well represented in our model: low latitude efflux and high latitude influx. Some of the largest discrepancies between the model and observations occur in the South Pacific, where measurements are sparse. For the purposes of our study, these differences are unimportant, since we focus on the North Atlantic. After interpolating the model North Atlantic CO_2 flux climatology onto the coarser grid of the Takahashi observational climatology, the two can be compared quantitatively. The North Atlantic climatological CO_2 flux is one of the best represented basins in our setup; here, the model somewhat underestimates high values of flux, but otherwise the two are well correlated (with a correlation coefficient r value of 0.80, $p < 0.01$) (Figure 2.2c).

Next, we attempt to validate the model's temporal variability. Direct CO_2 flux observations representing large spatial and temporal scales do not exist, so instead we validate our model's fCO_2 fields (CO_2 fugacity is almost equivalent to pCO_2, but is scaled for the non-ideal nature of real world gases). The model uses only pCO_2 in its calculations for simplicity, but for this comparison only fields of model fCO_2 are calculated from pCO_2 using standard tools (*van Heuven et al.*, 2011a). We compare our model output against 1) the SOCAT database of surface fCO_2 observations (which maximises spatial coverage at the expense of temporal length) (*Bakker et al.*, 2014) and 2) data collected at the BATS site (to compare variability on the longest timescale possible, although only for a limited area). We compare fields of fCO_2 rather than ΔpCO_2 because in our setup, the atmospheric pCO_2 only varies with the increase prescribed under RCP8.5, and so all of the modelled ΔpCO_2 variability arises from the oceanic side. Spatial and temporal (other than the trend) variability in atmospheric pCO_2 are omitted in our setup, but are small (order 1-10 ppm) in comparison to the oceanic pCO_2 variability of interest (order 10-100 ppm) (*Wanninkhof et al.*, 2013).

We compare our model output with $1{\times}1^\circ$ monthly mean gridded fCO_2 fields from the SOCAT database (version 2) (*Bakker et al.*, 2014). For this comparison, we first regrid our model output onto the SOCAT grid. Although the dataset includes values from the 1970s, the most consistent temporal coverage in the North Atlantic is between 2002 and 2011. We choose three locations in zonally distinct regions on the basis that they had the most complete set of observations for this

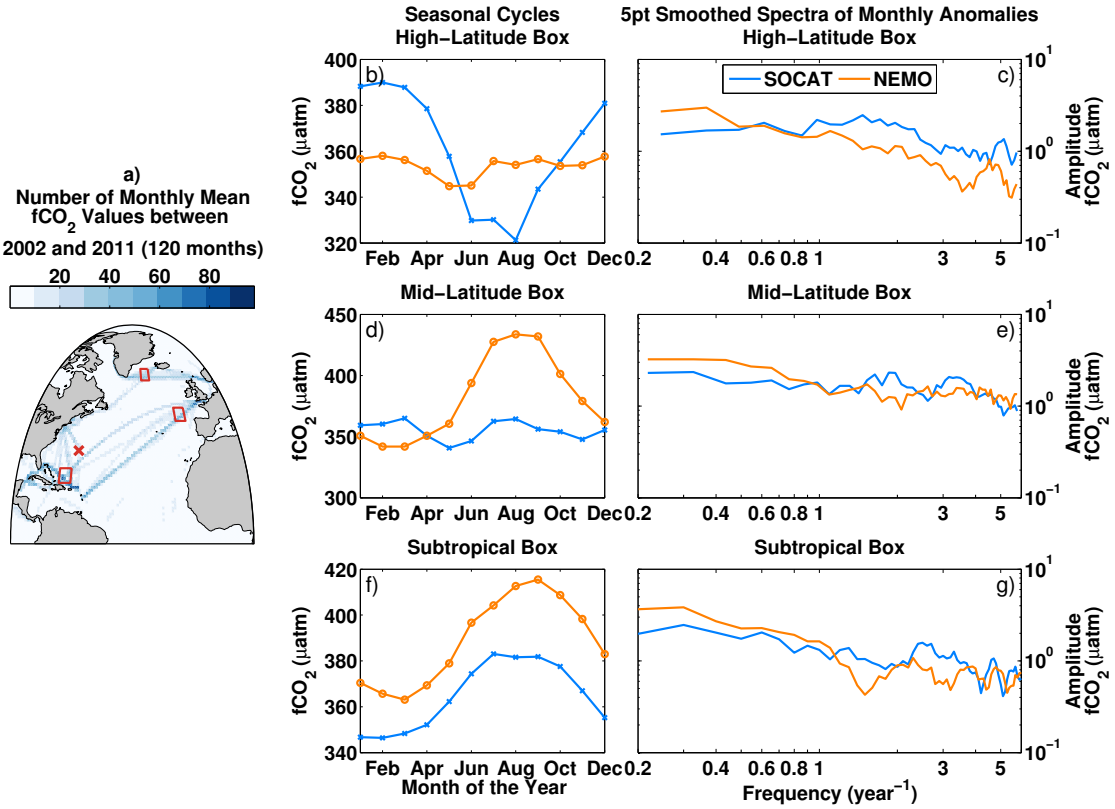

Figure 2.3: Comparison of data from the SOCAT database and output from the anthropogenic run. a) Coverage of SOCAT monthly mean fCO_2 values 2002-2011, orange squares: locations of comparison regions, orange cross: location of BATS site. b), d) and f), Monthly mean fCO_2 climatologies for the three comparison regions (high-latitude, mid-latitude and subtropical, respectively) for 2002-2011: for SOCAT (blue) and NEMO-MEDUSA (orange). c), e) and g), frequency spectra of monthly fCO_2 anomalies, smoothed with a 5 point running mean

period. We select data from 5×5° degree areas across the North Atlantic (subtropical: northeast of the Carribbean, mid-latitude: west of the Bay of Biscay, and high-latitude: south of Greenland/Iceland) to compare against our model output (Figure 2.3a, orange boxes). The comparison is insensitive to the exact location of the boxes (shifting their positions by a few degrees gives similar results), and the time period of model output used. It was not possible to apply this comparison to the equatorial Atlantic, as there were insufficient monthly mean fCO_2 values (Figure 2.3a). We calculate a monthly climatology of time mean fCO_2 fields (Figure 2.3b, d and f), and monthly anomalies from this climatology for the 2002-2011 period. We then calculate frequency spectra of the fCO_2 anomalies for each box (Figure 2.3c, e and g). Data gaps were filled with that month's mean value, plus the contribution of the linear trend. Where gaps existed in the SOCAT data, the model output was accordingly subsampled and the resulting gaps were filled in the

same way as for the observations.

Clear differences exist between the modelled and observed seasonal cycles of fCO_2 (Figure 2.3b, d and f). These differences are unimportant for our study, which does not focus on seasonal variability. The comparison between the frequency spectra of the model output and the observations is similar across all boxes: high frequency (short timescale) variability is similar or slightly higher in observations, and low frequencies (long timescales) show slightly more energy in the model. The discrepancies at high frequencies are unsurprising, as the observations will reflect features that are unresolved by the model, such as mesoscale eddies. Although the fCO_2 variability at low frequencies is larger in the model, the agreement with observations is within a factor of 2.

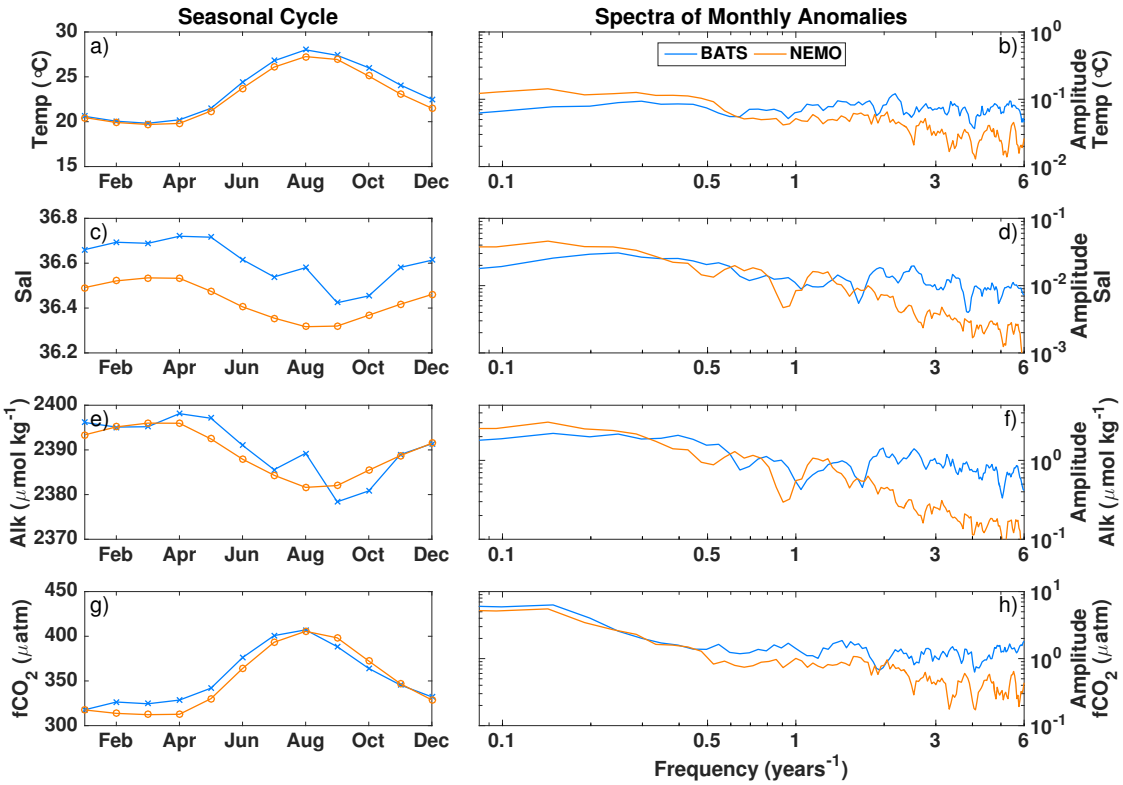

Figure 2.4: Comparison of (from top to bottom) Temperature, Salinity, Alkalinity and fCO_2 from BATS, Bermuda (blue) with corresponding NEMO-MEDUSA anthropogenic run output (orange). a), c), e) and g), Climatological monthly means for 1991-2011. b), d), f) and h), 5 point smoothed frequency spectra of monthly anomalies for 1991-2011

The carbon system data collected at BATS, Bermuda (64° W, 31.5° N), are among the longest and most consistent, covering the years 1991 to 2011. The seasonal cycle amplitudes of all four parameters are well resolved in the model,

with systematic offsets in salinity and alkalinity (Figure 2.4c, e). Non-seasonal variability is well represented (Figure 2.4b, d, f and h). As with the SOCAT-NEMO comparison, there is substantial high frequency variability in the observations not present in the model output, since the former represents snapshots of real world features, while the latter represents monthly-mean output from a 1×1° model grid cell. Overall, the model tends to underestimate sub-annual variability, but captures the amplitudes on longer timescales that are relevant for this study.

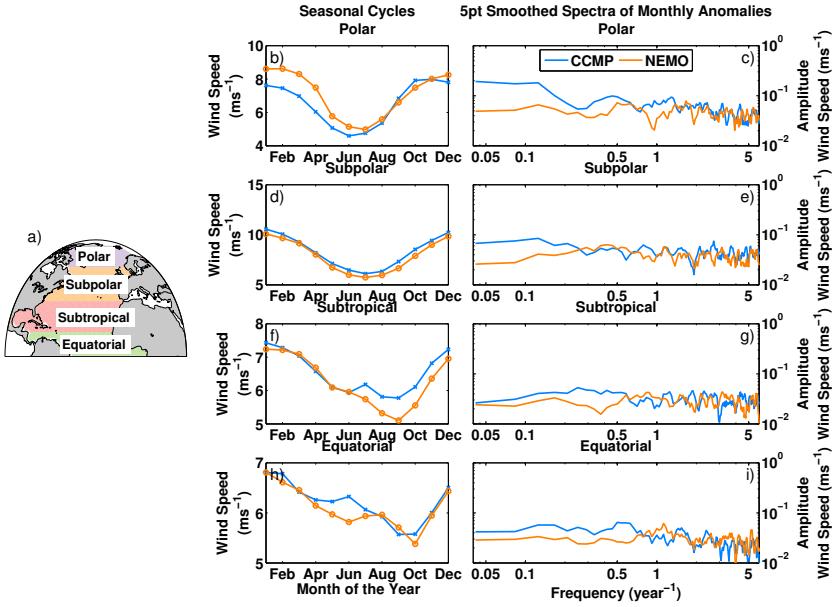

Figure 2.5: Comparison of wind variability from the CCMP wind product (*Atlas et al.*, 2011) and the anthropogenic run. a) Division of zones. b), d), f) and h), Monthly mean wind speed climatologies for the four zonal areas (Polar, Subpolar, Subtropical and Equatorial, respectively) for 1988-2011: for CCMP (blue) and NEMO-MEDUSA (orange). c), e), g) and i), frequency spectra of monthly wind speed anomalies, smoothed with a 5 point running mean

The gas transfer velocity is primarily a function of wind speed, so it is important that our setup reproduces realistic wind fields and variability. Other work has explored the performance of the HadGEM2 models more generally (*Martin et al.*, 2011; *Collins et al.*, 2011). We compare the wind fields used to force NEMO-MEDUSA with monthly mean Cross-Calibrated Multiplatform (CCMP) sea surface (10m) winds (*Atlas et al.*, 2011), which cover the period 1988-2011. CCMP zonal wind speed variability is similar to other products' (*Wanninkhof et al.*, 2013), and so our comparison would likely produce similar results if other wind datasets were chosen. We regrid the data from its 0.25×0.25° grid onto a 1×1° grid for comparison with our model output. We construct a monthly climatology and fields

of anomalies of wind speeds. Similarly to the other aspects of the validation, we construct frequency spectra of the model and observation anomaly fields (Figure 2.5). In general, agreement between the model and observations is good for variability with frequencies higher than 0.25 year^{-1}, and somewhat poorer for lower frequencies (longer timescales). In the subpolar and polar North Atlantic, the model underestimates low frequency wind variability.

2.4 Results

2.4.1 The roles of flux components in interannual variability

In this section, we investigate the drivers behind interannual CO_2 flux variability, quantifying the contributions of its components, ΔpCO_2, k and α. This approach builds on the methodology of *Doney et al.* (2009), attributing interannual flux variability to each component. First, we establish that our model setup is able to represent CO_2 flux variability comparable to previous estimates using the portion of the simulation which overlaps the observational record.

Table 2.1: Comparison of global interannual variability (RMS or Standard Deviation of monthly CO_2 flux anomalies) from various studies

Variability (Pg C yr^{-1})	**Approach**	**Time Period**	**Reference**
0.20	Model	1979-1997	(*Le Quéré et al.*, 2000)
0.23	Model	1961-1998	(*Obata and Kitamura*, 2003)
0.28	Model	1980-1998	(*McKinley et al.*, 2004)
0.34	Model	1979-2004	(*Doney et al.*, 2009)
0.20	Obs and Model	1990-2009	(*Wanninkhof et al.*, 2013)
0.31	Observations	1993-2008	(*Rödenbeck et al.*, 2014)
0.12	Observations	1998-2011	(*Landschützer et al.*, 2014)
0.29	Model	1980-2009	This Study

To assess global CO_2 flux interannual variability, we calculate the root mean square (RMS) or standard deviation of globally integrated monthly flux anomalies. From monthly averaged CO_2 flux fields at each gridpoint, we subtract a long-term mean flux (spanning 1980-2009) for each month to generate anomaly fields. For this time period, variability is insensitive to the choice of RCP because the scenarios

have not yet substantially diverged (*Myhre et al.*, 2013). We globally integrate those flux anomalies, and calculate the square root of the mean squared anomaly, yielding the RMS. The metric is quite sensitive to the duration over which it is calculated. We calculate the RMS over a similar time period to other studies (1980 to 2009), finding a value of 0.29 Pg C yr^{-1}, comparable previous estimates (Table 2.1). Two recent observational estimates of interannual flux variability differ by a factor of two ((*Rödenbeck et al.*, 2014) and (*Landschützer et al.*, 2014)), which the authors attribute to differing time periods of study. *Landschützer et al.* (2014) comment that their data do not cover the strong 1997/1998 El Niño period, which made the *Rödenbeck et al.* (2014) estimate much larger.

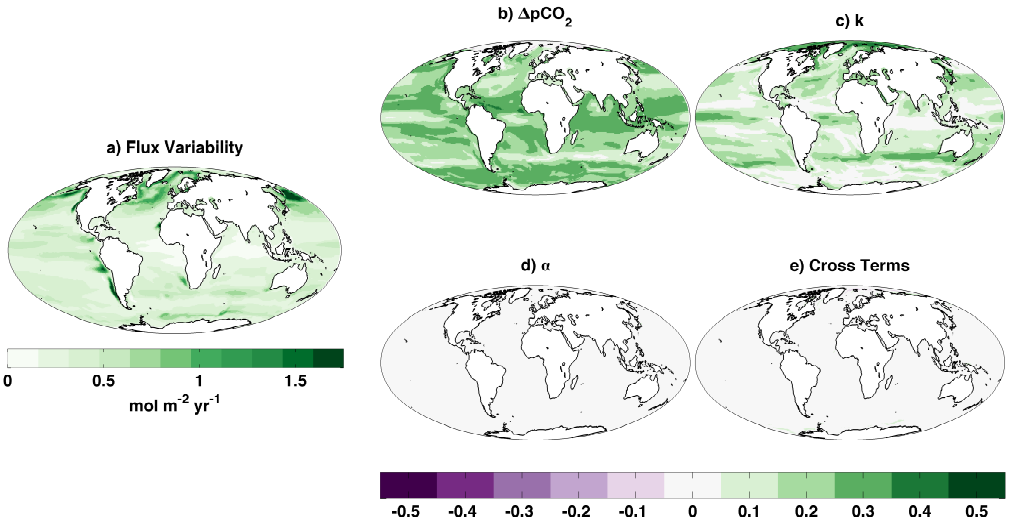

Figure 2.6: Model interannual CO_2 flux variability as the RMS of deseasonalised monthly anomalies (a) and contributions of ΔpCO_2, k, α and cross terms (b to e) to interannual variability in the CO_2 flux for the period 1980-2009 of the anthropogenic run, as in equation (2.12)

Qualitatively, our setup captures many of the key regional hotspots of interannual variability between 1980-2009 (Figure 2.6a): the equatorial Pacific, the subpolar and subtropical oceans, and the south Southern Ocean (e.g. *Doney et al.*, 2009; *Rödenbeck et al.*, 2014). The North Atlantic is a notable region for its large interannual CO_2 flux variability. The areas with the strongest variability (>1.0 mol m^{-2} yr^{-1}) are in the subpolar gyre, along the sea ice edge of the Labrador Sea, along the Greenland coast and along the path of the North Atlantic Current (NAC). The subtropical gyre shows a relatively moderate level of variability (up to 1 mol m^{-2} yr^{-1}) which decays with distance from the NAC. The equatorial Atlantic

shows the lowest overall CO_2 flux variability.

To investigate the causes of the interannual variability illustrated in Figure 2.6a, we estimate the contribution of each component of the flux equation (2.1) using the linear expansion of F' (equation (2.11)). At each grid point for all months, we calculate the contribution of each term in equation (2.11). Taking each of these contributions, we regress them against the gridpoint's monthly CO_2 flux anomalies (F') to quantify the influence of that particular term on F', as in equation (2.12). This allows us to compare the contributions of ΔpCO_2, k, α and the cross terms (Figure 2.6b-e, respectively) to variability in F'.

Over much the global ocean, ΔpCO_2 is the most important contributor to interannual CO_2 flux variability (Figure 2.6b), in agreement with the findings of *Doney et al.* (2009). The global area-weighted mean ΔpCO_2 contribution is 0.20 mol m^{-2} yr^{-1}; about 60% of the global interannual CO_2 flux variability. The role of k is also important in almost all regions, contributing about 35% of global interannual flux variability, but is the most significant where the role of ΔpCO_2 is smaller (2.6c). Indeed, Figure 2.6b and c mirror each other, since nearly all interannual variability in the CO_2 flux comes from variability in either ΔpCO_2 or k. This is because the contributions from α and the cross terms are minor (Figure 2.6d and e). Furthermore, most of the variability observed when considering k and α together as one component comes from k, as was assumed by *Doney et al.* (2009).

Many of the locations where k is an important driver behind interannual CO_2 flux variability coincide with the edges of the seasonally ice-covered oceans. This is because k is scaled by the proportion of each ocean grid cell area that is ice-free. Away from ice edges, k is an important control on F' in such locations as the tropical Pacific and the storm track of the North Atlantic (and to a lesser extent the Pacific). Here, interannual variability in winds is considerable, probably associated with low-frequency modes of climate variability such as the ENSO and the NAO, respectively.

Overall, this analysis yields findings that agree with many of those of *Doney et al.* (2009) insofar as that interannual variability in the global oceanic flux of CO_2 is controlled primarily by ΔpCO_2, but that k contributes about 40% of this. In the

following section, we build upon these findings, exploring the longer multiannual to multidecadal timescales of variability, with an emphasis on the North Atlantic.

2.4.2 Critical timescale of ΔpCO_2 dominance of CO_2 flux variability

In this section we identify at what time scale, if any, does variability in F become dominated by variability in ΔpCO_2. To explore which parameters dominate flux variability over specific timescales, we average each component's contributions (i.e. $\Delta pCO_2' \bar{k} \bar{\alpha}$ for the contribution of ΔpCO_2, etc.) over various zonal areas to obtain mean contributions on the sub-basin scale. We define zones as polar (Baffin Bay and the Greenland-Iceland-Norwegian (GIN) Sea), subpolar (60° N-35° N), subtropical (35° N-10° N) and equatorial (10° N-10° S) (Figure 2.7a). We construct frequency spectra of these zonal mean contributions to quantify the energy of each contribution at specific timescales. Since the contributions from each component are in units of CO_2 flux (mmol m^{-2} d^{-1}), one can compare their magnitudes directly. We also employ Welch's method of segmenting signals to better constrain estimates of the spectra (*Welch*, 1967). Briefly, this involves segmenting a signal into shorter segments of equal length, calculating the spectra of each segment and then averaging over all segments' spectra to obtain one more robust estimate of the spectrum. In our case, we segment the 150 year series of zonally averaged CO_2 flux anomalies and the contribution from k into 5 non-overlapping segments of 30 year length. This method improves the confidence intervals of the spectrum calculated at the cost of being unable to solve for variability on timescales longer than the segment length. This is because the timescales of interest correspond to the lowest frequencies of variability, and so we plot the spectra in period space to highlight this end of the domain.

Across the North Atlantic, most of the variability in CO_2 flux is attributable to the contribution from either ΔpCO_2 or k; the roles of α and the cross terms are minor (not shown). Therefore, almost all of the spectral energy in CO_2 flux anomalies (Figure 2.7b-e, blue lines) that does not correspond with the spectrum of k (red) is attributable to the contribution from ΔpCO_2. In other words, where the energy in CO_2 flux anomalies is high, but the energy of k's contribution is

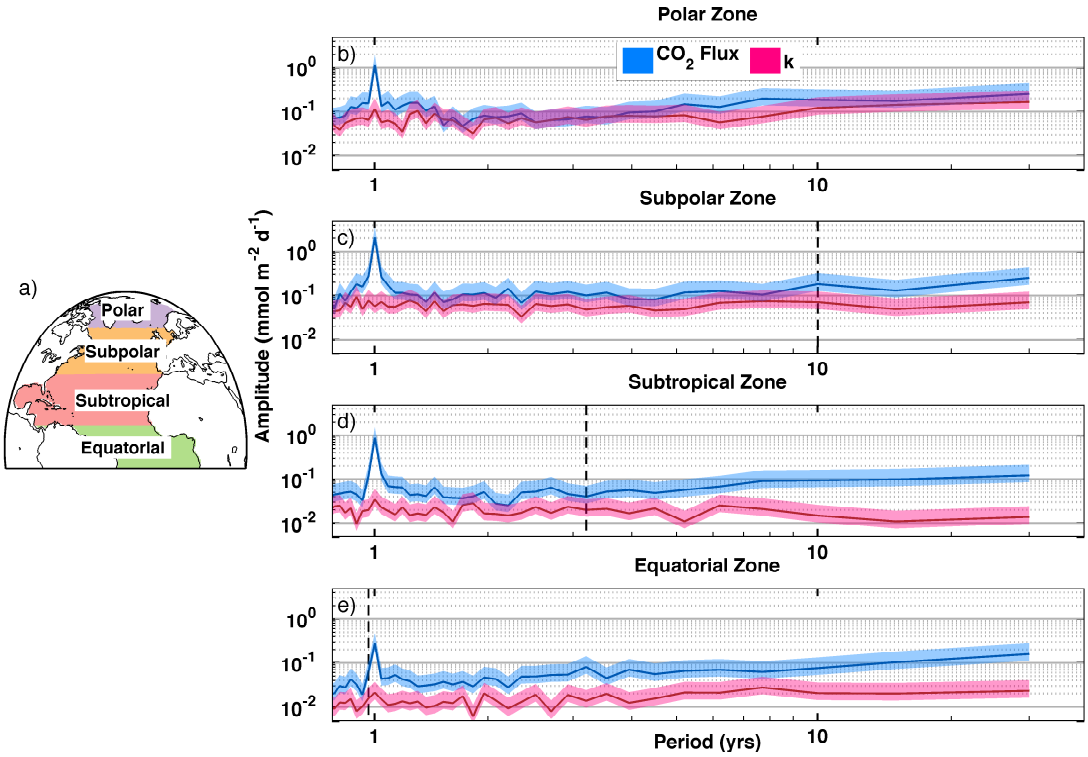

Figure 2.7: Model North Atlantic zones (a) and their period spectra of zonally averaged CO_2 flux (blue), and the contribution to flux variability from k (red) for in the anthropogenic run, 1950-2099 (b-e). The dark coloured lines denote best estimates of spectra, lighter shaded regions show the spectra within 95% confidence. Vertical dashed lines indicate the critical timescale: the shortest timescale that for all longer timescales, the best estimate of CO_2 flux variability is at least twice as large as that of k

lower, most of the discrepancy comes from the contribution of ΔpCO_2. In general, the long period CO_2 flux variability comes from the variability of ΔpCO_2, rather than k. We quantify the CO_2 flux variability that is dominated by the contribution from ΔpCO_2 as being the shortest period of variability where the amplitude of F' variability is at least twice as large as the contribution from k for all longer periods. A factor of two was chosen as it identifies the point at which a clear majority (at least half) of flux variability is attributable to the ΔpCO_2 contribution. To do this, we search along the spectrum from long to short periods for the first period where the spectrum of F' is equal to or less than double the energy of the contribution from k. The vertical dashed lines in Figure 2.7b-e show the value of this critical timescale for each zonal band. If this number is small, then it means a wider band of long period CO_2 flux variability is controlled entirely by ΔpCO_2.

In the equatorial and subtropical latitudes, a very wide band of long-period variability in CO_2 flux is controlled by ΔpCO_2 (all timescales to the right of the vertical dashed lines in Figure 2.7c-e). That is to say that the roles of k and α are negligible for these long periods. The same is also true at subpolar latitudes, but the band of timescales is narrower: approximately decadal and longer-term variability in CO_2 flux is almost entirely controlled by ΔpCO_2. The separation of the (95% confidence) error envelopes around the best estimates of the subpolar, subtropical and equatorial spectra (darker blue and pink lines) indicate that the differences between the spectra at the large-period end are significant. For the polar zone, both ΔpCO_2 and k have an important role in driving flux variability for all timescales longer than interannual (even without curtailing the series length by segmentation), and so there is no long period dominated by ΔpCO_2. In addition to the strong influence of ΔpCO_2, there is also long period variability in k. As k is scaled by sea-ice cover, a negative trend in ice area (in response to a warming climate) will therefore force F' in the long term at high latitudes. Such a decline has been documented in this model setup (*Yool et al.*, 2013b). Taken over the whole North Atlantic, we find that flux variability on pentadal and longer timescales is greatly dominated by the influence of ΔpCO_2, and k contributes to less than quarter of long period flux variability.

To more fully interpret the spectra of zonally averaged contributions, it is helpful to examine the critical timescale of ΔpCO_2 dominance at each grid point for the anthropogenic run (Figure 2.8a). At the grid-point scale, one can infer which physical phenomena give rise to the spectra in Figure 2.7. The polar zone in both runs is dominated by points with no long timescale of ΔpCO_2 dominance: much of Baffin Bay and the western GIN Sea. These regions are strongly influenced by sea ice, but in the eastern ice-free GIN Sea long-period variability is dominated by ΔpCO_2.

The subpolar zone features a southwest-to-northeast band of gridpoints whose flux variability is only dominated by ΔpCO_2 on multidecadal timescales (higher than elsewhere in the basin). This location coincides with the southern boundary of the NAC. Here, there is long period variability in wind speeds in the model, which drives the critical timescale of ΔpCO_2 dominance in the subpolar zone ($\sim$10

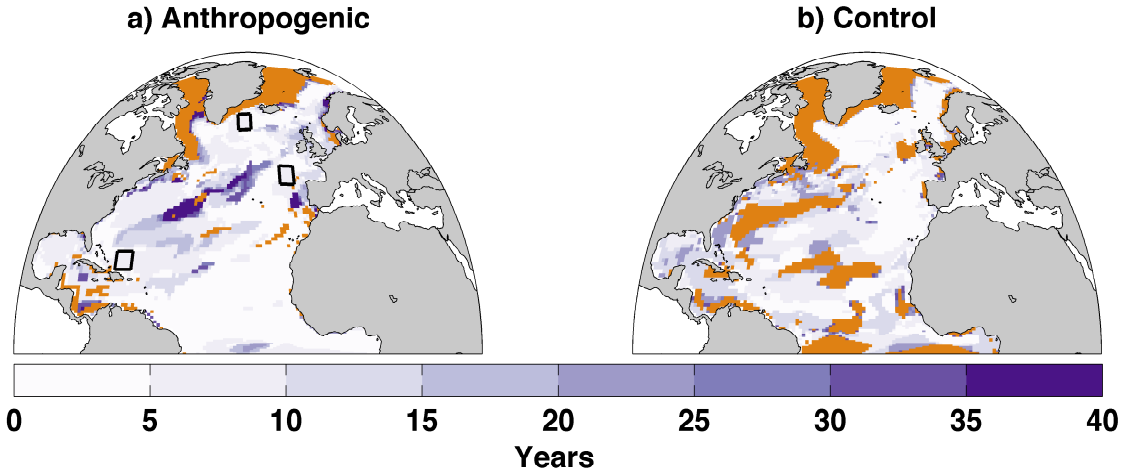

Figure 2.8: Largest timescale of CO_2 flux variability for which the contribution of k is non-negligible, beyond which variability is dominated by ΔpCO_2 for the anthropogenic (a) and control (b) runs. Shades of purple indicate this timescale, orange areas show where ΔpCO_2 never dominates on the longest timescales and white non-Atlantic areas are out of bounds. Colors inside the three black squares in a) show the timescale derived using observations in the same locations as Figure 2.3 (CCMP winds (*Atlas et al.*, 2011), SOCAT oceanic pCO_2 (*Bakker et al.*, 2014), MLO atmospheric pCO_2 (*Thoning et al.*, 2014), and EN4 SST (*Good et al.*, 2013))

years) to be longer than the subtropical or equatorial zones (∼3 and ∼1 years respectively).

We also estimate the critical timescale using observations in the three locations described in section 2.3. In the three 5-by-5 degree areas with the largest number of SOCAT monthly mean fCO_2 values, we construct and decompose CO_2 fluxes using these fCO_2 data (as in Figure 2.3), monthly mean CCMP winds, SST values from the EN4 gridded dataset (*Good et al.*, 2013), and atmospheric pCO_2 from Mauna Loa, Hawai'i (*Thoning et al.*, 2014). In these locations, there is a sufficient history of ocean fCO_2 data to determine the critical timescale: 2 years in the subtropical box, 0.5 years in the mid-latitude box and 4 years in the high latitude box (values shown as color within black squares in Figure 2.8a). These values are comparable to those determined using model output in the same locations; 4.6, 3.7 and 4.6 years, respectively.

By examining the same metric for the control run, we can learn the extent to which ΔpCO_2 controls natural variability in the global ocean, without the influence of anthopogenic CO_2 input. For much of the North Atlantic, ΔpCO_2 variability controls most of the CO_2 flux variability in the control run (Figure 2.8b). Due to

the construction of the control run, it is not possible to comment on variability on timescales longer than 30 years, yet this period is sufficiently longer than the ΔpCO_2 critical timescale for most of the ice-free North Atlantic. This means that natural, internal ocean multiannual CO_2 flux variability is quite insensitive to the contribution from k, and therefore that much of the control exerted by the ΔpCO_2 is not purely the product of anthropogenic emissions. In other words, the strong influence of the ΔpCO_2 in many parts of the North Atlantic is naturally occurring, and not purely due to rising atmospheric carbon concentrations. Such variability in ΔpCO_2 may arise without a rise in atmospheric pCO_2 due to ocean circulation (particularly horizontal and vertical advection). Advection acts to reorganise the surface inventories of heat, DIC and alkalinity, thereby modulating ocean pCO_2 (*Doney et al.*, 2009; *Halloran et al.*, 2015).

2.4.3 CO_2 flux estimation with simplified k

Here, we explore the extent to which flux variability can be reliably estimated in circumstances where we have a minimal knowledge of the variability in gas transfer velocity. In section 2.1, some of the uncertainties associated with k were outlined. A key question is understanding the extent to which those uncertainties limit our ability to estimate oceanic CO_2 flux variability. We can approximate equation (2.11) by assuming that variations in the gas transfer velocity (k') and the role of the cross terms (terms 4 to 7) are small (demonstrated in section 2.4.2). Under these assumptions, terms 2, 4, 5, 6, and 7 vanish, yielding equation (2.13).

$$F' \approx \Delta pCO_2' \bar{k} \bar{\alpha} + \overline{\Delta pCO_2} \bar{k} \alpha' \tag{2.13}$$

If these assumptions are valid and equation (2.13) is a reasonable approximation, the uncertainties associated with k would also become irrelevant in the determination of flux variability. This estimation would be useful in estimating multidecadal flux variability using limited observations, or simple box models. The 'true' simulated CO_2 flux is known in the model, and we are therefore able to determine the error due to the approximation in equation (2.13). By omitting some contributions, the estimated flux will necessarily have less variability than the actual

flux. We therefore assess our estimation by quantifying at each grid point 1) the correlation coefficient (r values) between estimated and model actual fluxes that are significant beyond a level of 95% confidence and 2) the proportion of the flux variability that is captured by the estimation relative to the model's actual flux variability. The error in observational reconstructions of CO_2 flux is likely to differ due to the parameterization of gas transfer in the model, but the model validation (section 2.3) indicates that the statistical properties of the error should be similar on interannual to decadal timescales.

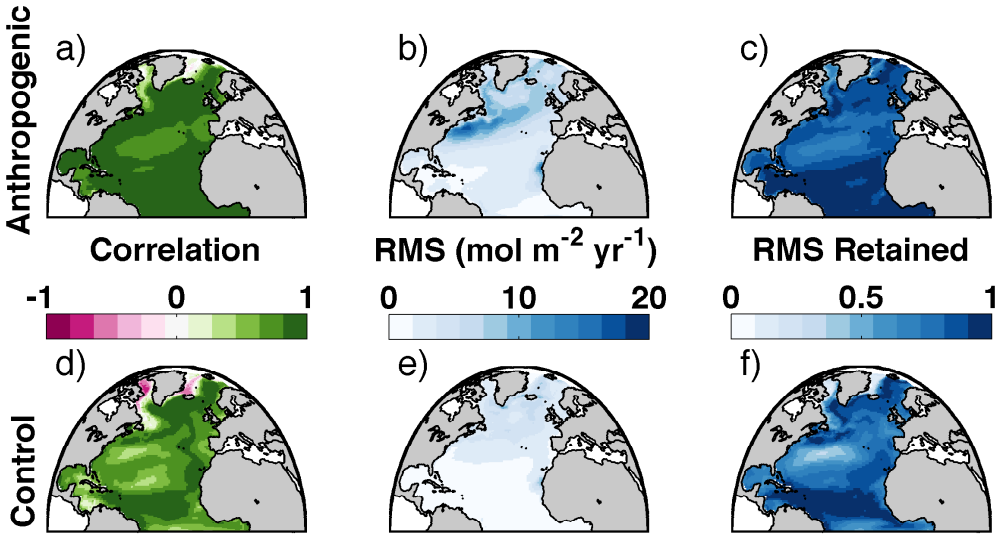

Figure 2.9: Evaluation of flux estimation applied to the anthropogenic (a-c) and control (d-f) runs, 1950-2099. a) and d), correlation between modelled and estimated fluxes (all values are >95% significance). b) and e), RMS of modelled CO_2 flux anomalies (a measure of variability). c) and f), ratio between estimated and modelled CO_2 flux RMS (the proportion of variability captured by the estimation)

The longest-term variability in the North Atlantic CO_2 flux is primarily controlled by the positive trend in atmospheric pCO_2. Correspondingly, the estimated CO_2 flux correlates very closely with the model's actual series (Figure 2.9a). However, even without this trend (as in the control run), the actual and estimated fluxes correlate well (Figure 2.9d). In general, the correlations are weaker in the control than in the anthropogenic run, and several local minima are apparent; these also correspond to regions where variability is generally small (Figure 2.9b and f). The good correlation between estimated and actual fluxes in both the anthropogenic and control runs suggest that the estimation captures the key patterns of flux variability; both anthropogenically and internally driven.

In addition to reproducing patterns of flux variability, it is also necessary for the estimation to correctly predict magnitudes. Since the estimation omits some contributions, it will naturally show either equal or lower variability than the actual flux. To quantify this, we show the ratio between the estimated and actual modelled CO_2 flux variability (as the RMS of monthly anomalies) (Figure 2.9c,f). Where the value is 1, the estimation reproduces all the modelled variability; values between 0 and 1 indicate the proportion of variability retained by the estimation. This metric indicates that the estimation is robust at reproducing most of the modelled variability across the Atlantic, in both the anthropogenic and control runs.

The main area where the flux estimation fares poorly is in the ice-covered North Atlantic. Here, non-seasonal sea ice variability is an important control on fluxes. Our estimation implicitly excludes interannual variability in the ice edge and the multidecadal decline of ice extent, so the fluxes in the region are not well represented. To the south of the NAC there are local minima in correlations and the RMS retained, which are more pronounced in the control run than the anthropogenic. Although these areas are less well estimated than elsewhere in the Atlantic, the variability in these regions is small, and so flux variability on the basin and sub-basin scale will still be well captured.

2.5 Discussion

Presently, large uncertainties are introduced into calculated CO_2 fluxes via the gas transfer velocity. The choice of wind speed parameterization can vary k by approximately 50% at global mean wind speeds ($\sim$7 m/s) and by 100% at speeds higher than 15 m/s (e.g. *Woolf*, 2005). The choice of wind product can affect k by 10-40% (*Wanninkhof et al.*, 2002), and variability differs between products (*Wanninkhof et al.*, 2013; *Wanninkhof*, 2014; *Kent et al.*, 2013). The roles of breaking waves and bubbles are not taken into account when using a purely wind speed-based parameterization of k, so these phenomena introduce poorly constrained uncertainty (*Prytherch et al.*, 2010). Certainly, these factors all limit our ability to accurately estimate CO_2 flux variability on interannual and shorter timescales, and ongoing work is needed in these areas.

In the high-latitude North Atlantic, the gas transfer velocity controls CO_2 flux variability on longer timescales than elsewhere in the basin. In the regions of the Labrador Sea, Baffin Bay, Denmark Strait and Fram Strait, sea ice cover is an important mediator of gas exchange. Here, long period variability in sea ice cover controls CO_2 flux variability via the gas transfer velocity, since k is scaled by the fraction of area that is ice-free. As a result, there is no long period of variability over which ΔpCO_2 predominantly controls the carbon flux. Therefore, to accurately quantify estimates of the high-latitude North Atlantic carbon flux, a detailed knowledge of sea ice dynamics is necessary.

Over the whole North Atlantic, pentadal and longer-term CO_2 flux variability is dominated by the influence of ΔpCO_2. These longer timescales contrast the shorter, where the role of k is crucial. This suggests that a detailed knowledge of the pentadal to multidecadal control of k on F may not be necessary to quantify the longer term variability of the North Atlantic carbon sink. This finding therefore lends support to the approaches of studies such as that of *McKinley et al.* (2011), which attempt to make judgements about multidecadal variability of the North Atlantic CO_2 sink based purely on pCO_2 observations. In their study, it was found that the oceanic trend in pCO_2 converges to that of the atmosphere when examined over the full 29 year period between 1981 and 2009, but when only decadal timescales are considered the two trends differ. Therefore, if on these same multidecadal timescales, the present day air-sea pCO_2 difference is maintained as *McKinley et al.* (2011) suggest, then the North Atlantic CO_2 sink is approximately stable; neither a decline nor an enhancement of the flux is apparent. Our work would support this approach, since we find the roles of k and α in governing flux variability over this timescale to be minor.

There is a broad increase in the critical timescale with latitude in the North Atlantic, which is explainable in terms of wind speed variability. At the low latitudes, wind speed variability is lower, increasing toward the poles (Figure 2.5). In addition, mean wind speeds are higher at the poles than the equator, so a given magnitude of wind speed variability at subpolar latitudes will produce greater variability in k than at the equator. This is because k scales with the square of the wind speed in our setup (*Nightingale et al.*, 2000). This zonal increase in k variability, in

addition to the presence of sea ice at the highest latitudes, is what causes the comparable zonal increase of the critical timescale (Figures 2.7 and 2.8). Furthermore, wind speed (and hence k) variability is a stronger control on carbon fluxes in the control simulation than the anthropogenic run. This is because the control's fixed atmospheric CO_2 concentration mean there is much less variability in ΔpCO_2 (and therefore also in the CO_2 flux) than in the anthropogenic run. As a result, wind speed variability patterns become relatively more important in setting the critical timescale for the control run than the anthropogenic (Figure 2.8). This means that k is a more important controller of variability of preindustrial carbon fluxes, although not more important than ΔpCO_2 on pentadal and longer timescales.

Through the comparison of modelled ocean fCO_2 fields against observations from SOCAT and Bermuda, it was shown that our setup underestimates variability on timescales shorter than 1 year. This result is to be expected, since GCMs of this scale will tend not to represent high frequency and small spatial-scale variability well (e.g. *Taylor et al.*, 2012). This could indicate that the ΔpCO_2 contribution may be a stronger control on fluxes on shorter timescales than our study suggests. Our forcing set underestimates multiannual wind speed variability at high latitudes, which may be associated with an inability to appropriately represent the NAO (an issue common to many GCMs (*Lee and Black*, 2013)). This could cause the real world critical timescale to be longer than what the model suggests. In the polar zone, the low bias does not affect the critical timescale, since k variability on all timescales is non-negligible. In the subpolar zone, the critical timescale may be underestimated, due to the low bias, yet the observation-derived critical timescales are comparable to the model prediction ($\sim$1-5 years for all three locations, using both model output and observations, Figure 2.8a).

Current ocean models (including NEMO-MEDUSA) do not derive k from the full range of kinetic factors that control it, and instead parameterize it purely from wind speed. It is likely then, that k variability on interannual and shorter timescales will be underestimated too; since real-world, shorter timescale variability in processes such as wave breaking and bubble dynamics etc. is not represented in GCMs. Until a more thorough understanding of the mechanisms underlying k is developed, we will not know exactly how important it is in governing short times-

cale flux variability. While the unmodeled factors are very likely strong controls on k on short timescales, it is not clear if their variability on longer timescales (decadal and longer) is large, relative to the effect of wind speed. If on these long timescales k variability is dominated by the contribution from wind speed, then wind speed parameterizations of k should be sufficient to estimate decadal gas transfer variability.

It is worth exploring the caveat that we have derived our findings from GCM output. One could expect that other models and configurations would yield slightly different timescales for the emergence of ΔpCO_2 dominance of flux variability. Yet our choice of model and setup appears reliable for the purposes of our study. This experiment has been shown to produce interannual flux variability comparable to other models as well as observational estimates (Table 2.1). In addition, it captures real world multiannual fCO_2 variance (Figures 2.3 and 2.4) and a reasonable degree of wind speed variability (Figure 2.5 and (*Lee and Black*, 2013)). Therefore, other models similarly capable of representing multiannual flux, fCO_2 and wind variability would likely give results consistent with those presented here, even if the mechanisms underlying that variability differ. Finally, the choice of gas transfer velocity parameterization can have some effect on the critical timescale derived. Functions (e.g. *McGillis et al.*, 2001) that produce a wider range of k values over the most commonly occurring wind speed range (3 to 15 m/s (*Wanninkhof*, 2014)) impart greater variability into the CO_2 flux, and so would increase the critical timescale. Many of the most commonly used parameterizations, however, show the greatest concordance of derived k values over the range of commonly occurring wind speeds, and so the critical timescale is generally insensitive to the choice of function (see Supporting Information).

While we have clearly identified the roles of each of the components of the flux equation in governing F variability, our methodology only hints at which underlying processes are important. To derive a more complete and mechanistic understanding of the controls on carbon flux variability, further work is necessary. A very broad range of physical, chemical and biological processes cause ocean pCO_2 variability, and so future work should seek to quantify the relative importance of these drivers, while attributing them to specific timescales of variability.

2.6 Conclusions

We have examined the relative importance of the three components of the air-sea CO_2 flux equation (k, ΔpCO_2 and α) in controlling flux variability on a range of timescales. In the North Atlantic, as for much of the global ocean, we find that sub-annual to interannual variability in ΔpCO_2 and k both have important roles in controlling the air-sea carbon flux, in agreement with previous work (e.g. (*Doney et al.*, 2009)). On these timescales, it is critical to obtain estimates of ΔpCO_2 and k for accurate flux variability to be derived. On pentadal and longer timescales, variability in k is not important, and can be ignored when estimating flux variability. The critical timescale increases from interannual at low latitudes to decadal at high latitudes.

Chapter 3

Controls on the Variability of DIC in the North Atlantic

3.1 Introduction

The carbon cycle is the system of exchanges of carbon within and between atmospheric, oceanic, terrestrial biospheric and lithospheric reservoirs. The distribution of the planet's carbon between these reservoirs and the processes occurring within them affects (and is affected by) the Earth's climate, forming a complex network of exchanges and feedbacks. Human activities over the latest three centuries have perturbed this system by rapidly releasing carbon from the lithosphere into the other three reservoirs, namely through the processes of fossil fuel combustion, cement production and land use change (*Ciais et al.*, 2013). Understanding the implications of the anthropogenic perturbation of the carbon cycle for Earth's climate is therefore a critical focus of current research. One of the main effects of humans' addition of carbon to the atmosphere from the lithosphere is to alter the radiative balance of the planet, which then has a range of interconnected knock-on effects on Earth's climate and carbon cycle. However, less than half of the anthropogenic carbon emitted to the atmosphere remains there; about a quarter of these emissions is absorbed by the oceans and 30% by the terrestrial biosphere (*Ciais et al.*, 2013; *Le Quéré et al.*, 2016). The importance of the oceans for the carbon cycle and the climate is well known, yet the details of its role are still to be understood. In particular, the variability of the size of the ocean carbon reservoir over interannual to multidecadal timescales is not well understood. This variability in oceanic

carbon concentrations is a leading-order control on the amount of CO_2 that the oceans absorb (*Doney et al.*, 2009; *McKinley et al.*, 2011; *Couldrey et al.*, 2016).

In the atmosphere, the main form of gaseous carbon is carbon dioxide (CO_2), whose proportion in air is often expressed as a partial pressure of the total gas mixture, pCO_2. A sample of seawater in contact with the atmosphere will, given time, reach an equilibrium or saturation concentration of Dissolved Inorganic Carbon (DIC) with respect to the atmospheric carbon concentration. The magnitude of this seawater saturation concentration is set by the temperature, salinity and alkalinity of seawater (and other dissolved species also play minor roles). The vast majority of DIC present in the global ocean results from the partial or complete equilibration of seawater with the carbon dioxide present in the preindustrial atmosphere. This means that to first order, a water parcel's DIC concentration is primarily set while it is in contact with the atmosphere in the mixed layer, based on atmospheric pCO_2, seawater temperature, salinity and alkalinity.

The timescale required for the mixed layer to equilibrate with atmospheric CO_2 levels is on the order of 0.5-1.5 years (*Broecker and Peng*, 1974; *Jones et al.*, 2014). This timescale is often longer than the flushing time of the mixed layer, and so water may leave the mixed layer before it has entirely equilibrated with atmospheric CO_2 concentrations. Furthermore, air-sea CO_2 disequilibria are also generated by physical, chemical and biological processes acting on faster timescales than the equilibration timescale of CO_2. Photosynthetic fixation of CO_2, respiration of organic matter, and mixed layer depth physical variability may all act to modify local DIC concentrations away from atmospheric equilibria, while the buffering effect of seawater carbonate chemistry slows equilibration relative to nonreactive gases (*Jones et al.*, 2014). Seawater DIC concentrations are further modified away from saturation concentrations once it departs the mixed layer into the ocean interior by two main processes: the soft-tissue pump and the carbonate (or hard-tissue) pump.

The soft tissue pump is a keystone biogeochemical process by which organic matter is moved from the upper ocean to the interior. In the top, sunlit hundred or so metres of ocean, phytoplanktonic primary producers draw inorganic carbon and nutrients that are dissolved in seawater into their bodies. When these organ-

isms die, some portion of their constituent organic matter on the order of 10-35% (*Buesseler and Boyd*, 2009; *Cavan et al.*, 2017) sinks into the deep ocean as particulates. Here, heterotrophs consume this sinking organic matter, and release CO_2 and nitrogenous waste back into solution. This whole process 'pumps' approximately 11 Pg C yr^{-1} out of the photic surface zone (*Sanders et al.*, 2014) and causes an enrichment of DIC at a depths greater than 300 m (*Gruber and Sarmiento*, 2002). Water that has been recently ventilated (such as North Atlantic Deep Water in the Atlantic) tends to show lower concentrations of DIC than older waters (such as those in the deep Pacific) because in the latter, the soft tissue pump has caused carbon to accumulate with water mass age (*Williams and Follows*, 2011).

In addition to the soft tissue pump, sinking particles can also enrich deep waters with carbon through the carbonate (or hard tissue) pump. In the photic surface ocean, calcifying plankton such as coccolithophorids produce calcium carbonate ($CaCO_3$) shells. When these shells sink into the deep ocean, they dissolve back into solution, adding carbon to the DIC pool. Much like with the soft tissue pump, the carbonate pump adds carbon to water masses over time, causing DIC enrichment in older waters. However, the carbonate pump tends to increase ocean DIC at greater depth than the soft tissue pump because the depths at which seawater is sufficiently corrosive to $CaCO_3$ are deeper than soft tissue remineralisation depths (*Williams and Follows*, 2011).

Recent decades of ocean carbon cycle research have yielded a useful understanding of the currently observed, large scale, time-mean ocean carbon reservoir, while highlighting important areas still in need of development (*Takahashi et al.*, 2014; *Key et al.*, 2015; *Bakker et al.*, 2016; *Olsen et al.*, 2016). The total oceanic inorganic carbon inventory is on the order of 38,000 Pg C (*Key et al.*, 2004, 2015; *Olsen et al.*, 2016). On the order of 90% of this inventory is accountable in terms of saturation with the preindustrial atmosphere (*Williams and Follows*, 2011). The DIC added to seawater at depth by the soft tissue pump contributes approximately 7% of the total budget (*Volk and Hoffert*, 1985). A few percent of the total DIC budget derives from the carbonate pump (*Williams and Follows*, 2011). The total amount of DIC that exists due to subduction of water masses with considerable disequilibrium carbon is not well defined. The final, anthropogenic component of ocean DIC

of 155±30 Pg C (*Ciais et al.*, 2013) represents approximately half a percent of the total. The current, instantaneous or mean state of the ocean carbon reservoir is therefore relatively better quantified (although still crucially incomplete) than its variability in time.

3.2 Methods

To explain variability of the ocean carbon sink through an era of large anthropogenic CO_2 emissions, a method of attributing DIC variability to underlying mechanisms is needed. To do so, the concepts of ocean carbon pumps (*Brewer*, 1978; *Ito and Follows*, 2005; *Williams and Follows*, 2011) are applied in a computer simulation of the ocean and carbon cycle. A numerical model is a useful tool to disentangle the complex interplay between biogeochemical processes and physical processes that control the ocean carbon sink. In a numerical model, it is possible to directly diagnose the roles of some of these processes, while the action of other mechanisms must be derived from model output. This section presents first a description of models used, then details of the configuration of simulations and finally the theoretical framework used to partition the ocean carbon sink in terms of contributions from biogeochemical processes.

3.2.1 Model and Simulations

The ocean physical model used is the Nucleus for European Modelling of the Ocean (NEMO v3.2) (*Madec*, 2008), coupled with Model of Ecosystem Dynamics, Utilisation, Sequestration and Acidification (MEDUSA)-2 biogeochemistry (*Yool et al.*, 2013a) and version 2 of the Louvain-la-Nueve Ice Model (LIM2, (*Timmermann et al.*, 2005)) sea ice model. Simulations were configured with the ORCA1 grid, featuring a nominal horizontal resolution of 1-by-1 degree of latitude (about 110 by 110 km) with 64 depth levels (*Madec and Imbard*, 1996). The horizontal grid scale is finer near the equator (reaching $1/3^{\text{rd}}$) to better represent equatorial processes such as upwelling. MEDUSA-2 is an intermediate complexity biogeochemical model that resolves nitrogen, silicon, iron, carbon, alkalinity and oxygen cycles. Further details about the models can be found in (*Couldrey et al.*, 2016) and the models'

respective publications.

The ocean model was forced with output from a simulation using the HadGEM2-ES model (*Collins et al.*, 2011). The HadGEM2-ES simulation models the time period 1860-2099 using prescribed greenhouse gas concentrations according to the IPCC's (Intergovernmental Panel on Climate Change) RCP8.5 forecast (*Jones et al.*, 2011). HadGEM2-ES features physical models of the ocean and atmosphere, the terrestrial and ocean carbon cycles, tropospheric chemistry and aerosols. The surface fluxes of heat, momentum and freshwater, and atmospheric chemistry from the HadGEM2-ES simulation were used to force NEMO at 6-hourly intervals. A 'control' forcing set was created by taking the first 30 years of this simulation (before changes in greenhouse gas concentrations impart significant climate change) and fixing greenhouse gas concentrations at a single preindustrial value. The ocean model was then forced with repeats of the forcing set such that the model could be spun up for a much greater length of time than the HadGEM2-ES output would otherwise permit.

The first phase of model spin-up entailed forcing the model with 20 repeated cycles of the 30 year forcing set, totalling 600 years. During this time, most of the drifts in the upper 1000m are eliminated, Figure 3.1a,b,c and Figure 3.2a,b,c. For some properties like oxygen, 600 years of spin-up is sufficient to clear most of the drifts even in the deep ocean, Figure 3.1d. For most tracers, however, drifts are still present in the deep ocean, and would require many more centuries (or millenia) to equilibrate, Figure 3.2d. Crucially, the drifts that remain after several hundred of years are relatively stable long term trends rather than unpredictable shocks, like those that occur within the first timesteps to 100 years of any simulation. Any remaining drifts can be easily accounted for in perturbed experiments by continuing the spin-up procedure as a control simulation, and then subtracting out the long term trend in the control from the perturbed experiment (see Section 4.4.5). Most importantly for this study, most surface fields show little to no drifts after 600 years of spin-up.

$$\frac{d\mathrm{Tr}^{pre}}{dt} = \frac{\mathrm{Tr}^{pre} - \mathrm{Tr}}{\tau} \tag{3.1}$$

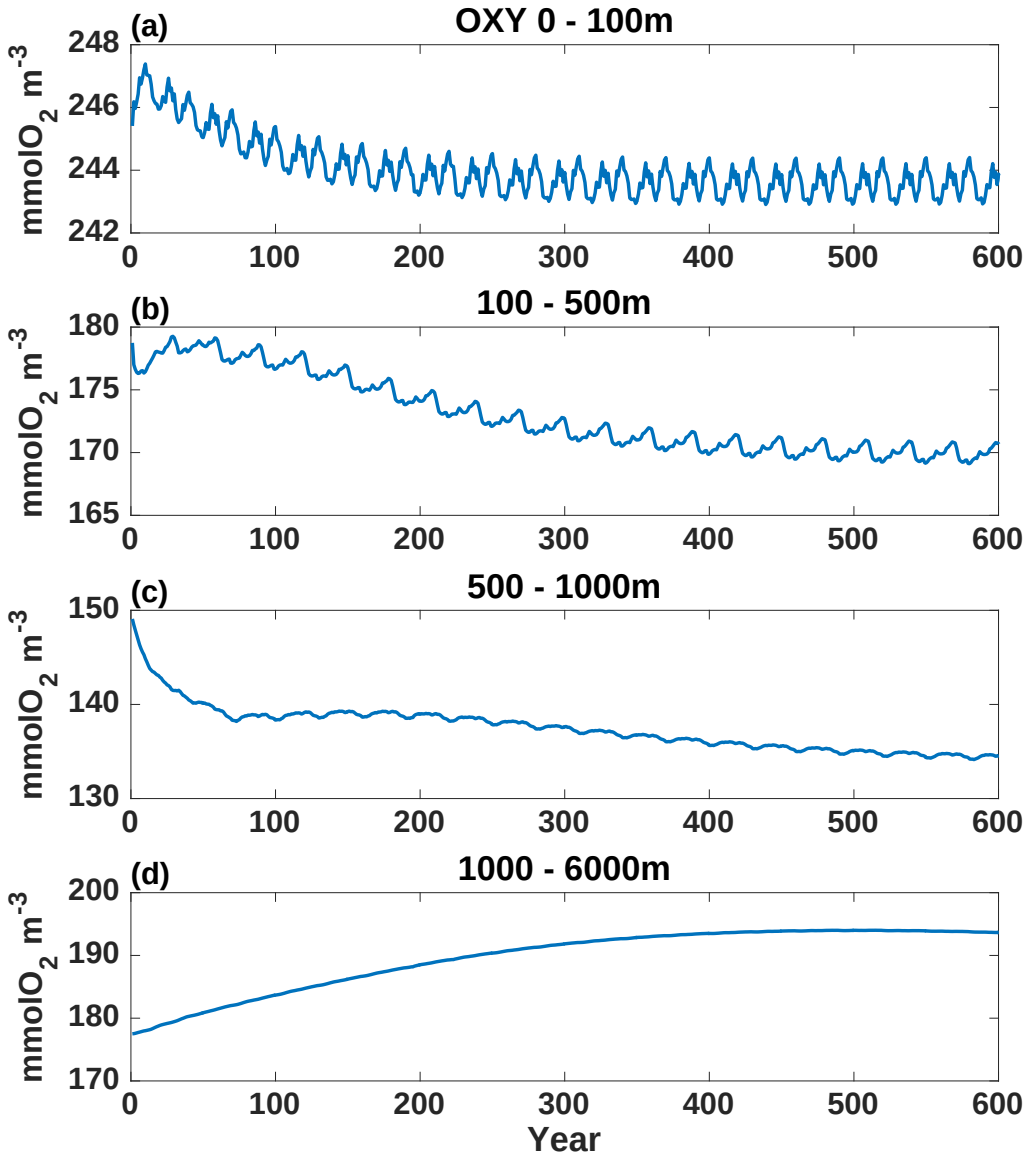

Figure 3.1: Time series of global mean oxygen concentration for four depth domains over the 600 year spin-up; 0-100m (a), 100-500m (b), 500-1000m (c) and 1000-6000m (d)

Further to the configuration of NEMO-MEDUSA-2 described earlier and elsewhere (*Yool et al.*, 2013a,b; *Couldrey et al.*, 2016), two preformed tracers were added; preformed alkalinity (A_T^{pre}) and preformed dissolved inorganic nitrogen (DIN^{pre}). An ideal preformed tracer's concentration (Tr^{pre}) in the mixed layer is equal to the concentration of the 'real' counterpart (Tr). The amount of any tracer regenerated (i.e. added to solution) at depth is therefore the difference between the total and preformed tracer concentrations. Away from the mixed layer, the pre-

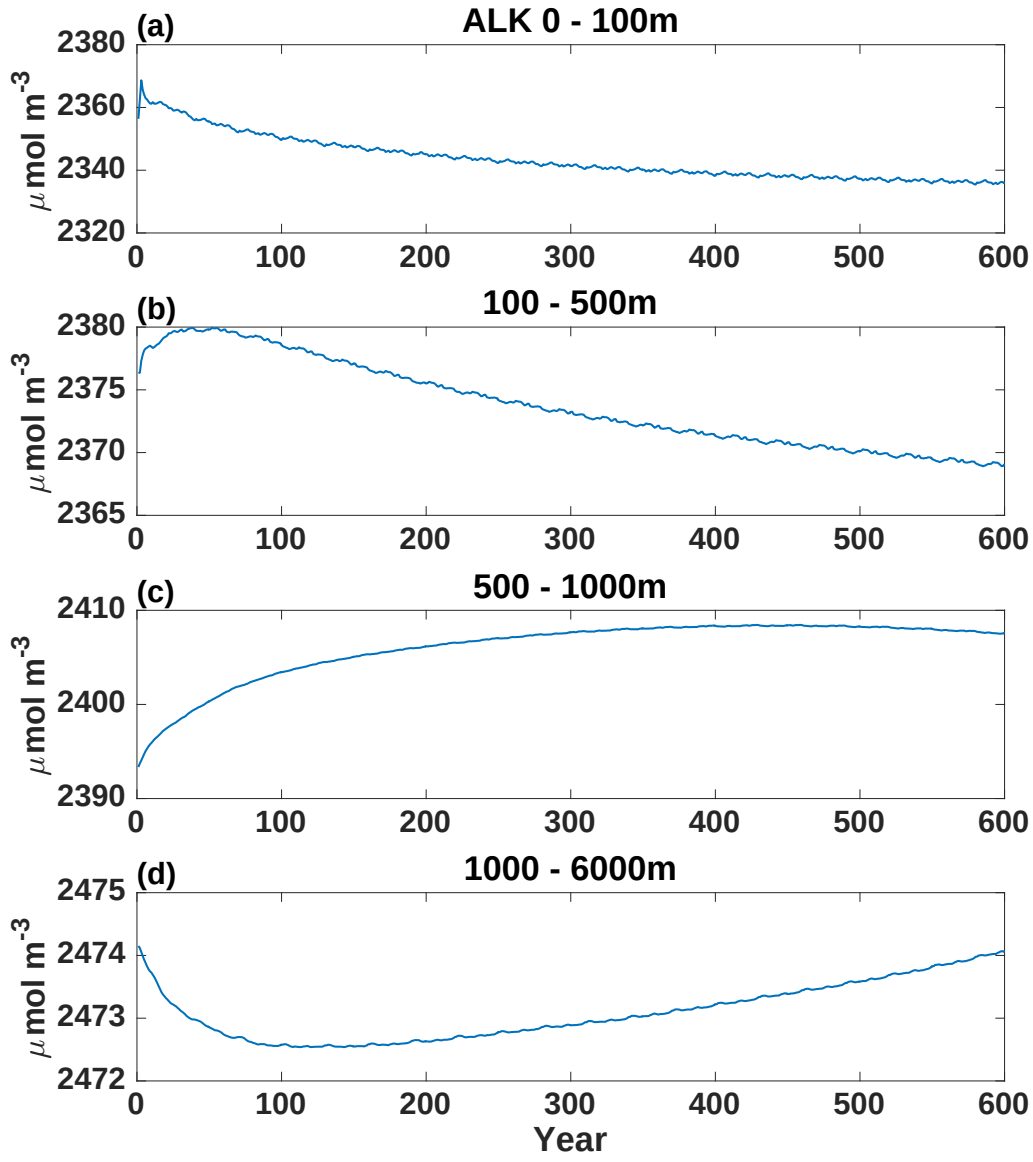

Figure 3.2: Time series of global mean alkalinity for four depth domains over the 600 year spin-up; 0-100m (a), 100-500m (b), 500-1000m (c) and 1000-6000m (d)

formed tracers are not subjected to any biogeochemical processes, and instead are only varied through physical redistribution. For the purposes of this work, these passive tracers are needed to understand the biogeochemical processes that happen deeper than the layer of primary productivity. Therefore, the surface ocean (where the preformed tracers' concentrations are set) is defined as the depth above which 95% of the global mean primary productivity occurs. At the end of 600 years of spin-up using 20 repeated cycles of the control forcing set, this depth is calculated as 62m. Above this depth, the preformed tracer concentration, Tr^{pre} is relaxed

toward the total tracer concentration, Tr, using equation (3.1). The relaxation timescale, τ, is set to 1 day, to quickly adjust the Tr^{pre} towards Tr.

$$A_{Tsurf} \approx S_{surf}m + c \tag{3.2}$$

$$A_T^{pre} = Sm + c \tag{3.3}$$

To initialise $\mathrm{A}_T^{pre}$and $\mathrm{DIN}^{\mathrm{pre}}$ in the model, fields of both tracers were estimated empirically using the model state at the end of 600 years of spin-up. If salinity is assumed to be conserved in the ocean interior, it possible to estimate A_T^{pre} in the deep ocean by linearly regressing surface alkalinity against salinity to find the coefficients m and c, equation (3.2). This generates a single regression that is applicable globally, since the entire global fields of surface salinity and alkalinity are used. The relationship found has an R^2 of 0.78 (a correlation r value of 0.8836), and a root-mean-square error (RMSE) of 28.419 μmol m^{-3}. Interior A_T^{pre} is found by multiplying interior salinity (S) by m and then adding c, equation (3.3). The A_T^{pre} field was generated using equation (3.3) on the model state after 600 years. The $\mathrm{DIN}^{\mathrm{pre}}$ initial field was generated by multiplying the model AOU field at the end of the 600 years by a Redfield ratio of nitrogen to oxygen ($\mathrm{R}_{NO} = -16/151$, (*Yool et al.*, 2013a)). The model was then run for a further 300 years (10 forcing cycles) with the preformed tracers included. It was not practical to run the model for the 1000s of years needed to reach physical or biogeochemical equilibria. However, drifts in the upper 2000m (where this study's variability of interest occurs) were judged to be sufficiently small after these 900 years of spin-up. After the spin-up period, three simulations were spawned, each 240 years long, spanning 1860-2099 (inclusive).

Table 3.1: Description of simulations' forcing

Experiment Name	**Radiative Forcing**	**Biogeochemical Forcing**
Anthropogenic (AN)	Yes	Yes
Warming Only (WO)	Yes	No
Control (CN)	No	No

The Anthropogenic run (AN) features prescribed rising concentrations of atmospheric CO_2 (and other greenhouse gases: methane, nitrous oxide and halocar-

bons) following RCP 8.5 (*Jones et al.*, 2011), which exceed 900 ppmv by the end of year 2099 (*Riahi et al.*, 2011). The Control (CN) simulation has its atmospheric CO_2 concentrations held fixed at a preindustrial level of 286 ppmv. The Control simulation was used to determine model drifts through the experiments. Another simulation was generated to distinguish the physical from the biogeochemical ocean carbon cycle response to rising atmospheric CO_2. This is achieved by decoupling the response of the biogeochemical model to changing atmospheric CO_2 levels, while still allowing greenhouse gases to perturb the physical model's radiation balance. In the Warming Only run, the model is subjected to the same radiative forcing of the Anthropogenic run, but atmospheric CO_2 is held constant at 286 ppmv. This allows for the ocean to physically adjust to anthropogenic climate change, without accumulating anthropogenic carbon. An estimate of the excess oceanic DIC due to anthropogenic carbon additions (C^{anth}) is found by subtracting the DIC field of the Anthropogenic run at a given time, t, (C_t^{AN}) from that of Warming Only run (C_t^{WO}), equation (3.4).

$$C_t^{anth} = C_t^{AN} - C_t^{WO} \tag{3.4}$$

3.2.2 Partitioning Reservoirs of DIC

One may express the DIC concentration of a water parcel, C, as the sum of preformed (C^{pre}) and regenerated (C^{reg}) carbon, equation (3.5). 'Preformed' carbon describes the dissolved inorganic carbon concentration that seawater had when it was last ventilated at the surface, and 'regenerated' carbon refers to the DIC that has been subsequently added into solution. If a water mass is in contact with the atmosphere (i.e. it is in the surface mixed layer) then its preformed and total tracer concentrations are the same, and the regenerated component is zero.

$$C = C^{pre} + C^{reg} \tag{3.5}$$

Preformed carbon can be partitioned into saturation (C^{sat}), disequilibrium (C^{dis}) and anthropogenic (C^{anth}) components, equation (3.6). C^{sat} is calculated with

standard carbonate system equations (*van Heuven et al.*, 2011a) (see also Chapter 1.7) and is a function of a water parcel's temperature, salinity, the mixing ratio of CO_2 in the preindustrial atmosphere ($X^{pre}_{CO_2}$=286 ppmv), and the alkalinity it had when last in contact with the surface (its preformed alkalinity, A_T^{pre}), equation (3.7). Note that the sea level pressure used to convert $X^{pre}_{CO_2}$ to pCO_2 is a uniform 100,000 Pa, since the ocean model does not respond to atmospheric pressure variability at sea level. C^{dis} refers to the excess or deficit of carbon that a water parcel may have if it is subducted away from the mixed layer without being saturated relative to the preindustrial atmosphere. The C^{dis} reservoir is distinct from the excess carbon content of seawater due to anthropogenic activities, C^{anth}. The calculation of C^{dis} is described at the end of this section and the derivation of C^{anth} is discussed earlier in Section 3.2.1.

$$C^{pre} = C^{sat} + C^{dis} + C^{anth} \tag{3.6}$$

$$C^{sat} = f(T, S, A_T^{pre}, X^{pre}_{CO_2}) \tag{3.7}$$

$$A_T = A_T^{pre} + A_T^{reg} \tag{3.8}$$

As with carbon, alkalinity (A_T) can also be expressed in terms of preformed (A_T^{pre}) and regenerated (A_T^{reg}) components, equation (3.8). Preformed alkalinity is set up as a passive tracer in the model, as described earlier in section 3.2.1. This passive tracer is required in ocean simulations experiencing transient climate change, since empirical approaches to estimating A_T^{pre} break down if the climate is not at steady state (*Williams and Follows*, 2011; *Bernardello et al.*, 2014).

$$C^{reg} = C^{csoft} + C^{carb} \tag{3.9}$$

$$DIN^{reg} = DIN - DIN^{pre} \tag{3.10}$$

$$C^{soft} = -R_{CN} DIN^{reg} \tag{3.11}$$

C^{reg} in equation (3.5) represents the contribution of the soft tissue pump (C^{soft}) and the carbonate pump (C^{carb}) to DIC, equation (3.9). Soft tissue carbon (C^{soft}) therefore describes the DIC that is added to seawater by organic matter respiration at depth. To diagnose C^{soft} a second preformed tracer is used: preformed Dissolved Inorganic Nitrogen (DIN) (DIN^{pre}). The biogeochemical model, MEDUSA-2, considers DIN as an aggregation of all inorganic nitrogen species, and does not separately represent nitrate, ammonium, nitrite etc. (*Yool et al.*, 2013a). This simplification means that biogeochemical calculations are performed using a bulk DIN pool, rather than accounting for differing behaviour of nitrogen species. If one assumes that carbon is regenerated at depth according to a fixed stoichiometry with the nitrogen regenerated at depth (DIN^{reg}), then preformed DIN may be used to estimate C^{soft} using equations (3.10) and (3.11). R_{CN} is the Redfield ratio of carbon to DIN, 106:16 in the model (*Yool et al.*, 2013a), after (*Anderson*, 1995), and DIN and DIN^{pre} are total and preformed DIN concentrations respectively. Since DIN^{pre} is relaxed toward 0 in the surface 62 m (see Section 3.2.1), C^{soft} is therefore also be relaxed toward 0 in the same domain.

The carbonate pump contribution (C^{carb}) is defined here as the DIC that has been added to seawater at depth as a result of the dissolution of $CaCO_3$. As with C^{soft}, the concentration of C^{carb} in the surface ocean (i.e. above 62 m) is by definition zero. For every mole of $CaCO_3$ dissolved, one mole of carbon is regenerated (added to the DIC pool as C^{carb}) alongside one mole of calcium ions, $[Ca^{2+}]$, equation (3.12). The addition of DIC to seawater in this way can be quantified from changes in seawater alkalinity away from preformed values. Since calcium ions are one of the components of alkalinity and are doubly charged, for each mole of calcium ions dissolved, there is a change in A_T (δA_T^{CaCO3}) relative to its preformed concentration by two moles, equation (3.13).

$$C^{carb} = \delta[Ca^{2+}] \tag{3.12}$$

$$\delta A_T^{CaCO3} = 2\delta[Ca^{2+}] = 2C^{carb} \tag{3.13}$$

Organic matter respiration also regenerates alkalinity at depth through the re-

lease of nitrate ions, $[NO_3^-]$, into seawater and must be accounted for, equation (3.14). The effect of the production of nitrate ions by respiration on alkalinity (δA_T^{NO3}) can be calculated by multiplying a fixed Redfield ratio of nitrate released to oxygen consumed (R_{NO} = -16/151) by the Apparent Oxygen Utilisation (AOU), equation (3.15).

$$\delta A_T^{NO3} = -\delta[NO_3^-] \tag{3.14}$$

$$\delta A_T^{NO3} = R_{NO}AOU \tag{3.15}$$

The total change of A_T from its preformed concentration is therefore the regenerated alkalinity and is the sum of the effects of both $CaCO_3$ dissolution and organic matter respiration, equation (3.16). By substituting equations (3.13) and (3.15) into equation (3.16), one arrives at an equation for A_T^{reg} in terms of C^{carb} and AOU. According to the decomposition of alkalinity in equation (3.8), A_T^{reg} is the difference between seawater A_T and A_T^{pre}, equation (3.18). By substituting (3.18) into (3.17) and rearranging, an equation for C^{carb} in terms of regenerated alkalinity and nitrogen is yielded, equation (3.19). However, in MEDUSA's simplified representation of alkalinity cycling, nitrate remineralisation does not affect A_T (the computational cost of this effect was considered to outweigh the gain in accuracy) and so this term does not feature in the final equation for C^{carb}, equation (3.20). Note that as with C^{soft}, the concentration of C^{carb} above 62 m is near zero because preformed alkalinity is relaxed toward the total alkalinity in the surface (see Section 3.2.1).

$$A_T^{reg} = \delta A_T^{CaCO3} - \delta A_T^{NO3} \tag{3.16}$$

$$A_T^{reg} = 2C^{carb} + R_{NO}AOU \tag{3.17}$$

$$A_T^{reg} = A_T - A_T^{pre} \tag{3.18}$$

$$C^{carb} = \frac{1}{2}(A_T - A_T^{pre} - R_{NO}AOU) \tag{3.19}$$

$$C^{carb} = \frac{1}{2}(A_T - A_T^{pre}) \tag{3.20}$$

By substituting equations (3.6) and (3.9) into equation (3.5), a complete decomposition of DIC can be written, equation (3.21). By subtracting the derived fields of C^{sat}, C^{soft}, C^{carb} and C^{anth} from modelled fields of C, an equation for disequilibrium carbon emerges, equation (3.22). In similar decompositions of DIC (*Williams and Follows*, 2011), preformed alkalinity must be estimated empirically, AOU is used to estimate some of the components, and C^{anth} cannot be easily quantified. The result is that when using an observation-based empirical DIC decomposition, it is not possible to distinguish C^{anth} and C^{dis}, nor the errors that accumulate using such approaches. By using explicitly simulated preformed tracers in numerical ocean models, it is possible to determine all the right hand side terms of equation (3.22) and solve for C^{dis}, and the major errors that arise from assumptions about empirical relationships are avoided.

$$C = C^{sat} + C^{soft} + C^{carb} + C^{dis} + C^{anth} \tag{3.21}$$

$$C^{dis} = C - (C^{sat} + C^{soft} + C^{carb} + C^{anth}) \tag{3.22}$$

3.3 Model Validation

In this section, modelled DIC and alkalinity fields are compared against observations in the GLODAP version 2 database (*Key et al.*, 2015; *Olsen et al.*, 2016). GLODAPv2 contains three dimensional ungridded values of biogeochemical parameters including DIC and alkalinity, as well accompanying physical water properties dating between 1972 and 2013. Since the ocean-only model is forced with output from an atmospheric model rather than observations, variability in the model will not be correlated with real world variability. In other words, at any grid cell for a single point in time, the modelled and observed monthly mean DIC, alkalinity etc. will differ, because the model experiences environmental variability that is not correlated with real world variability at that time. As such, it is more meaningful to compare the statistical properties of modelled variability, than to carry out a one-to-one comparison with observations. By extension, specific real world events such as the 1997-1998 El Niño or the phase of the North Atlantic

Oscillation will not match the model since such events are generated by internal variability rather than external forcing. However, the statistics about phenomena like ENSO are reasonably well captured in the model, although there are low biases in ENSO frequency and magnitude (see the end of section 1.9 for further details).

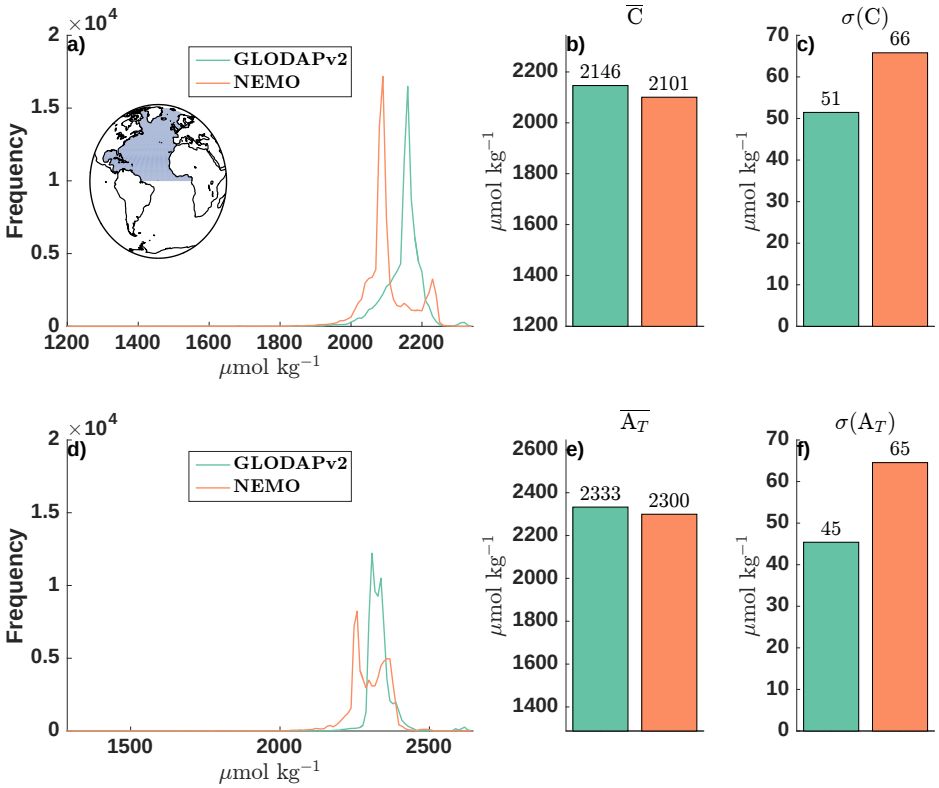

Figure 3.3: Frequency distributions of North Atlantic DIC (a) and alkalinity (d) in the GLODAPv2 database from all depths (green) with their corresponding values from colocated monthly mean model grid cells from the NEMO-MEDUSA Anthropogenic simulation (orange), where horizontal axes limits reflect the ranges of values. Time and space means of all DIC (b) and alkalinity (e) values. Standard deviations of all DIC (c) and alkalinity (f) values. Light blue area on inset map in (a) indicates this study's North Atlantic domain

To create a collection of model output comparable to the observations in GLODAPv2, the model grid cell values of DIC and alkalinity nearest to every GLODAP data point across all depths were identified. These two collections of modelled and observed DIC and alkalinity are then compared for their spatial and temporal variability by comparing the aggregrated frequency distributions of all values of DIC and alkalinity in 10 μmol kg^{-1} bins (Figure 3.3a and d). This demonstrates the extent to which the modelled fields of DIC and alkalinity show realistic spatial and temporal variance, in spite of the paucity of observations and differing histor-

ies of variability. By comparing model grid cells with unmapped observations, a more direct validation of the carbonate system is made than if an interpolated or mapped observation set were used. Since this work focuses on the North Atlantic, only datapoints from this basin are compared to model output; this domain is shown in the inset map of Figure 3.3a).

The modelled fields of DIC and alkalinity show broad agreement but with clear statistical differences from their data-based counterparts (Figure 3.3). Modelled DIC shows a low mean bias of 2101 μmol kg^{-1} versus the 2146 μmol kg^{-1} observed and, spatiotemporal variability is somewhat overestimated (66 μmol kg^{-1} versus the 51 μmol kg^{-1} observed). The most discrepant DIC values (the secondary mode with values above 2200 μmol kg^{-1} in Figure 3.3b) are associated with a high bias in the model below 3000 m. Modelled mean North Atlantic alkalinity shows a low bias (of 33 μmol kg^{-1}) and excessive spatiotemporal variability (standard deviation of 65 μmol kg^{-1} versus 45 μmol kg^{-1}).

3.4 Results

3.4.1 Total DIC Inventory

Before quantitatively attributing DIC variability to underlying causal mechanisms, the spectrum of the North Atlantic's full depth carbon inventory is shown. First, the North Atlantic's volume integrated inventory of DIC is calculated each year using annual mean fields (the North Atlantic domain is the same as in Figure 3.3a). The same is then done for the components of DIC: C^{sat}, C^{soft}, C^{carb}, C^{dis} and C^{anth}. Anomalies of these inventories (denoted with a prime, C') are calculated by subtracting out the long term (1860-2099) mean from each component. To first show the time variability of DIC and components, period spectra are calculated using standard Fast Fourier Transform techniques. It was not possible to satisfactorily detrend the series of C' and its components (by using a polynomial fit as one ideally would) before calculating spectra since their trends were not always well described by linear functions. Instead, more meaningful spectra are found when calculated from the time derivative (as a finite time difference) $\frac{\Delta C'}{\Delta t}$ (Figure 3.4a). Spectra are

smoothed with a 5-point moving average to aid visual comparison (Figure 3.4b).

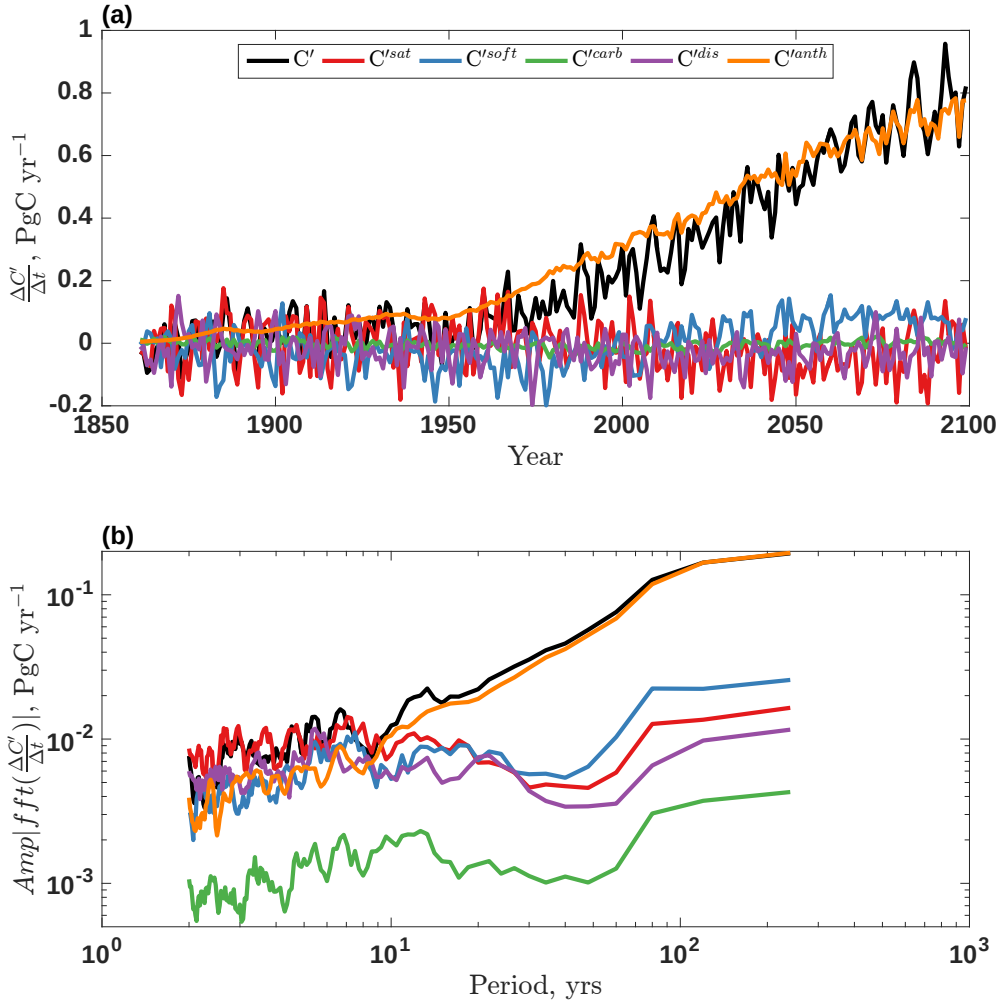

Figure 3.4: a) First time derivative of model total annual average North Atlantic carbon reservoir anomalies, black, with DIC component reservoirs, colour. b) Amplitudes of spectra of variability of the inputs shown in (a) against period in years. Note both logarithmic axes, and spectra are shown with short periods (high frequency) on the left, increasing to long periods (low frequency) on the right

Comparing the variability of the total carbon reservoir, C′, with its components in Figure 3.4 begins to suggest which mechanisms are reponsible for which variability. The long term accumulation of C′ closely matches that of C^{anth} (black and orange lines respectively in Figure 3.4a and b), especially for periods longer than 10 years. There is substantial variability in C′ on shorter timescales. The close alignment of the spectra for C′ and C^{sat} in the 1-10 year period band suggests that the C^{sat} component is important on these shorter timescales. Across all timescales, the spectrum for C^{carb} shows low amplitudes, suggesting this component is minor

in determining the variability of the North Atlantic carbon sink. The other two components, C^{soft} and C^{dis} show moderate to large amplitudes across a range of timescales. However, without an additional understanding of how component variability correlates with total DIC variability, it is not possible to discern the crucial detail of the interplay between components. This analysis reveals that North Atlantic DIC variability consists of different bands of timescales, each controlled by a different set of mechanisms.

Next, four distinct timescales of variability of the total North Atlantic DIC inventory (Figure 3.5) are isolated and examined. The long-term response of the North Atlantic carbon sink (or trend) is quantified by fitting a third order polynomial to annual mean DIC inventory anomalies (C') from a long term mean, equation (3.23), where $a_0, ..., a_3$ are polynomial constants and t is time (Figure 3.5e). This long term trend is subtracted from the C' time series to quantify variability on other timescales (3.24). Low frequency multidecadal variability (excluding the trend) is revealed by applying a low-pass 20 year running mean (f_{20}) to the detrended C' series, $C'^{Detrend}$, equation (3.25) (Figure 3.5d). The medium frequency decadal (5-20 year) variability is calculated by filtering the detrended series with a 5 year running mean (f_5), then subtracting the low frequency series, equation (3.26) (Figure 3.5c). Finally, the high frequency interannual (1-5 year) variability is the detrended series with the low and medium frequency components subtracted out, equation (3.27) (Figure 3.5b). Note that the seasonal cycle is not included in this analysis, since annually averaged model output is used. This same filtering analysis is applied to the time series of each of the components of the total DIC reservoir: saturation, soft tissue, carbonate, residual and anthropogenic. These four timescales of DIC variability were chosen because each is controlled by a different set of mechanisms.

$$C'^{Trend} = \sum_{i=0}^{3} a_i t^i \tag{3.23}$$

$$C'^{Detrend} = C' - C'^{Trend} \tag{3.24}$$

$$C'^{Low} = f_{20}(C'^{Detrend}) \tag{3.25}$$

$$C'^{Med} = f_5(C'^{Detrend}) - C'^{Low} \tag{3.26}$$

$$C'^{High} = C'^{Detrend} - C'^{Low} - C'^{Med} \tag{3.27}$$

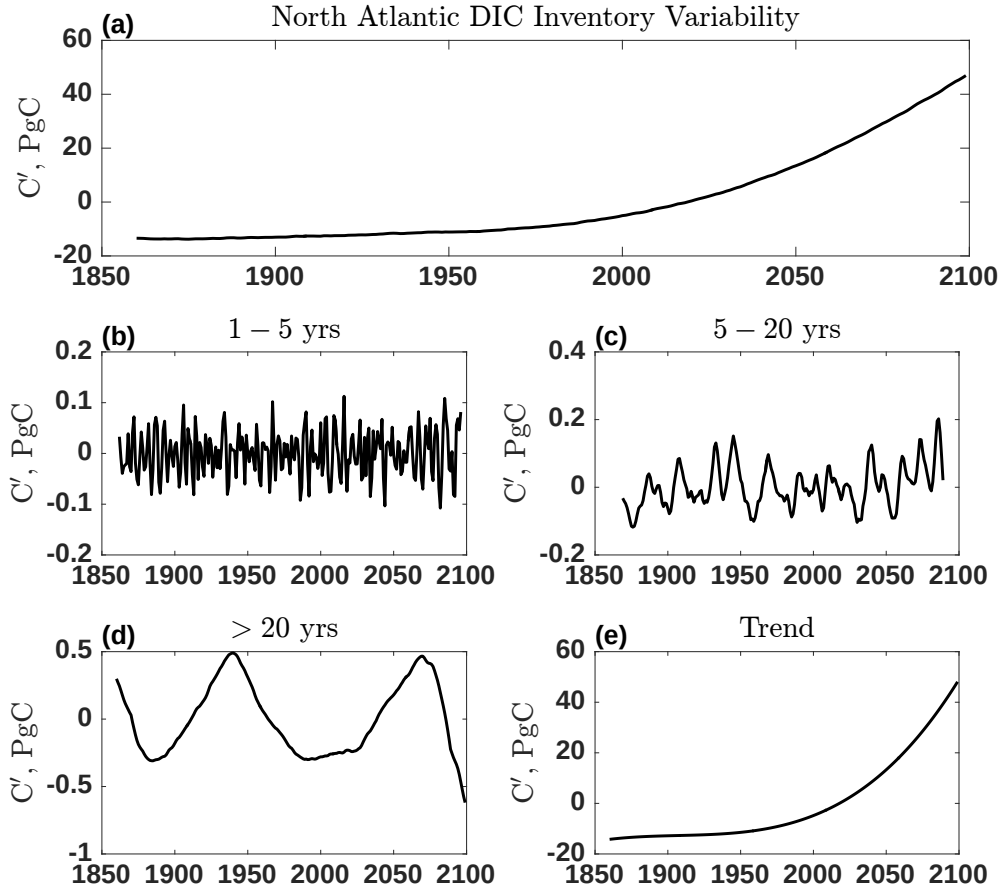

Figure 3.5: Variability of the North Atlantic Inventory of DIC annual anomalies from a long term annual mean (a), showing the interannual (b), decadal (c) and multidecadal (d) components, and the long term trend (e)

To asses the magnitude of variability on each timescale, the root-mean-square (RMS) is calculated for each of the filtered DIC components (Figure 3.6, a, d, g and j). This shows how large the anomalies in each DIC component are, with respect to the total DIC anomaly. However, for a component to be a strong control on the

total DIC variability, the anomalies in that component must be both large and well-correlated with DIC anomalies. For example, although decadal variability in C^{soft} is quite large (RMS = 0.07 PgC, Figure 3.6d), in comparison to C′ (RMS = 0.06 PgC), anomalies in C^{soft} are not correlated with C′ (correlation < 0.1, Figure 3.6e). Therefore, C^{soft} is not a strong control on North Atlantic decadal DIC variability. Equally, if component anomalies are well-correlated with C′, but small with respect to C′ (as in the case of C^{sat} for the long term trend, Figure 3.6j and k) then its overall impact on C′ is weak. A useful metric to quantify the control of a mechanism on DIC variability is the regression slope between filtered carbon anomalies (C′) and anomalies in each component (Figure 3.6c, f, i, l). This dimensionless number has values close to 1 if a component strongly controls C′, and close to 0 if the component is unimportant. Values for the slope of one component may be larger than 1 if at least one other component's slope is negative (i.e. compensatory). If the relationship between each component and the total DIC anomaly is perfectly linear then the sum of the slopes of all components is equal to one. However, in practice these relationships are not precisely linear, but nevertheless the sum of slopes is always close to 1 (0.89-1.14). By examining all three of these statistics (RMS of anomalies, correlations and regression slopes), one can attribute North Atlantic DIC inventory variability to its constituent components.

A comparison of the size of variability across the four different timescales as the RMS of anomalies (Figure 3.6a, d, g, j) shows that the magnitude of DIC inventory variability increases for longer timescales. In particular, interannual anomalies (Figure 3.6a) are much smaller (on the order 10^{-2} PgC) than longer timescale anomalies (order 10^{-1} to 10^{1} PgC, Figure 3.6g, j). While it would be tempting to dismiss these interannual anomalies as unimportant since they are small in comparison with the long term changes in basin carbon content by the year 2100, they are nonetheless crucial in setting the interannual variability of the ocean's uptake of CO_2, which in turn is an important component of climate variability (*McKinley et al.*, 2017).

Much of interannual North Atlantic DIC variability (regression slope of 0.78) is attributed primarily to the saturation component, C^{sat}. C^{anth} and C^{carb} are minor contributors on this timescale (0.10 and 0.05), and the roles of C^{soft} and C^{dis} are

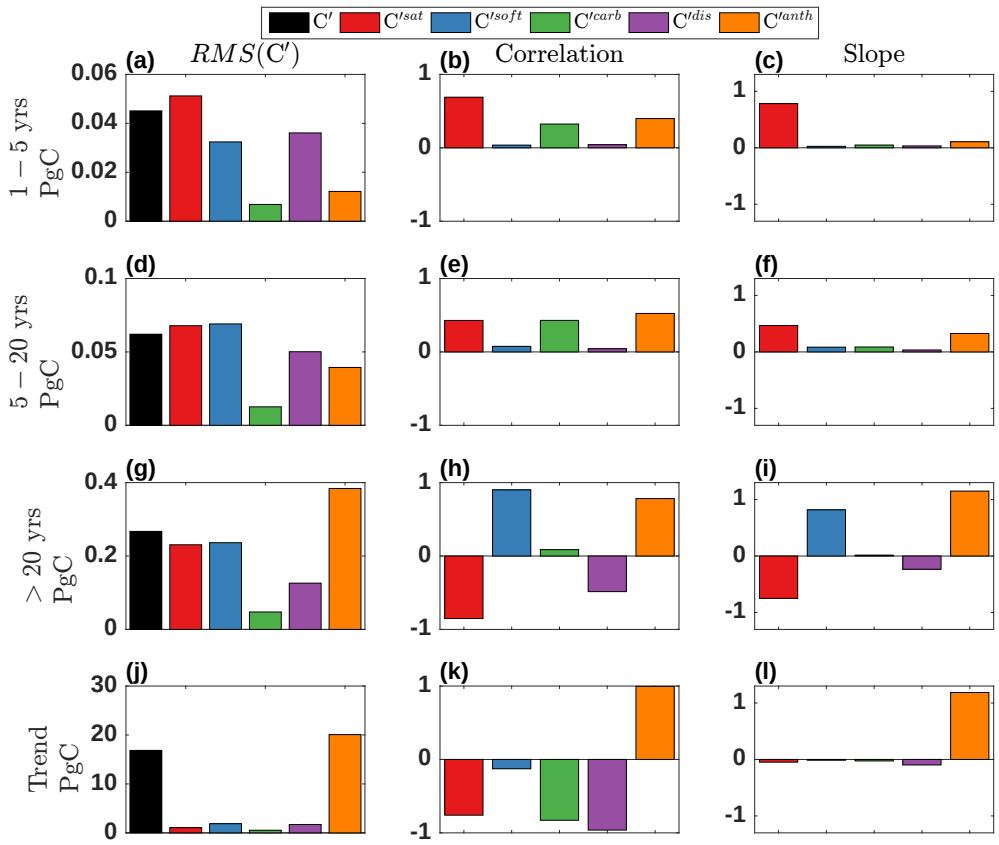

Figure 3.6: Statistics describing the relationship between DIC component variability and total DIC inventory variability on four timescales: interannual (1-5 year, a-c), decadal (5-20 year, d-f), multidecadal (>20 years, g-i), and the long term trend (j-l). Left: root-mean-square (RMS) of anomalies of total DIC inventory (black) and DIC components (colours). Centre: Correlations between component and total DIC inventory anomalies. Right: Slope of regression line between component and total DIC inventory anomalies

negligible (Figure 3.6c). Note that while a carbon anomaly in a given year may have large components from various periods of variability, this analysis identifies the portion of that anomaly that varies on specific timescales. For example, for a given time, a large part of the total carbon anomaly C′ may be due to a large anomaly in C^{soft}, but if that C^{soft} anomaly is part of long period variability, then this analysis will find C^{soft} to be unimportant on interannual timescales and instead identifies which component varies coherently on short, interannual timescales. On decadal timescales, most DIC variability is driven by the C^{sat} (0.46) and C^{anth} (0.32) components, each with similar importance (Figure 3.6f). Over multidecadal timescales, large variability in C^{sat} (-0.76) and C^{soft} (+0.81) is approximately compensatory, and variability in the accumulation of anthropogenic carbon (1.16) dominates the

variability of the North Atlantic carbon sink. The longest-term changes in the North Atlantic DIC inventory are driven almost entirely (1.18) by the basin's uptake of anthropogenic carbon (Figure 3.6l). On this timescale, although there are considerable changes in the inventories of each of the other components on the order of a few PgC, these are dwarfed by the basin's accumulation of approximately 70 Pg of anthropogenic carbon (Figure 3.5e).

3.4.2 C^{sat} Variability

The previous section has established that variability in saturation carbon is an important driver of the variability of total North Atlantic DIC, and so the following section seeks to account for this. Using the same variability analysis as for the total DIC inventory, the sources of variability in C^{sat} are quantified. For this analysis, only 3 timescales of variability are distinguished, since the controls on decadal and multidecadal C^{sat} variability are similar. To investigate the contribution of temperature, alkalinity and salinity to variability in C^{sat}, fields of C^{sat} are recalculated offline by fixing two fields while allowing the other to vary. For example, to quantify the C^{sat} variability caused by variability in ocean temperature, C^{sat}_{temp}, fields of C^{sat} are calculated using annual mean temperature fields for each year, but the alkalinity and salinity fields from the first year of the experiment, 1860. Note that this method of calculating saturation concentration by varying one parameter and fixing the others does not account for nonlinearities in carbon system equations. This means that at a given time, the sum of C^{sat} anomalies due to temperature, preformed alkalinity and salinity will not exactly match the C^{sat} anomaly when all three parameters vary together. Nevertheless, this method of decomposing C^{sat} variability is useful because the errors that result from carbonate system nonlinearities are smaller than the effects of interest.

Across all timescales, temperature and alkalinity are both important seawater properties that control C^{sat} variability, and the impact of salinity is negligible. On interannual timescales, large anomalies in C^{sat} due to temperature (regression slope of 0.60) and alkalinity (0.49) variability (Figure 3.7b) are well-correlated with the total C^{sat} variability (Figure 3.7c), and so both play roles in controlling interannual C^{sat} variability (Figure 3.7d). On decadal and multidecadal timescales, variability

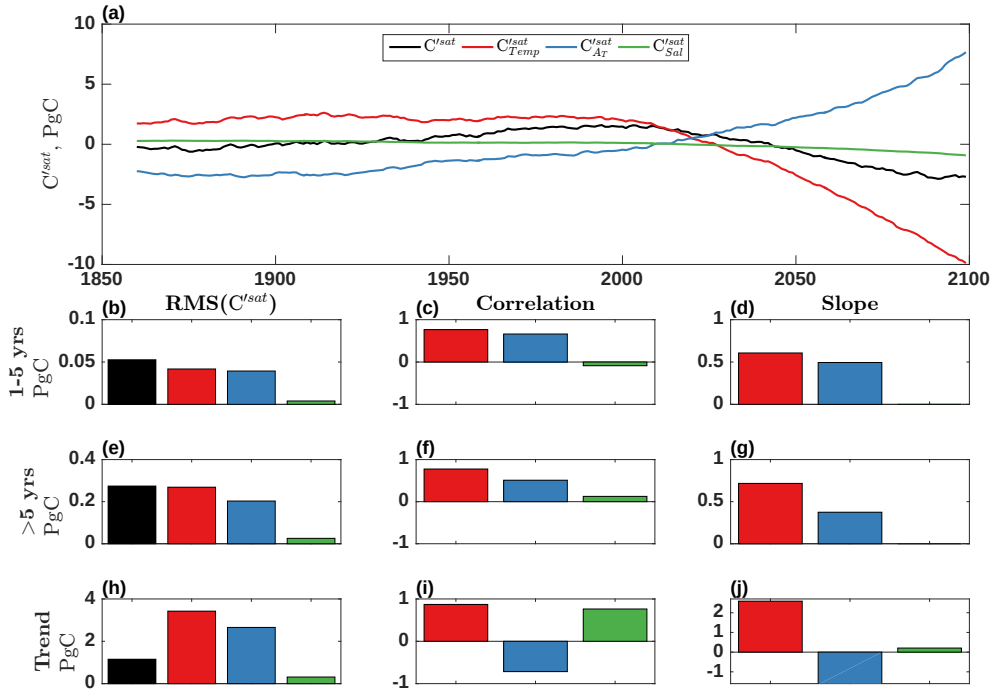

Figure 3.7: Time series of C'^{sat} with contributions from temperature, alkalinity and salinity (a), with descriptive statistics showing the roles of each contribution on different timescales, : interannual (1-5 years, b-d), decadal and multidecadal (>5 years, e-g), and the long term trend (h-j). Left: root-mean-square (RMS) of anomalies of C^{sat} inventory (black) and components (colours). Centre: Correlations between component and total C^{sat} inventory anomalies. Right: Slope of regression line between component and total C^{sat} inventory anomalies

in temperature imparts most of the variability in C^{sat} (0.71), but alkalinity variability is also important (0.37, Figure 3.7g). The trend in C^{sat} arises due to the partially compensatory long term changes in North Atlantic temperature and alkalinity (2.58 versus -1.65), which act in opposition to each other (Figure 3.7i and j). The effect of temperature, however, is larger, and gives rise to the long term decline of C^{sat} in the North Atlantic (Figure 3.7a). The only timescale over which salinity variability has an impact on C^{sat} is in the long term, causing a very small decrease by the end of 2099 (Figure 3.7j).

A 'back of the envelope' calculation demonstrates the carbonate system equations are slightly more sensitive to temperature variance than preformed alkalinity in the North Atlantic. In the North Atlantic, most of the C^{sat} variability occurs in the upper 300 m. A typical mean temperature for surface 300 m of the North

Atlantic is 16.22 °C, with a mean preformed alkalinity of 2388 mmol m^{-3}. Taken over the same domain, the RMS of interannual temperature anomalies is 0.0307 $°C$, and 0.2818 mmol m^{-3} for preformed alkalinity. A basin-scale temperature anomaly of 0.0307 $°C$ with properties that are otherwise typical of the upper 300 m in the causes a C^{sat} anomaly of 0.2805 mmol m^{-3}, all other factors being held constant. On the other hand, a preformed alkalinity anomaly of 0.2818 mmol m^{-3} will only change C^{sat} by 0.2284 mmol m^{-3}. Therefore, typical temperature variability in the North Atlantic imparts a greater effect on C^{sat} than typical preformed alkalinity variability does.

3.4.3 C^{soft} Variability

Soft tissue DIC variability is an important component of total DIC multidecadal variability. On a regional scale, this reservoir of carbon is modulated by only three process: export production, advection and destruction. Export production describes the process of generation of organic matter that is respired at depth by heterotrophs to form C^{soft}. Export production is therefore the source of C^{soft} in the global ocean. Once formed, C^{soft} may be exchanged between basins, and so advection can be a regional source or sink process. The global sink for C^{soft} arises when deep waters are upwelled into the surface mixed layer and its identity as C^{soft} is lost because in this framework, C^{soft} is assumed to be 0 in the surface ocean (i.e. C^{soft} is 'destroyed' as it is relaxed towards 0 above 62 m, see Section 3.2.1). Taken over the global scale, the advection term is zero, and the only two processes affecting the size of the C^{soft} reservoir are export production and destruction. To compare the roles of export production against physical redistribution and destruction in varying the soft tissue carbon concentrations on regional scales, the C^{soft} reservoir is partitioned into two components.

$$\frac{dC^{soft}}{dt} = E_t - (H_t + D_t) \tag{3.28}$$

$$(H_t + D_t) = \frac{dC_t^{soft}}{dt} - E_t \tag{3.29}$$

The total inventory change of soft tissue carbon in an ocean basin over time,

$\frac{dC^{soft}}{dt}$, can be expressed at any time, t, as the sum of the generation of C^{soft} by export production (E_t), the net horizontal advection of C^{soft} in or out of the basin (H_t) and the destruction of C^{soft} through ventilation (D_t), equation (3.28). Rearranging, it is possible to solve for $H_t + D_t$ using model output fields of E_t and $\frac{dC^{soft}}{dt}$, equation (3.29). Note that with this method it is not possible to distinguish between H and D, but their sum can be interpreted as the control of physical processes on C^{soft}.

$$C_t^{soft} = C_{t0}^{soft} + \sum_{t0}^{t} E + \sum_{t0}^{t} (H + D) \tag{3.30}$$

$$C_t^{\prime soft} = C_t^{soft} - C_{t0}^{soft} \tag{3.31}$$

$$C_t^{\prime soft} = \sum_{t0}^{t} E + \sum_{t0}^{t} (H + D) \tag{3.32}$$

To apply the same variability analysis on the C^{soft} budget, it is necessary to derive reservoirs of C^{soft} due to the two controlling processes, E and $H + D$. First, one may express the total amount of C^{soft} in a region at a given time, t, (C_t^{soft}) as the sum of C_{t0}^{soft}, the region's soft tissue carbon inventory at an initial time, $t0$ (the year 1860, model year 1), the amount of C^{soft} produced through export production since $t0$ and the amount of C^{soft} produced through advection and destruction since $t0$, equation (3.30). One can simplify equation (3.30) by subtracting out the initial C^{soft} inventory, C_{t0}^{soft}, to derive an equation for C^{soft} anomalies since the initial time ($C^{\prime soft}$), equations (3.31) and (3.32).

$$C_t^{\prime softE} = \sum_{t0}^{t} E + \overline{(H + D)^{CN}} \times (t - t0) \tag{3.33}$$

$$C_t^{\prime softH+D} = \sum_{t0}^{t} (H + D) + \overline{E^{CN}} \times (t - t0) \tag{3.34}$$

To quantify how one process (either E or $H + D$) changes the C^{soft} reservoir over time since $t0$, one may write down a similar equation where the other process is held constant. For example, the changes in C^{soft} in the anthropogenic (AN) simulation due to export production ($C^{\prime softE}$) can be expressed as the sum of the export

production since $t0$ plus the long term average of C^{soft} advection and destruction in the control (CN) simulation $\overline{(H+D)^{CN}}$ multiplied by the number of years since $t0$, equation (3.33). A similar equation for the changes in C^{soft} due to advection and destruction ($C'^{softH+D}$) in the anthropogenic simulation can be constructed in the same way, equation (3.34).

$$\overline{\frac{dC^{softCN}}{dt}} \neq 0 = L \tag{3.35}$$

At steady state, in a well spun-up control simulation, a long term average of $\frac{dC^{softCN}}{dt}$ should be zero. However the computational expense of running the model was large enough that it was not feasible to integrate the model for the thousands of years necessary to fully equilibrate all the fields. As a result, the ocean's C^{soft} pool in the control simulation (C^{softCN}) is still drifting throughout the experiments, equation (3.35). The long term average of this drift is calculated over the entire 240 years of the control simulation as L (in $PgC^{soft}yr^{-1}$), equation (3.35).

$$C_t'^{softL} = L \times (t - t0) \tag{3.36}$$

To close the budget such that the total $C_t'^{soft}$ is equal to the sum of the components from export production and advection plus destruction, a third 'leak correction' term must be included, $C_t'^{softL}$. The leak correction at any time, t, is calculated as the long term average drift in the control simulation C^{soft} inventory multiplied by the number of years since $t0$, equation (3.36).

$$C_t'^{soft} = C_t'^{softE} + C_t'^{softH+D} - C_t'^{softL} \tag{3.37}$$

The leak correction arises because the long term average production of C^{soft} in the control simulation is not equal to its advection + destruction. As a result, the sum of $C_t'^{softE}$ and $C_t'^{softHD}$ drifts away from $C_t'^{soft}$ at a rate of the drift in the control simulation, L. This term is qualitatively unimportant on all timescales

except the long term trend since its rate of accumulation is time invariant. The full C^{soft} decomposition in terms of contributions from changes in export production, advection + destruction, and drift is therefore found, equation (3.37). Note that the leak correction term is subtracted in this budget because by definition its sign must oppose the control simulation drift, L, equation (3.35). Therefore, if the control simulation has a negative C^{soft} drift (i.e. loses C^{soft} over time), then C'^{softL} increases over time to compensate.

With the decomposition of C^{soft} equation (3.37), one may quantitatively attribute variability in the total pool to anomalies in either export production or physical processes. Time series of the three components in equation (3.37) can then be analysed using the same methods described earlier: subtracting long term means, filtering and calculating descriptive statistics.

Earlier it was shown that C^{soft} variability becomes important in setting the overall North Atlantic DIC variability over multidecadal timescales (Figure 3.6i). Over interannual timescales, C^{soft} variability in the North Atlantic is driven primarily by variability in advection and destruction (Figure 3.8d). $H+D$ variability is partially opposed by variability in export production on decadal and longer timescales, but the magnitude of the latter is much smaller (Figure 3.8g and j). The contribution of model drift to the overall changes in C^{soft} by the end of the simulation in 2099 is small in comparison with the other two components (Figure 3.8j).

Typical anomalies in the export production are not large enough to generate the C^{soft} anomalies produced in this simulation. In the North Atlantic, the RMS of basin-integrated interannual C^{soft} anomalies is 0.032 PgC, Figure 3.8b. North Atlantic export production anomalies on interannual timescales have an RMS of 0.0186 PgC yr^{-1}. On longer timescales, the case is qualitatively the same: export production variability is insufficient to explain the modelled C^{soft} inventory variability. The the other physical processes controlling (advection of C^{soft} into the basin and destruction of C^{soft} by ventilation) therefore must also have an important stake in setting the basin's inventory variability.

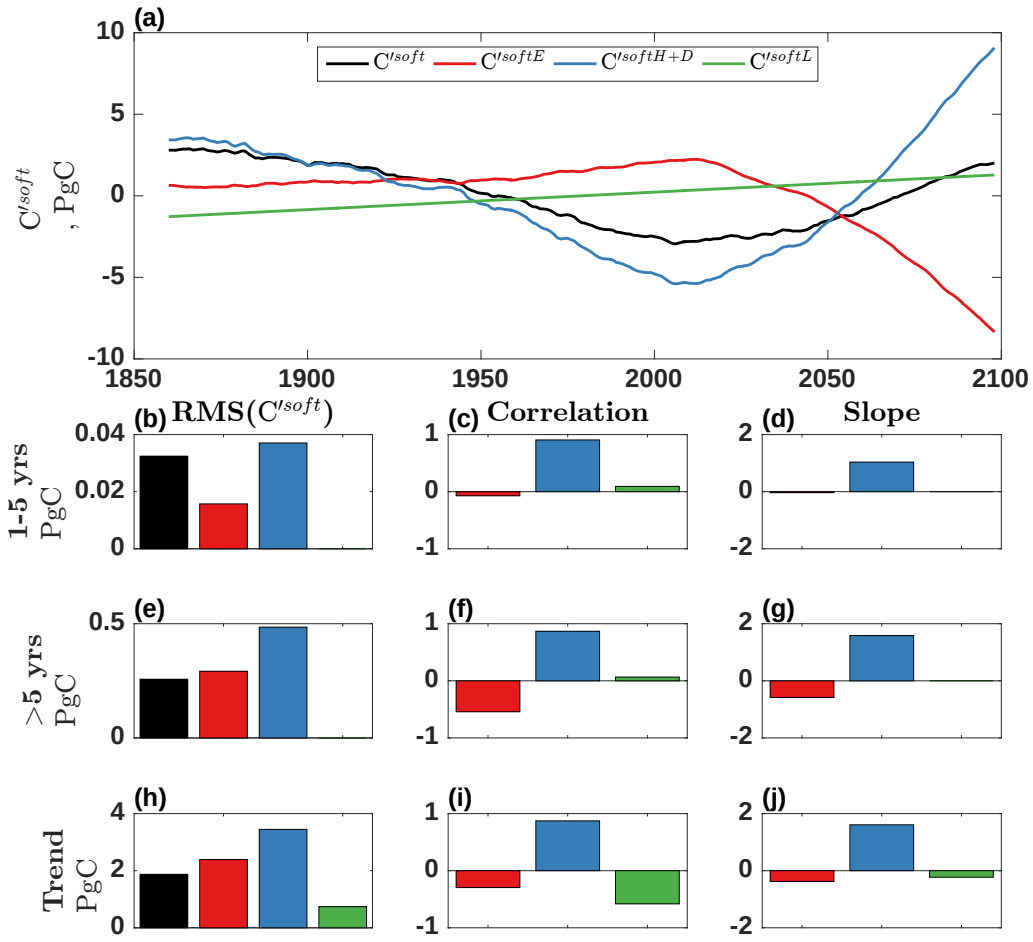

Figure 3.8: Time series of C'^{soft} with contributions from export production (E), and advection plus destruction ($H + D$) (a), with descriptive statistics showing the roles of each contribution on different timescales, : interannual (1-5 years, b-d), decadal and multidecadal (>5 years, e-g), and the long term trend (h-j). Left: root-mean-square (RMS) of anomalies of C^{soft} inventory (black) and components (colours). Centre: Correlations between component and total C^{soft} inventory anomalies. Right: Slope of regression line between component and total C^{soft} inventory anomalies

3.5 Discussion

In this work, it has been shown that different mechanisms give rise to variability in the size of the North Atlantic carbon sink over a range of timescales from the onset of industrial era through to the end of the current century. In general, variability primarily in temperature but also in preformed alkalinity of the North Atlantic governs the interannual variations in basin DIC content. This result suggests that

relatively high frequency variations in ocean heat content are critical in driving short term changes in the carbon reservoir, which are likely to govern short term CO_2 flux variability (*Halloran et al.*, 2015). *Doney et al.* (2009) describe how the physical redistribution of DIC in the upper 100m is the main process giving rise to interannual variability in surface ocean pCO_2 and therefore air-sea carbon fluxes in the North Atlantic. Advection and diffusion of heat and alkalinity could therefore be the main processes that give rise to the C^{sat} variability presented here. However, further work would be necessary to exhaustively identify the roles of other mechanisms that vary temperature and preformed alkalinity (such as surface heat and freshwater fluxes, biological modulation of surface alkalinity etc.).

Interannual DIC variations are small in size in comparison with the longer-period variability of North Atlantic carbon content. The accumulation of anthropogenic carbon on decadal, decadal and multidecadal timescales becomes increasingly important in setting the basin's DIC content. Even so, saturation carbon variability remains an important driver of total DIC variability across decadal to multidecadal timescales. On multidecadal timescales, fluctuations in the basin's soft tissue carbon reservoir also become critical. These soft tissue reservoir variations are almost completely counteracted by variations in the basin's saturation carbon content of opposing sign, with the net effect on total DIC being primarily driven by anthropogenic carbon accumulation. Again, this saturation carbon variability is mostly controlled by North Atlantic heat content, with preformed alkalinity playing a secondary role. The C^{soft} changes are mainly caused by physical accumulation of soft tissue carbon driven by circulation and/or ventilation changes rather than increasing biological export. In both reservoirs, these findings suggest primacy of physical rather than biological controls on North Atlantic DIC variability. *Bernardello et al.* (2014) describe how the natural carbon cycle response at the end of the 21st Century is characterised by large, nearly compensating decreases in preformed carbon (due to decreased C^{sat}) and increases in C^{soft}. The work presented here identifies the same long-term DIC response (the trends in C^{sat} and C^{soft}, Figure 3.6l), but also that counteracting C^{sat} and C^{soft} variability is a critical control on North Atlantic DIC on shorter, multidecadal timescales as well (Figure 3.6i).

Large multidecadal North Atlantic DIC variability arises in connection with the

basin's circulation. Export production is affected by ocean circulation by varying the supply of nutrients to the photic zone, which modulates primary productivity. However, this work suggests that action of North Atlantic circulation variability on the redistribution and destruction of soft tissue carbon is greater (and of opposing sign) than the effect on export production. The result is that net multidecadal variability in the soft tissue carbon reservoir is controlled by the larger effect of those physical processes than the biological DIC source. Indeed, redistribution of C^{soft} has been suggested as the main driver of observed multidecadal DIC accumulation in the Northeast subpolar Atlantic (*Humphreys et al.*, 2016). Furthermore, the upper (0-1000m) ocean overturning has been highlighted recently for its major role in in controlling decadal CO_2 flux variability by modulating the supply of remineralised DIC (*DeVries et al.*, 2017). Future work should aim to distinguish the roles of advection and destruction, and to identify the roles of different advective pathways in and out of the North Atlantic.

The North Atlantic anthropogenic carbon content shows large multidecadal swings in phase with the total DIC. The AMOC is a likely candidate responsible for these multidecadal swings, although further work is necessary to explicitly link the mechanisms. One potential mechanism could be that stronger overturning rapidly removes DIC (and C^{anth}) from the basin (southward across the equator). During weaker phases the opposite occurs and C^{anth} (which invades the ocean from the surface) has more time to accumulate in the basin before being advected out. A dedicated study investigating C^{anth} transport across the edges of the North Atlantic domain to large scale circulation would be necessary to determine if this speculated mechanism is robust.

3.6 Conclusions

Variability in the North Atlantic carbon sink across interannual, decadal, multidecadal and centennial timescales was attributed to contributions from driver processes. Interannual anomalies of DIC in the North Atlantic are mainly driven by temperature and alkalinity variations to the saturation concentration. Most of basin's decadal variability is set by saturation variability, and anthropogenic

carbon plays an important secondary role. On multidecadal timescales, swings in large scale North Atlantic circulation drive strong compensating effects on DIC: decreasing saturation and increasing soft tissue carbon variability mostly cancel each other, and the anthropogenic increase drives the net effect. The long term trend is entirely characterised by the North Atlantic's accumulation of about 70 PgC, which dominates the comparatively minor changes of a couple of PgC in the natural pools by the end of the 21st Century.

Chapter 4

A Dissection of Global DIC Variability

4.1 Introduction

In the previous chapter, the drivers of variability of the North Atlantic's total DIC inventory were explored in detail. That work identified that much of the interannual DIC inventory variability was controlled by modulation of the carbon saturation concentration, C^{sat}. Of the four input parameters to the saturation calculation (temperature, salinity, preformed alkalinity and the preindustrial atmospheric CO_2 mixing ratio), the biggest driver of variability was found to be temperature, with preformed alkalinity playing a secondary role. This result is intriguing because it implies that one can quantify much of the year-to-year variability of the North Atlantic carbon stock using readily available observations of water temperature and salinity. A salient question that follows this finding is "to what extent is C^{sat} the main driver of global interannual DIC variability; what processes control DIC variability in the other ocean basins?"

Previous work identifies strong interannual CO_2 flux variability in the tropical Pacific, subpolar and temperate North Atlantic and Pacific and the Southern Ocean (*McKinley et al.*, 2017). In the Pacific, interannual variability in the tropics associated with ENSO varies the supply of DIC to the surface, which affects surface pCO_2 and driving large swings in the air-sea CO_2 flux (*Doney et al.*, 2009; *Park et al.*, 2010; *Rödenbeck et al.*, 2014; *Wang et al.*, 2015; *Landschützer et al.*, 2016). Contrastingly in the Atlantic, there are indications that thermal effects on pCO_2

as well as DIC reorganisations play a large role in modifying year-to-year flux variability (*Thomas et al.*, 2008; *Doney et al.*, 2009; *Wang et al.*, 2015; *Landschützer et al.*, 2016). In the Southern Ocean, flux variability is linked to atmospheric forcing of ocean circulation that varies the supply of DIC and alkalinity to the surface (*Landschützer et al.*, 2015, 2016). In all cases, those studies point towards the key role of DIC in controlling interannual the global CO_2 flux.

Looking to variability on longer decadal and multidecadal timescales, the accumulation of anthropogenic carbon appears to become important (*Wanninkhof et al.*, 2010; *McKinley et al.*, 2016). However, it is presently difficult to precisely distinguish anthropogenic carbon uptake from the large decadal variability in the natural carbon cycle (*Landschützer et al.*, 2016; *McKinley et al.*, 2016). For instance, in the Northeast Atlantic where C^{anth} accumulation is relatively rapid, changes in remineralised carbon dominate the multidecadal DIC increase (*Humphreys et al.*, 2016). Other work investigates the long term climate adjustment to anthropogenic climate change by the year 2100 CE, identifying widespread accumulation of C^{anth} and reductions in preformed carbon that are partly compensated by an accumulation of remineralised organic carbon (*Yool et al.*, 2013b; *Bernardello et al.*, 2014).

While other work has revealed that variability in the global inventory of DIC is a key driver of CO_2 flux variability over a wide range of timescales, questions still remain about what underlies this DIC variability. Some studies examine the contributions of component processes of global DIC fields in a time-mean sense (*Williams and Follows*, 2011; *MacGilchrist et al.*, 2014), or focus on the long term climate changes on centennial (*Bernardello et al.*, 2014) or much longer timescales (*Ödalen et al.*, 2017). The contributions of each DIC component to variability on interannual to multidecadal timescales has yet to be discussed from a global perspective.

This chapter is organised as follows: a brief overview of the model and simulations are presented. Then, a method to estimate the contributions of saturation, the soft tissue pump and the carbonate pump to DIC from commonly measured oceanographic parameters following standard published procedures is described. This method is then used to estimate each DIC component at various repeatedly

surveyed locations in the global ocean. The same method is also used on model output in the same locations. The observed and modelled temporal variability of each DIC component are compared to establish model performance, focusing on the surface 2000 dbar. Using model diagnostics (preformed tracers of alkalinity and nutrient) that provide more robust estimates of DIC components, global drivers of DIC variability for the full water column are then identified.

4.2 Methods

4.2.1 Model and Simulations

Output from a ocean general circulation model coupled to an intermediate complexity ecosystem model was used to identify the drivers of variability in the DIC inventory. The simulations used in this analysis are the same as those described in Section 3.2.1, but are briefly summarised again here, Table 4.1. The model consists of NEMO v3.2 ocean physics (*Madec*, 2008), coupled with MEDUSA-2 biogeochemistry (*Yool et al.*, 2013a) and version 2 of the Louvain-la-Nueve Ice Model (LIM2, (*Timmermann et al.*, 2005)) sea ice model. Simulations were run for the global domain at a nominal horizontal resolution of 1-by-1° of latitude.

The model was forced with surface fluxes of heat, momentum and freshwater, and atmospheric chemistry from a different coupled Earth System Model, HadGEM2.0-ES (*Collins et al.*, 2011). The HadGEM2.0-ES simulation was itself forced with emissions of greenhouse gases according to RCP8.5 (*Jones et al.*, 2011) from the year 1860 CE to the end of 2099 CE. A 'control' forcing set was created by taking the first 30 years of this experiment (while anthropogenic greenhouse gas concentrations are too small to cause significant climate change) and fixing greenhouse gas concentrations at a single preindustrial value of 286 ppmv. The ocean model was then spun up by 20 repeated iterations of the control forcing set for a total of 600 years. After this time, preformed tracers of Dissolved Inorganic Nitrogen (DIN) and alkalinity were set up, and the model was spun up for a further 300 years, as detailed in Section 3.2.1.

An 'Anthropogenic' experiment simulation (AN) was performed on the model

Table 4.1: Description of simulations' forcing

Experiment Name	**Radiative Forcing**	**Biogeochemical Forcing**
Anthropogenic (AN)	Yes	Yes
Warming Only (WO)	Yes	No
Control (CN)	No	No

state after the 900 years of spin-up by forcing the NEMO-MEDUSA with output from the HadGEM2.0-ES RCP8.5 simulation; a duration of 240 years from 1860-2099. In addition, a 'Warming Only' simulation (WO) was performed covering the same period, except the radiative forcing effect of rising atmospheric greenhouse gases was decoupled from the ocean biogeochemical effects. The result is that the ocean responds to a warming climate without accumulating additional DIC, and the excess DIC in the anthropogenic run relative to the control can be considered 'anthropogenic carbon', C^{anth}. Finally, a 'Control' simulation (CN) was performed by continually forcing NEMO-MEDUSA repeatedly with the 30 year forcing set for the same duration as the perturbed experiments (AN and WO, 240 years), with atmospheric greenhouse gas concentrations fixed at preindustrial levels. The Control simulation is used to remove model drift from long term trends in the Anthropogenic simulation. Further details about the setup of these experiments is included in Section 3.2.1.

4.2.2 Partitioning Reservoirs of DIC

In Chapter 3.2.2, a method to quantify DIC components in a model framework was discussed, which hinged on the use of prognostic preformed tracers. These tracers are useful to directly diagnose the five compontents of DIC in the model, but the same approach cannot be used in the real world because preformed alkalinity and nutrient cannot be directly quantified. In the real world, methods exist to perform a similar DIC decomposition by estimating preformed tracers empirically using commonly observed oceanographic parameters (*Brewer*, 1978; *Ito and Follows*, 2005; *Williams and Follows*, 2011). For the purposes of the model validation only, this 'empirical decomposition' is used because it can be applied to both observations and model output, allowing the two to be compared like for like. While the empirical method is useful, other work has highlighted how estimating preformed

nutrients using apparent oxygen utilisation can lead to errors due to the subduction of significant air-sea oxygen disequilibria (*Ito et al.*, 2004; *Bernardello et al.*, 2014). The use of preformed tracers therefore avoids this source of error since preformed tracers are modelled directly. The main analysis using model output described in this chapter (Section 4.4) employs the 'model decomposition' (see Section 3.2.2). The model decomposition is used for the main analysis because it provides three advantages over the empirical method: 1) errors arising from the empirical estimation of A_T^{pre} and preformed nutrient are avoided 2) the model decomposition is robust through transient climate change and 3) the model decomposition allows C^{anth} and C^{dis} to be distinguished (see description of C^{res} later in this section).

The first derived parameter needed is preformed alkalinity, A_T^{pre}: the alkalinity that a water parcel had when it lost communication with the surface (mixed layer). By assuming that both this property and salinity mix conservatively in the interior ocean, this can be approximated from surface salinity. Using the same method as described in Section 3.2.1, surface alkalinity may be linearly regressed onto salinity. Those regression coefficients may then be used on interior ocean salinity to estimate A_T^{pre}, equation (3.3). Using fields of temperature, salinity, A_T^{pre} and the mixing ratio of CO_2 in the preindustrial atmosphere ($X_{CO_2}^{pre}$=286 ppmv) C^{sat} is calculated using standard carbonate system equations (*van Heuven et al.*, 2011a).

$$C^{soft} = -R_{CO}AOU \tag{4.1}$$

Next, the DIC regenerated by heterotrophs can be calculated from oxygen concentrations by assuming that carbon is remineralised at a fixed ratio to the oxygen consumed by heterotrophs, $R_{CO} = -106/151$, (*Yool et al.*, 2013a). Thus, from AOU C^{soft} may be calculated (4.1).

$$C^{carb} = \frac{1}{2}(A_T - A_T^{pre} - R_{NO}AOU) \tag{4.2}$$

At depth, two main processes modify alkalinity: the dissolution of calcium carbonate and the remineralisation of nitrate, as discussed earlier in Section 3.2.2 (where the full derivation of C^{carb} can be found). By assuming that nitrate is

remineralised with a fixed ratio to oxygen, $R_{NO} = -16/151$ (*Yool et al.*, 2013a), the alkalinity change at depth due to nitrate remineralisation can be calculated by multiplying R_{NO} by AOU, equation (3.15). The dissolution of one mole of calcium carbonate adds one mole of DIC into solution with one mole of doubly charged calcium ions, equation (3.13). Therefore, the DIC regenerated due to the carbonate pump is determined from regenerated alkalinity and regenerated nitrate, equations (3.19) and (4.2).

$$C^{res} = C - (C^{sat} + C^{soft} + C^{carb}) \tag{4.3}$$

The final component, C^{res}, is found as the residual when C^{sat}, C^{soft} and C^{carb} are subtracted from the total DIC concentration, C, equation (4.3). This component is affected by a number of processes, and represents the contribution to DIC by anthropogenic carbon emissions (C^{anth}) and subducted DIC disequilibria (C^{dis}). Any errors that accumulate through violations of the underlying assumptions will also affect this component. It is not trivial to distinguish these components, and so a common approach is to cautiously interpret C^{res} with all of these factors in mind. Thus, an empirical decomposition of DIC fields in terms of four contributions from different processes is found that can readily be calculated from water sample temperature, salinity, DIC, alkalinity, and oxygen concentrations, equation (4.4).

$$C = C^{sat} + C^{soft} + C^{carb} + C^{res} \tag{4.4}$$

4.3 Model Validation

To determine whether this modelling setup produces a realistic carbon cycle variability, observed DIC fluctuations are compared against those of the model. This work aims to quantify how much saturation, the soft tissue pump, the carbonate pump, disequilibria and anthropogenic carbon contribute to DIC variability on interannual timescales up to the end of the current century. Since large scale observations of ocean biogeochemistry only cover the most recent four decades (*Olsen et al.*, 2016), it is not possible to comprehensively validate the model's ocean carbon

cycle variability over the interannual to multidecadal timescales that are studied here. Instead, the temporal variability of C^{sat}, C^{soft}, C^{carb}, and C^{res} is quantified wherever there are repeated cross-basin observations. In this way, it is possible to determine whether the model's ocean carbon cycle varies over years to decades in a way that resembles the world ocean. In particular, this validation aims to identify if observations show any important variability that is not represented in the model.

Version two of the GLODAP database contains the largest collection to date of ocean interior biogeochemical data in a common format (*Key et al.*, 2015; *Olsen et al.*, 2016). GLODAPv2 contains geolocated values of ocean biogeochemical parameters including DIC, alkalinity and oxygen, as well accompanying physical water properties dating between 1972 and 2013. The observations most useful for this study are full-depth hydrographic sections with biogeochemical parameters that have been repeatedly occupied over several years.

Table 4.2: Summary of repeat hydrography drawn from GLODAPv2

Initial	**Ocean**	**Region**	**Direction**	**Total Repeats**	**Total Years**
ACM	Atlantic	Central	Meridional	4	19
AEM	Atlantic	East	Meridional	7	11
ANZ	Atlantic	North	Zonal	4	19
ASZ	Atlantic	South	Zonal	3	25
ICM	Indian	Central	Meridional	2	1
IEM	Indian	East	Meridional	3	13
ISZ	Indian	South	Zonal	3	15
PEM	Pacific	East	Meridional	2	14
PNZ	Pacific	North	Zonal	2	10
SAM	Southern	Atlantic	Meridional	7	25
SAZ	Southern	Atlantic	Zonal	2	3
SIM	Southern	Indian	Meridional	3	16

Table 4.3: Additional information on hydrographic data drawn from GLODAPv2

Initial	**Other Names**	**Ship(s)**	**PI(s)**	**References**
ACM	A16 SAVE	Malcolm Baldrige Knorr, Melville R.H. Brown	R. Wanninkhof, D.K. Atwood, T. Takahashi, J. Bullister N. Gruber, S. Doney	(*SAVE*, 1992) (*Peltola et al.*, 2005)
AEM	A16N	Malcolm Baldrige, Knorr, Discovery L'Atalante, Thalassa R. H. Brown	R. Wanninkhof, D.K. Atwood, L. Talley, D. Smythe-Wright, L. Prieur, M. Bianchi, J.C. Gascard, J. Bullister N. Gruber	(*Johnson et al.*, 2003) (*Alvarez et al.*, 2005) (*Mémery et al.*, 2005) (*Peltola et al.*, 2005)
ANZ	A5	Hesperides, R.H. Brown, Discovery	G. Parilla, D. Bitterman, K. Lee, S. Cunningham, B. King (*Schuster et al.*, 2014)	(*Millero et al.*, 2000) (*Lee et al.*, 2003) (*Chung et al.*, 2004) (*Cunningham*, 2005a,b)
ASZ	SAVE A10	Knorr, Melville R.H. Brown, Mirai	T. Takahashi, M. Baringer, A. Macdonald, Y. Yoshikawa	(*SAVE*, 1992) (*Uchida et al.*, 2005)
ICM	I8N	Knorr, Malcolm Baldrige	L. Talley, R. Molinari	(*Peltola et al.*, 1998) (*Johnson et al.*, 2002)
IEM	I8I9	Knorr, Roger Revelle	A. Gordon, J. Swift J. Sprintall	(*Johnson et al.*, 2002)
ISZ	I5	Knorr, Roger Revelle	L. Talley, J. Swift	(*Johnson et al.*, 2002)
PEM	P18	Discoverer, R.H. Brown	B. Taft, G. Johnson, J. Bullister	
PNZ	P2	Kaiyo Maru, Melville	K. Okuda, P. Robbins, J. Swift	(*Watanabe et al.*, 1999)
SAM	A12/S2	Polarstern, Meteor, A.S.Vavilov, Marion Dufresne, R.H. Brown	E. Augstein, W. Roether S. Gladyshev, S. Speich U. Bathmann, E. Fahrbach, H. de Baar, J. Bullister, R. Key	(*Chipman et al.*, 1994) (*Hoppema*, 2004) (*González-Dávila et al.*, 2011)(*van Heuven et al.*, 2011b) (*Huhn et al.*, 2013)
SAZ	S4A	Polarstern	E. Fahrbach, H. de Baar	(*Huhn et al.*, 2013)
SIM	I6S	Marion Dufresne, Roger Revelle	A. Poisson, K. Speer	

Twelve long hydrographic sections were identified in GLODAPv2 that would be suitable for this validation (Table 4.2, Figure 4.1). Further details about the hydrographic sections can be found in Table 4.3, including references to individual datasets and cruise reports. Sections had to meet the following criteria to be useful in this analysis; 1) they must have been occupied at least twice 2) they sampled all of the following parameters necessary for the decomposition: temperature, salinity, pressure, oxygen, total alkalinity, DIC 3) stations were spaced no more than 111km along section with a the vertical resolution similar to the optimal 24 samples advised under the WOCE program (*WOCE*, 2003) 4) repeat surveys had to be within 220km of previous occupations. With the exception of the Arctic, all of the other major ocean basins are sampled in these twelve sections, although coverage is hardly global. The Atlantic basin is the best covered by repeat hydrography, with two sections (AEM and ANZ) covering the North, one section occupying the South (ASZ) and one central basin, full meridional section (ACM). The Southern Ocean is covered by three repeat sections (SAZ, SAM and SIM), although all are in or near the Atlantic sector. The Indian Ocean is covered by three sections, two meridional (ICM and IEM) and one zonal (ISZ). The Pacific Ocean is severely lacking coverage, with one zonal section (PNZ) and one meridional section in the eastern basin (PEM).

Although repeated hydrographic sections typically aim to occupy sampling stations in the same locations with each survey, in practice this is often not the case. To make a given section's repeat surveys quantitatively comparable to one another and to the modelled fields, it is necessary to regrid both onto common grids. First, at each station values of seawater density were calculated as potential density anomalies from a 4000 dbar reference pressure (σ_4, kg m^{-3}) for each DIC datapoint using standard tools (*McDougall and Barker*, 2011). The biogeochemical parameters (DIC, A_T and oxygen) were then interpolated onto a high resolution density grid using a piecewise cubic hermite interpolating polynomial (PCHIP). Where gaps in profiles were larger than 1 kg m^{-3}, no interpolation was performed. This is because it is not possible to solve for correct property/density gradients over large density intervals. Then, a generic cruise track for each of the 12 sections was drawn by selecting the model's spatial grid cells coincident with the real world

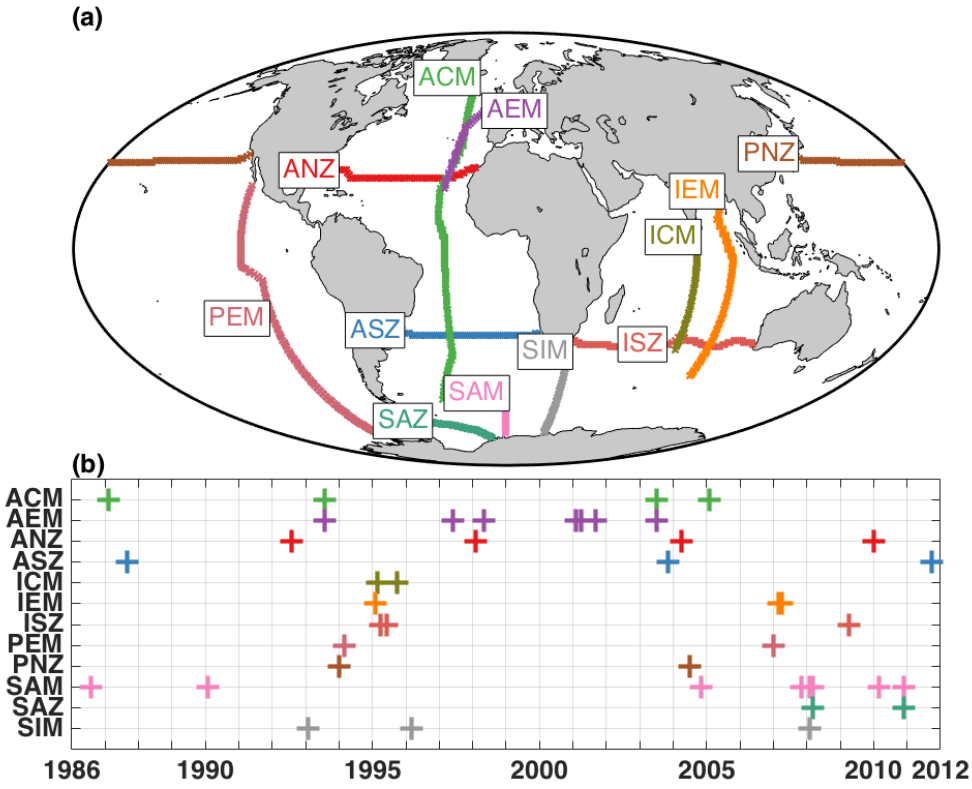

Figure 4.1: Distribution of repeatedly occupied hydrographic sections with biogeochemistry in space (a) and time (b)

cruise tracks. Each station was matched to the nearest grid cell of the ORCA1 model grid (*Madec and Imbard*, 1996). Where more than one station was matched to a grid cell, profiles were averaged together to generate uniform transects of data in space and density.

$$RMS(\mathrm{C}) = \sqrt{\overline{(\mathrm{C} - \bar{\mathrm{C}})^2}} \tag{4.5}$$

Along each section for each occupation, fields of C^{sat}, C^{soft}, C^{carb} and C^{res} were then calculated using the method described in section 4.2.2. For each section occupation, a single occupation-mean density profile was calculated each of the four DIC components. At each density level, the time mean concentration ($\bar{\mathrm{C}}$) was calculated, then the difference of each year from the time mean was found ($\mathrm{C} - \bar{\mathrm{C}}$). These anomalies were squared, and the mean squared anomaly calculated. Finally, the square root of the mean squared anomalies was calculated to yield the temporal

root-mean-square (RMS) at each density level, equation (4.5). This was done for all density levels and each DIC component to give density profiles of variability.

Model sections were then generated by collecting monthly average model output corresponding to the time of each observation. Observations represent snapshots of the real world at single fixed points, whereas the model output used in this comparison is available as only monthly averages of 1-by-1 degree by several vertical metres for each grid cell. This means that the comparison of a model grid cell value to an observation is not like-for-like, but is at least a best available approximation. Furthermore, modelled variability is uncorrelated with real world variability because nature experiences different random variations than a forced model. For example, if at a given location, August 1990 showed anomalously high DIC, one would not expect DIC at that location in the model to also be anomalously high in August 1990, because the two systems experience different forcing and random variations. Even if the model replicated the patterns and magnitudes of real world variability perfectly, the chaotic nature of the Earth system would mean than an alignment of variability between the real world and the model is unlikely. Therefore, it is inappropriate to compare model output and observations directly. Instead, it is more meaningful to compare statistics about modelled and observed variability to determine if the model behaves realistically. Continuing with the previous example, a more useful comparison would be to examine the time variance of August DIC at the location in the model and real world.

To compare the modelled and observed variability statistically, ensembles of modelled sections were collected. For example, The Atlantic Central Meridional (ACM) section was occupied in Feb 1987, Aug 1993, Jul 2003 and Feb 2005. For each of those occupations, occupation-mean density profiles along that section were calculated for each of the DIC components. For visualisation purposes, these density profiles are plotted in DIC-pressure space by calculating the section-mean sea pressure at each density point (coloured lines in Figure 4.2a-d). The temporal variability down each profile is then shown as the temporal RMS (thick black lines in Figure 4.2e-h). The upper 2000 dbar are plotted to focus on the upper water column because this is where most of the relevant DIC variability occurs. While this validation focuses on the upper 2000 dbar, the rest of the results presented in

Table 4.4: Example description of how model ensembles are formed for the ACM section

Occupation Years	**Model Years**	**Ensemble Member**
1987, 1993, 2003, 2005	1991, 1997, 2007, 2009	Year + 4
	1990, 1996, 2006, 2008	Year + 3
	1989, 1995, 2005, 2007	Year + 2
	1988, 1994, 2004, 2006	Year + 1
	1987, 1993, 2003, 2005	Year ± 0
	1986, 1992, 2002, 2004	Year − 1
	1985, 1991, 2001, 2003	Year − 2
	1984, 1990, 2000, 2002	Year − 3
	1983, 1989, 1999, 2001	Year − 4

this chapter include the full water depth.

Model output at the same location at the same time was then analysed in the same way to generate one ensemble member. Eight additional ensemble members were collected (for a total of 9 ensemble members) by using output from each of the four years before and four years after the observed years. For example, the year−1 ensemble member uses output from the same months but the years 1986, 1992, 2002 and 2004, Table 4.4. The minimum-maximum range of the ensemble's occupation-mean profiles are shown in the grey envelopes in Figure 4.2a-d. Therefore, if the observed mean profiles in Figure 4.2a-d lie within the grey envelopes, then the model's occupation means are plausible to first order. Similarly, the modelled ranges of the RMS profiles are shown by the grey envelopes in Figure 4.2e-h. Any major inconsistencies between the observations and the model are highlighted by comparing the observed RMS profile with the grey envelopes. This comparison is useful because the timescale of variability compared between the model and observations is always consistent. Note that for both the model and observations, variability at any density level can only be calculated if at least two occupations of a given section had DIC data. Note also that no assertions are made that a meaningful estimate of observed biogeochemical variability can be drawn from the comparison of two occupations. Rather, what is presented here is a method to make use of whatever data are available, regardless of the obvious sampling limitations.

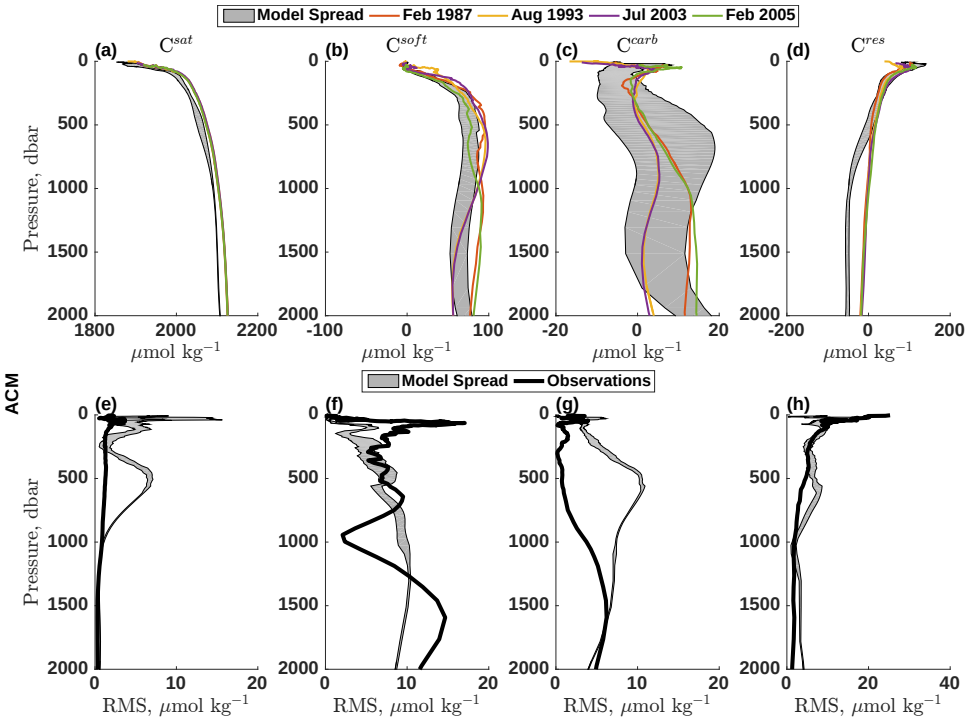

Figure 4.2: Modelled and observed variability of DIC components along the Atlantic Central Meridional (ACM) section

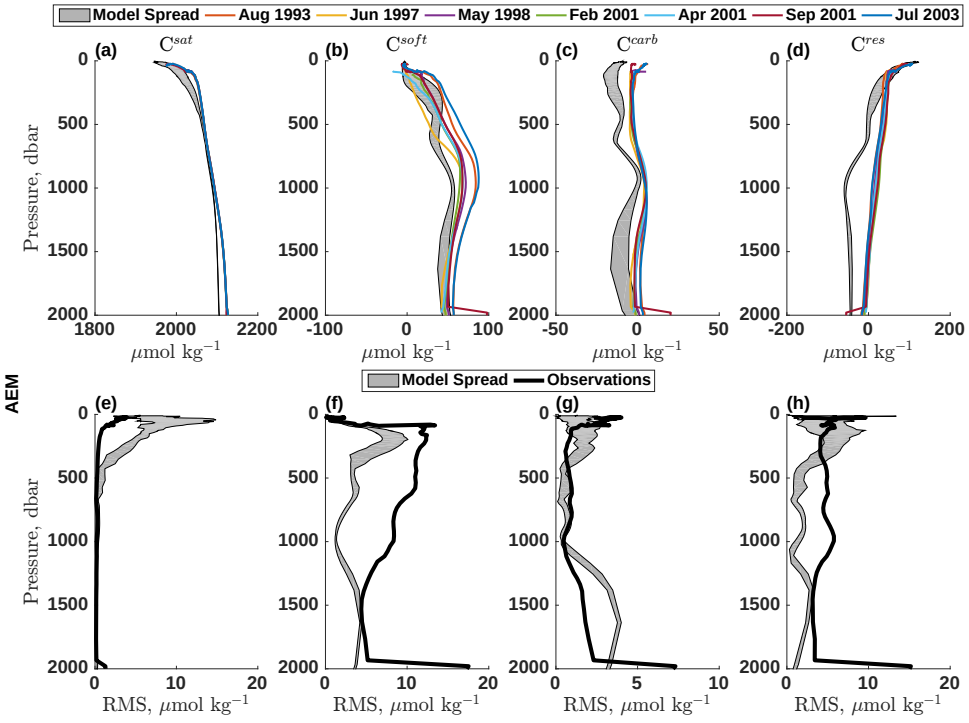

Figure 4.3: Modelled and observed variability of DIC components along the Atlantic East Meridional (AEM) section

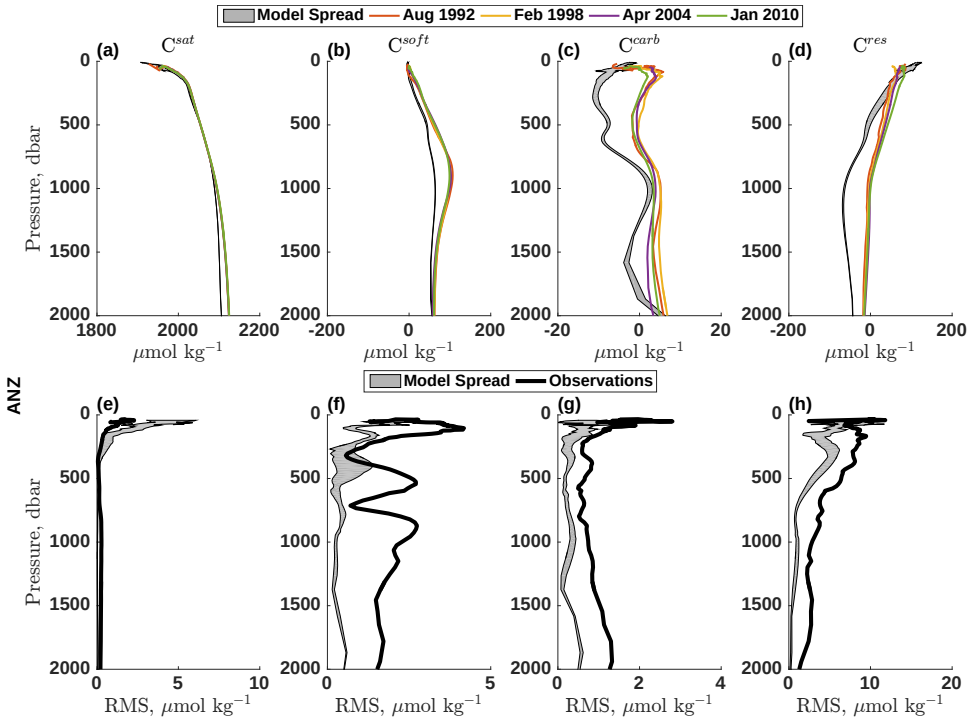

Figure 4.4: Modelled and observed variability of DIC components along the Atlantic North Zonal (ANZ) section

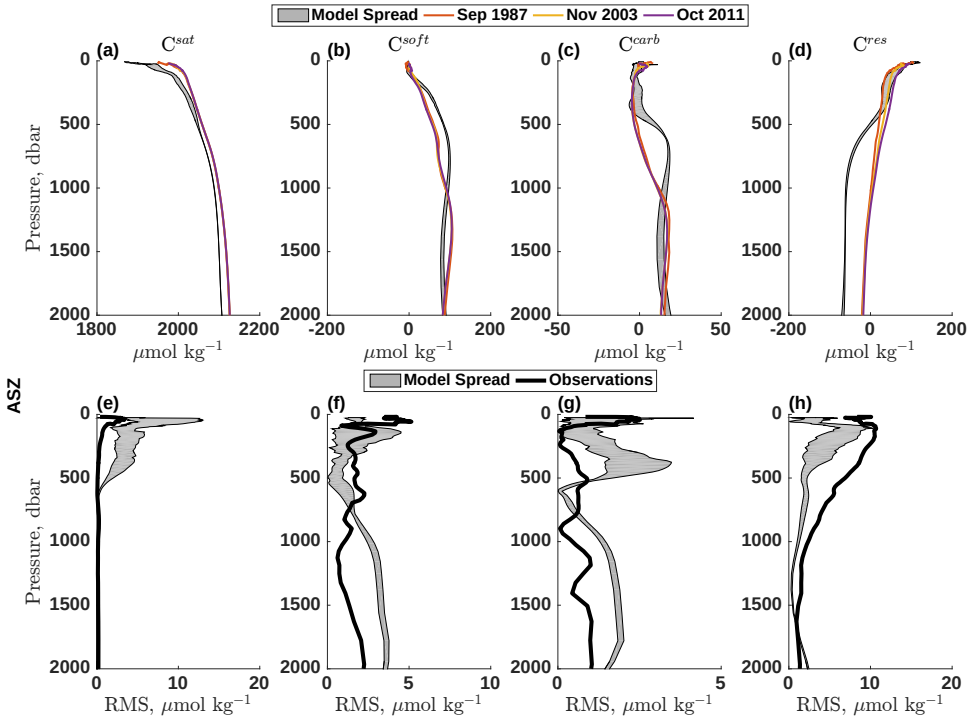

Figure 4.5: Modelled and observed variability of DIC components along the Atlantic South Zonal (ASZ) section

4.3.1 Atlantic

For Atlantic waters shallower than 500 dbar, agreement between modelled and observed mean DIC component profiles is generally good, within 10 μmol kg^{-1} (Figures 4.2-4.5a-d). C^{carb}, however shows a low bias in all four Atlantic locations for the upper water column (Figures 4.2-4.5c). Beneath the thermocline, ($>$ 750 dbar) the model tends to show low biases in C^{sat} and C^{res} (10s of μmol kg^{-1}).

Across the Atlantic, the model tends to predict larger temporal variability in C^{sat} in the upper 500 dbar than the observations indicate. Data from two Atlantic locations indicate that model also underestimates C^{soft} variability (Figure 4.3f, 4.4f). The model also fails to reproduce the deep C^{soft} maximum and its variability around 1000 dbar in the subtropical gyre at 24°N (Figure 4.4b and f). However, this is most likely due to its displacement further south in the model than a total absence because the deep C^{soft} maximum is visible in the full basin meridional section (ACM, Figure 4.2b and f). Agreement between the model and observations for C^{carb} and C^{res} variability is generally quite good, with some low biases.

4.3.2 Indian

Repeat basin-scale biogeochemical hydrography in the Indian Ocean is lacking, and none of these three sections have been occupied in more than two years. This validation is therefore insufficient to make confident statements about multi-year DIC variability. Mean DIC component density profiles appear to be well modelled. The model shows a systematic low bias in C^{sat} (Figure 4.6-4.8a), as well as in C^{res} below approximately 500 dbar (Figure 4.6-4.8d).

With the limitations of temporal coverage aside, the match is quite close between the model ensemble spread and observed variability (Figure 4.6-4.8e-h). Therefore, the limited (mostly seasonal) temporal variability observed in the Indian Ocean appears to well modelled.

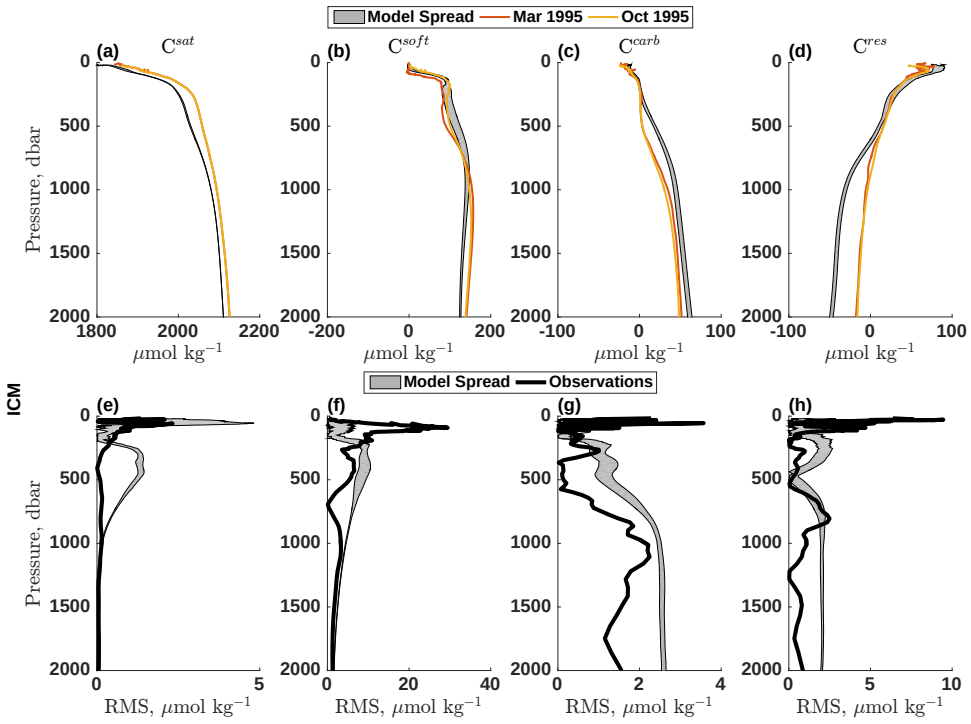

Figure 4.6: Modelled and observed variability of DIC components along the Indian Central Meridional (ICM) section

4.3.3 Pacific

This approach to model validation identifies in GLODAPv2 only two repeatedly occupied hydrographic sections with detailed biogeochemical measurements in the Pacific Ocean. Moreover, both sections were only occupied twice, and so only a very limited assessment of Pacific interannual carbon cycle variability can be made here. There is a systematic low bias in C^{sat} (Figures 4.9-4.10a), and the deep C^{carb} maximum appears somewhat overestimated (Figure 4.9c) although this bias is less pronounced zonally (Figures 4.10c) The model also shows a high bias in C^{res} in the upper 1000 dbar (Figure 4.9d).

The Pacific observations suggest generally low variability in all of the carbon components below 500 dbar, with the differences in C^{soft} and C^{carb} (Figure 4.10b,c,f,g) appearing to arise due to subtle variations in curvature of profiles rather than clearly genuine variability. Much of the observed Pacific DIC variability appears to be associated with C^{res}, which is somewhat underestimated in the model (Figure 4.9-4.10d,h).

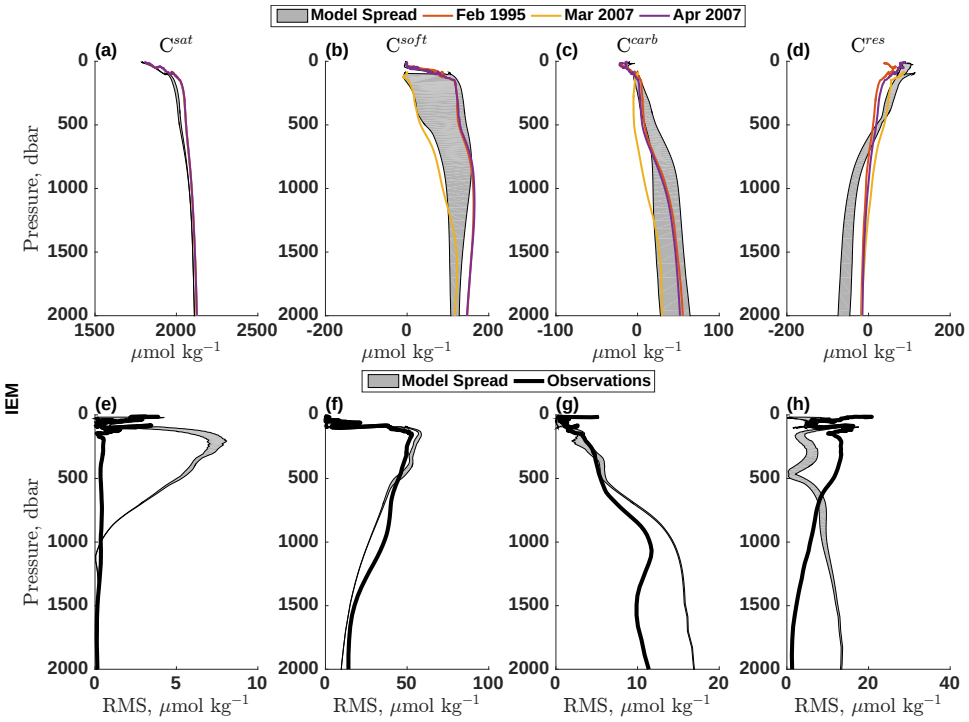

Figure 4.7: Modelled and observed variability of DIC components along the Indian East Meridional (IEM) section

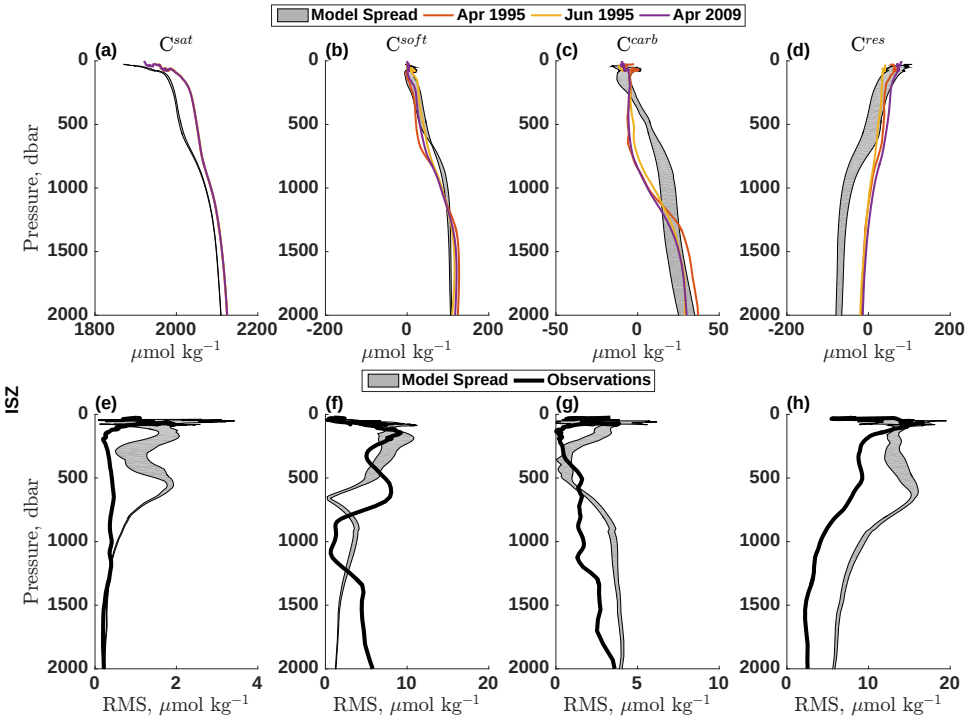

Figure 4.8: Modelled and observed variability of DIC components along the Indian South Zonal (ISZ) section

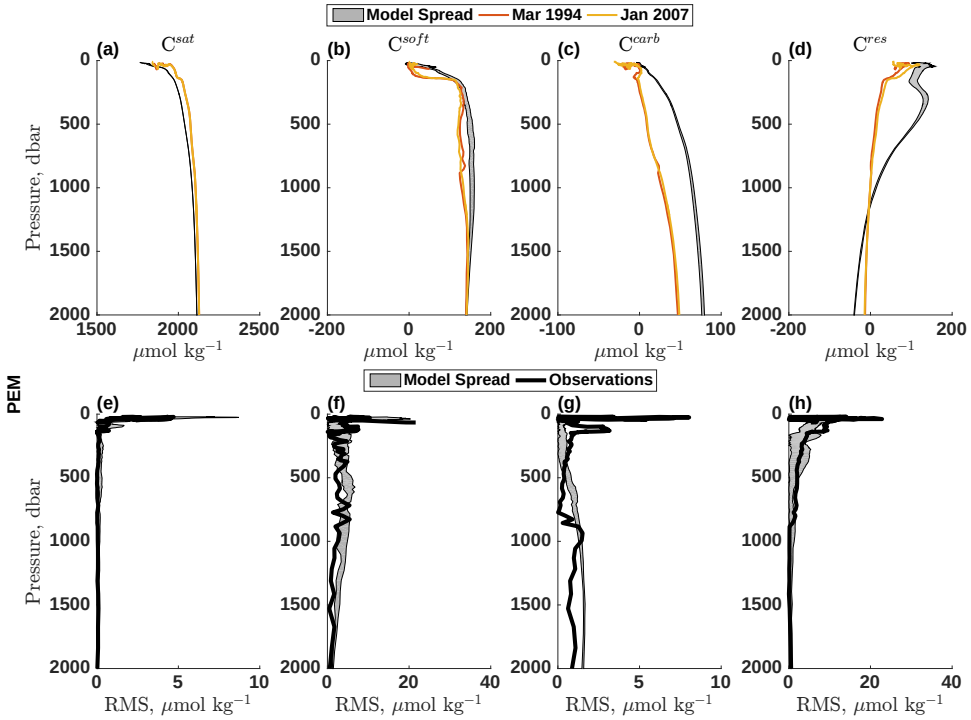

Figure 4.9: Modelled and observed variability of DIC components along the Pacific East Meridional (PEM) section

4.3.4 Southern

The Southern Ocean data show that the model has a low bias for C^{sat} in all three locations, although the shape of profiles is in agreement with observations (Figure 4.11-4.13a). In addition, modelled C^{carb} is often overestimated (Figure 4.11-4.13c). Outside of the Weddell Sea (where the SAZ data lie), the mean structure of C^{soft} and C^{res} are well modelled (Figure 4.11b and4.13b).

Counterintuitively, the Southern Atlantic Meridional section has the best temporal coverage of all the sections described here, and therefore represents a particularly useful timeseries for model validation. In general, the observed variability closely matches that of the model (Figure 4.11e-h), although unrealistically large C^{res} variance is indicated in waters deeper than about 200 dbar. In the surface waters at the Atlantic-Indian sector boundary (SIM), modelled variability matches the observations (Figure 4.13e-h). The jump in variability at 200 dbar arises with the inclusion of the 1993 occupation (which had insufficient surface data). For these deeper waters, the model shows higher variability than the observations indicate for C^{sat}, C^{carb} and C^{res}(Figure 4.13e,g,h).

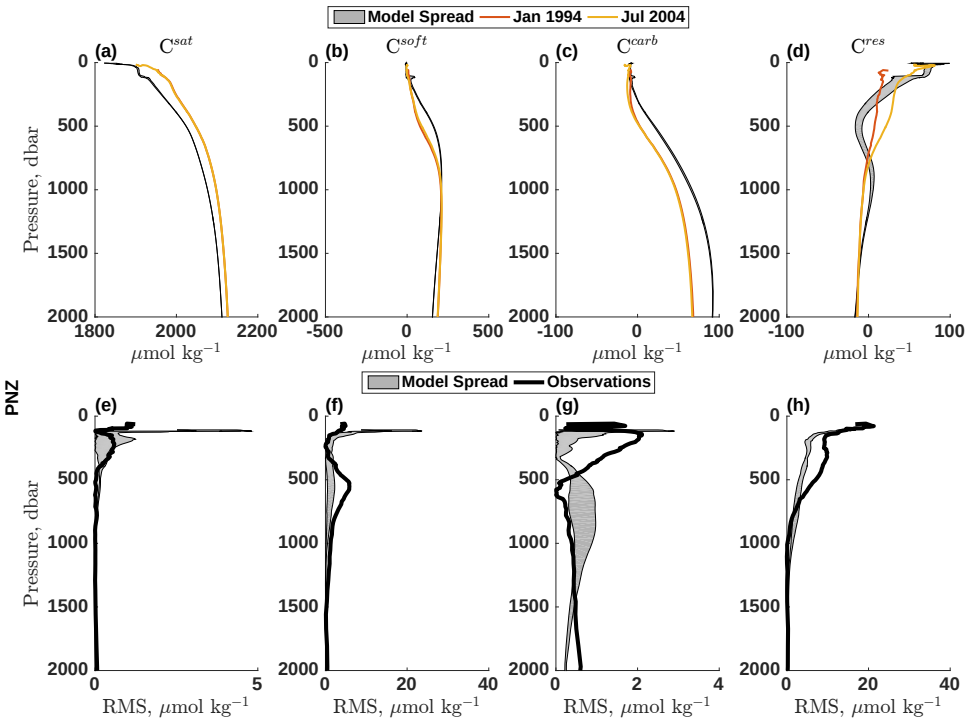

Figure 4.10: Modelled and observed variability of DIC components along the Pacific North Zonal (PNZ) section

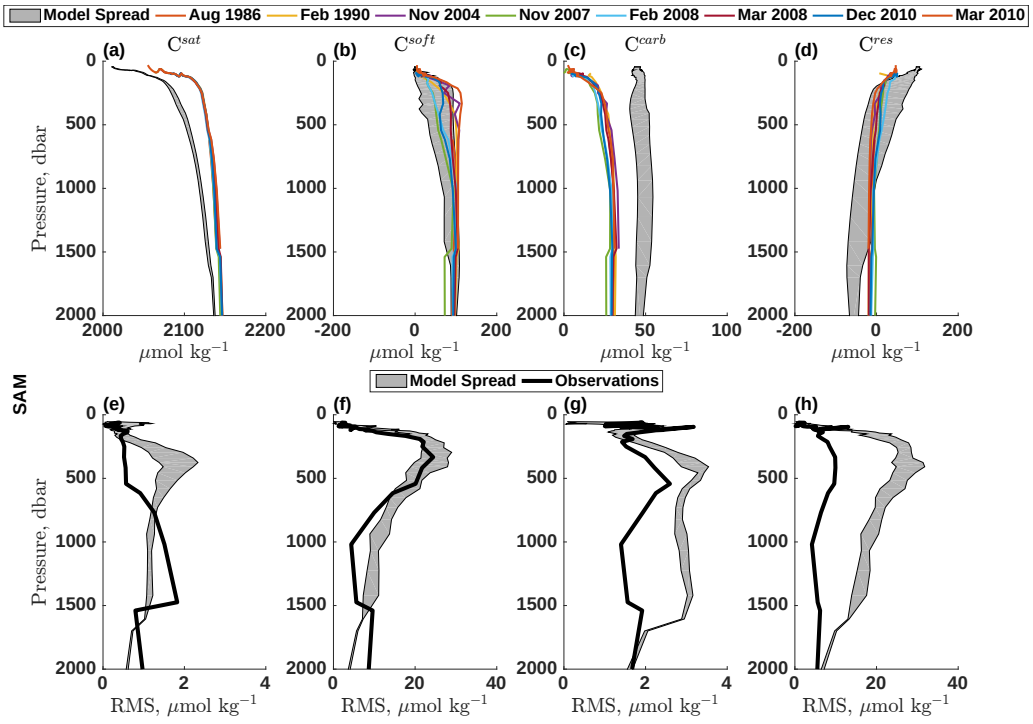

Figure 4.11: Modelled and observed variability of DIC components along the Southern Atlantic Meridional (SAM) section

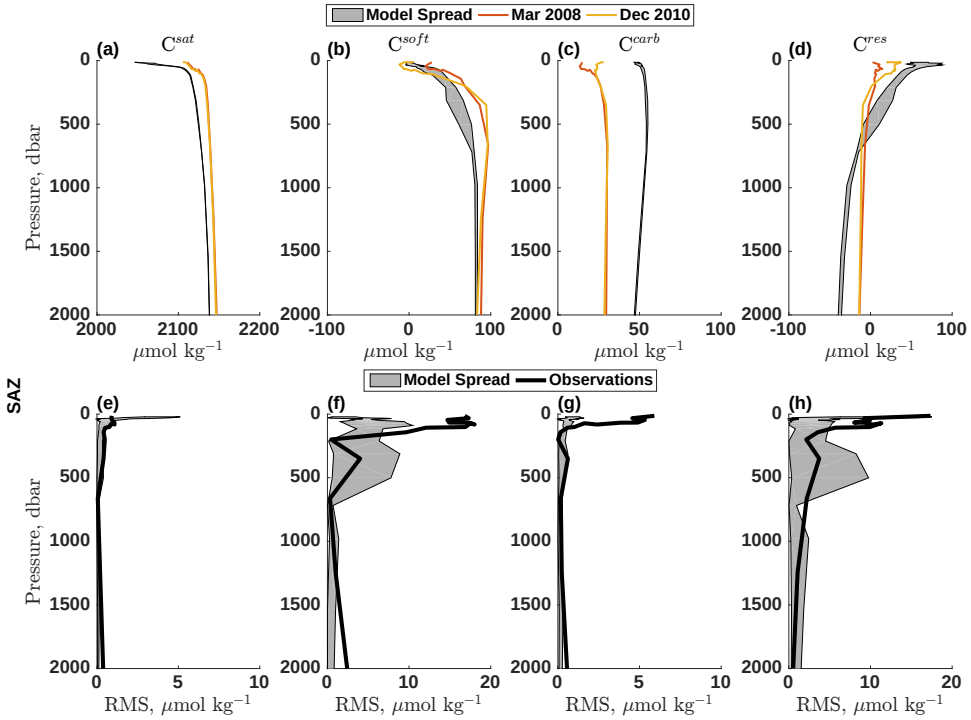

Figure 4.12: Modelled and observed variability of DIC components along the Southern Atlantic Zonal (SAZ) section

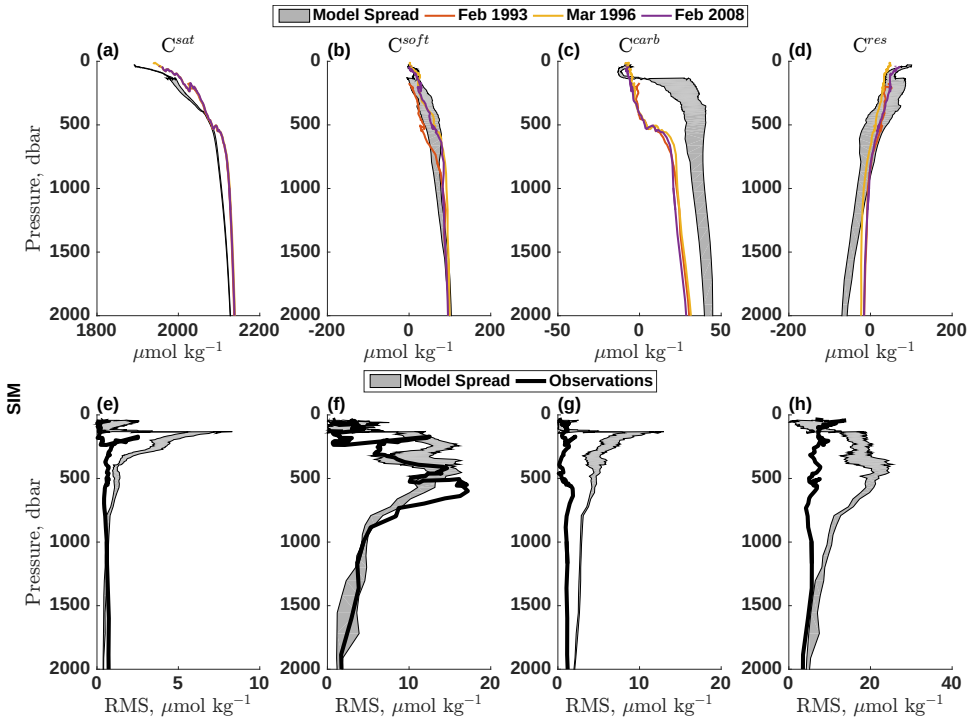

Figure 4.13: Modelled and observed variability of DIC components along the Southern Indian Meridional (SIM) section

4.3.5 Validation Summary

While it is necessary to compare modelled and observed DIC variability in detail as in the previous section, a broader, bigger picture comparison is also useful.

The observed upper ocean variability of each DIC component can be summarised by first regridding the RMS profiles onto a regular pressure grid, then taking the mean value of the temporal RMS across the upper 2000 dbar, giving equal weight to each pressure level (thick black lines in Figures 4.2-4.13e-h) for each of the 12 hydrographic sections (green bars in Figure 4.14). Similarly, the mean values of the upper and lower limits of the ranges of modelled variability in the upper 2000 dbar can also be calculated in the same way (orange diamonds in Figure 4.14).

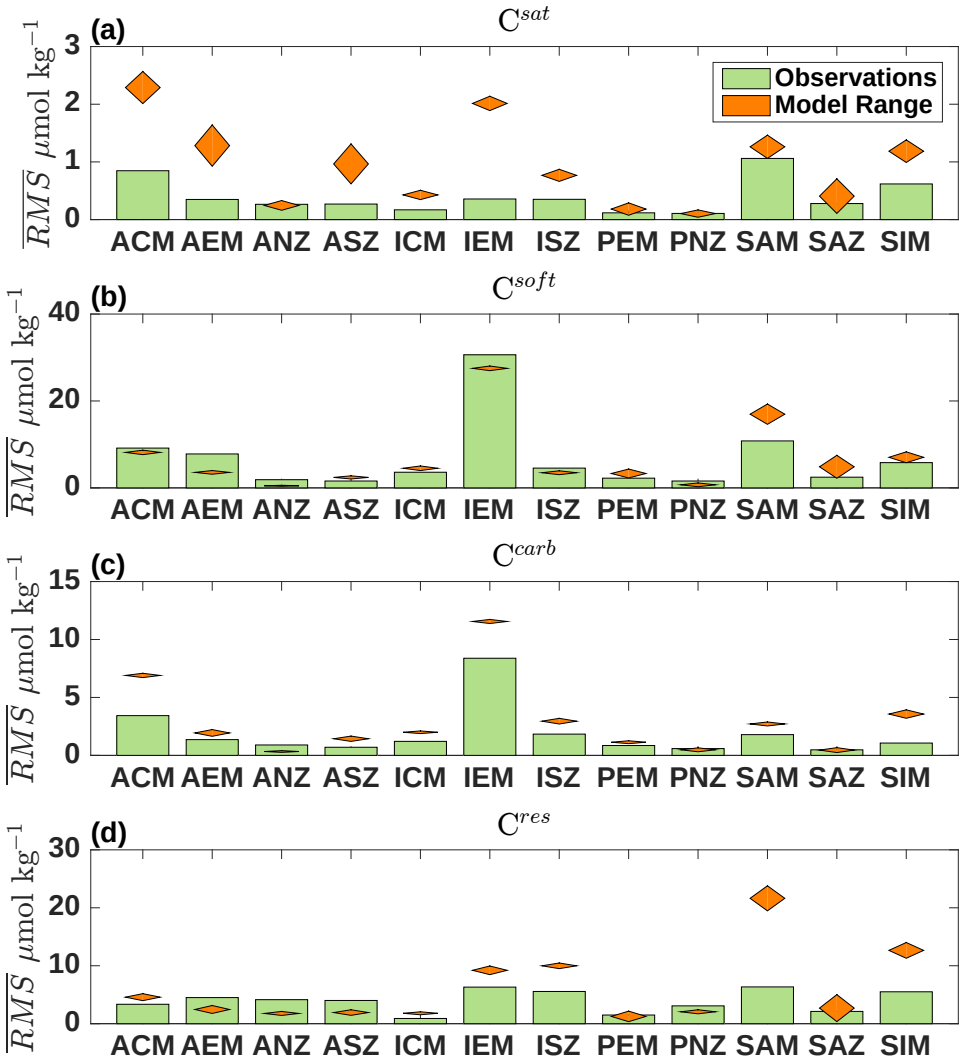

Figure 4.14: Comparison of observed versus modelled DIC component variability for C^{sat}, C^{soft}, C^{carb}, and C^{res} (a-d). Green bars show pressure-averaged temporal variability in the upper 2000 dbar for 12 repeat hydrographic sections sites. The vertical extent of the orange diamonds shows the equivalent range of modelled temporal variability.

This validation does not identify any large unmodelled DIC component variability, although clear discrepancies exist, Figures 4.2-4.13. The validation process highlights frequent underestimation of C^{sat}. Note that the low bias is on the order of 10-20 μmol kg^{-1}, which is large enough to be considerable, given the internal DIC consistency of 4 μmol kg^{-1} achieved in GLODAPv2 (*Olsen et al.*, 2016). This low bias is mostly associated with the preformed alkalinity (see Section 3.2.1), although model temperature biases play a secondary role. Estimating interior preformed alkalinity is done by using a linear regression of surface alkalinity against surface salinity on the model field, and so that regression is sensitive to those two fields. In the model, surface mean salinity agrees relatively well with observations, but modelled alkalinity shows a low bias of order 10 μeq kg^{-1}. This leads to a low bias of preformed alkalinity, which is likely to be the main driver of the C^{sat} low bias. *Yool et al.* (2013a) describe how high biases in primary production (particularly in the Pacific) causes increased $CaCO_3$ production, lowering surface alkalinity.

The model tends to show larger C^{sat} variability in the upper Atlantic than is indicated in the observations (Figure 4.14a). The previous chapter presented results suggesting that saturation carbon variability in the North Atlantic drives most of the interannual variability in the basin's DIC inventory. If the model's overestimation of C^{sat} variability is widespread across the North Atlantic, then there could be issues with the experimental setup that could weaken the conclusions presented in the previous chapter. However, since saturation variability in the model compares well with observations along the 24°N section (ANZ), the discrepancies in the eastern basin (at the ACM and AEM sections) could reflect a front in the model with misplaced zonal extent. Such a misplacement of a front would have pronounced effects locally but may not be critical at the basin scale, and so the low variability bias at the ACM and AEM sections does not necessarily undermine the conclusions entirely.

Broadly, most of the observed C^{soft} variability occurs in the upper 500 dbar, and the validation shows that much of this is captured in the model setup, Figure 4.14b). The model represents C^{carb} and its variability quite well away from the Southern Ocean, but misplaces the $CaCO_3$ saturation horizon in some regions. These issues likely stem from MEDUSA-2's tendency for excessive upper ocean

$CaCO_3$ dissolution that have been previously documented (*Yool et al.*, 2013a), a direct cause of which has not yet been identified. *Yool et al.* (2013a) also draw attention to the fact that global total $CaCO_3$ production in MEDUSA-2 is on the low end of observation-based estimates, which is difficult to reconcile alongside the high C^{carb} biases without dedicated investigation.

There is also a tendency for the model to under-represent C^{res}. It is difficult to confidently account for these differences because of the range of factors that affect C^{res} (namely errors in the decomposition, C^{anth} and C^{dis}). However, the main conclusions of this chapter are not reliant on the quantification of C^{res}; the following analysis of this chapter instead uses the tracer based diagnoses of DIC components (Section 3.2.2), rather than the empirical method (Section 4.2.2). Nevertheless, this validation indicates that interpretation of C^{dis} should be carried out with caution as this component is the least confidently validated. The rest of the analysis going forward described in this chapter uses the model decomposition (rather than the empirical method employed for this validation only).

4.4 Results

4.4.1 Global DIC Variability

In addition to analysing the global ocean DIC inventory as single reservoir, model output was also subdivided geographically into five basins Atlantic, Pacific, Indian, Southern and Arctic (Figure 4.15). The Southern Ocean is taken to be the region south of 45°S. The Atlantic includes the Labrador Sea but not the Greenland-Iceland-Norwegian Sea north of Iceland (poleward of 68°N). The Indian Ocean is bounded by 45°S to the south, 28°E to the west, 130°E to the east, and does not include the inland seas of Southeast Asia. The Pacific is bounded across the Bering Strait at 68 °N and includes the seas of Southeast Asia. The Arctic is therefore the basin northward of others. The major inland seas of the Baltic, Mediterrannean and Hudson Bay are masked out of all basins in this analysis. Annual average DIC basin totals for the full depth global ocean and its five sub-basins and its five components were calculated for each year to generate time series. These time

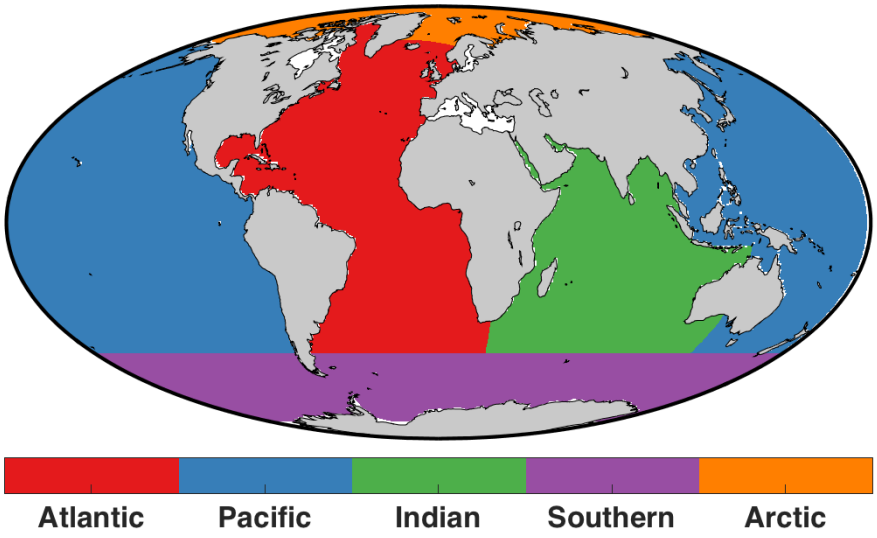

Figure 4.15: Delineation of basins

series were then filtered into four temporal components using the same procedure as in Section 3.4.1, separating out the interannual (1-5 year), decadal (5-20 year), multidecadal (>20 year) and trend variability. The same statistical methods were applied to these basin DIC series as discussed in Section 3.4.1: Inventory RMS to determine magnitudes of variability, correlations to determine strength of component covariance with total DIC and regression slope to determine the degree to which components produce anomalies in DIC.

Interannual variability in DIC is largely driven variability in soft tissue carbon (Figure 4.16a-c). There is a considerable but incompletely compensating effect of disequilibrium that also plays a role in setting total DIC interannual variability. This global result strongly contrasts the main results of the previous chapter, in which North Atlantic interannual variability in DIC was driven almost entirely by the saturation component. Clearly then, the North Atlantic is not the main ocean region driving global DIC variability.

Looking to longer timescales, decadal DIC variability is driven by strong variability in the uptake of anthropogenic carbon, with a secondary effect from C^{soft} (Figure 4.16d-f). As with the interannual variability, this result differs strongly from the results of the North Atlantic alone, suggesting the primacy of other locations in setting the global picture.

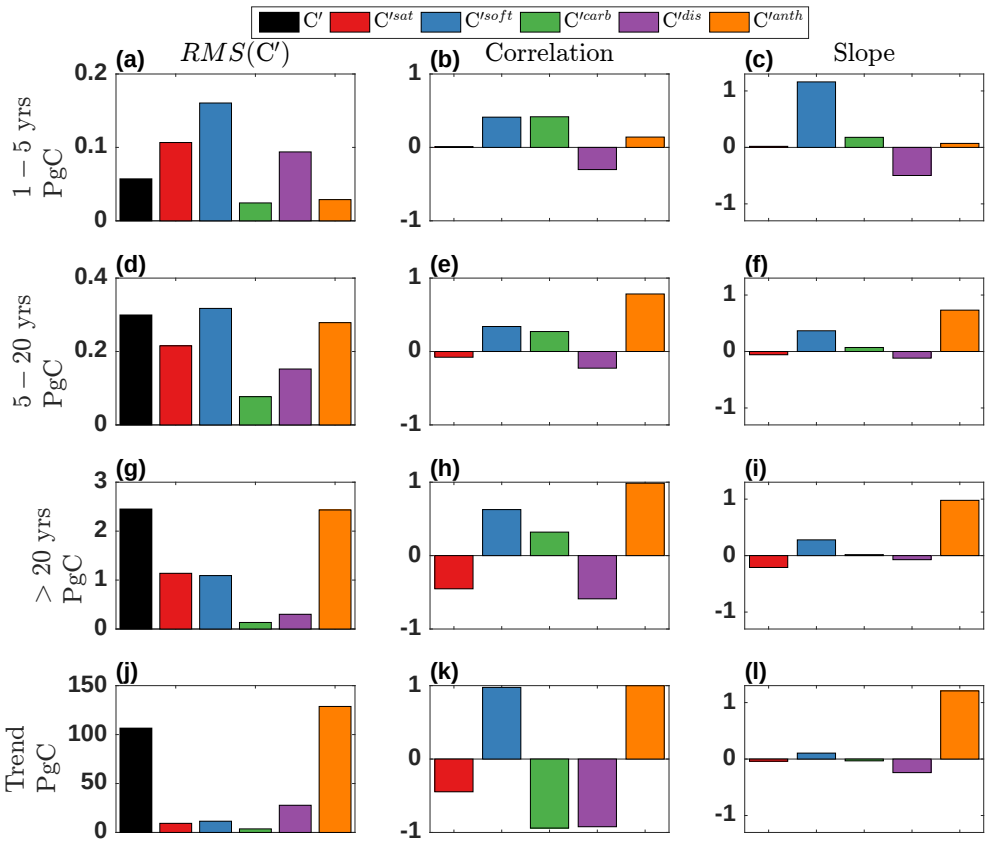

Figure 4.16: Statistics describing the relationship between global DIC component variability and total DIC inventory variability on four timescales: interannual (1-5 year, a-c), decadal (5-20 year, d-f), multidecadal (>20 years, g-i), and the long term trend (j-l). Left: root-mean-square (RMS) of anomalies of total DIC inventory (black) and DIC components (colours). Centre: Correlations between component and total DIC inventory anomalies. Right: Slope of regression line between component and total DIC inventory anomalies

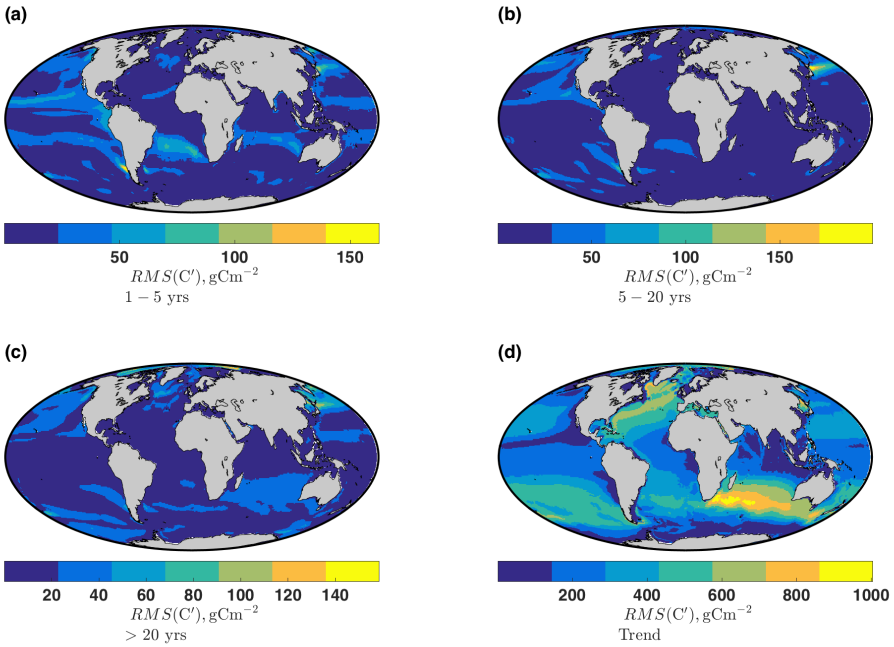

Figure 4.17: RMS of DIC anomalies at each gridpoint for the four filtered timescales, interannual (a), decadal (b), multidecadal (c) and the trend (d)

Multidecadal DIC variability is driven almost entirely by anthropogenic carbon uptake (Figure 4.16g-i). There are also important compensating effects of C^{sat} and C^{soft}, and since these two anticorrelated processes are of nearly equal magnitude, they nullify one another. The relative importance of these three components is similar for the North Atlantic as for the global ocean, but the size of multidecadal North Atlantic DIC anomalies (RMS = 0.23 PgC) is much smaller than anomalies at the global scale (RMS = 1.13 PgC) and so the North Atlantic is not the sole driver of global multidecadal DIC variability.

The overall global trend is driven by the uptake of anthropogenic carbon emissions (Figure 4.16j-l). By the end of the simulation, the global ocean DIC pool grows by 370 PgC. This is mainly driven by the accumulation of 400 Pg of anthropogenic carbon, although there is also a relatively small growth of the C^{soft} inventory. The other natural carbon pools show small declines by the end of the simulation.

To determine what drives variability in global fields of DIC, it is helpful to first look at where anomalies in DIC are large at the gridpoint scale. Water column inventories of DIC were calculated for each horizontal location by summing through

depth, and then rescaling (dividing) by grid cell area. The RMS of annual DIC column inventory anomalies from the long term mean were calculated, and this map shows where variability is large on each timescale (Figure 4.17). Interannual and multidecadal DIC variability is spread across: the upwelling regions off the western South American coast, the South Atlantic Gyre, the tropical Pacific, the subpolar Pacific, subpolar North Atlantic and West Australia/South Equatorial Current region (Figure 4.17a,b). The widespread, large RMS values across the Pacific indicate that a considerable portion of the global interannual and multidecadal DIC variability is driven by this basin.

Multidecadal variability is more diffusely spread everywhere except the equatorial oceans, especially in the Arctic, subpolar North Pacific and subpolar North Atlantic (Figure 4.17c). Rather than one single ocean basin overshadowing the others, global multidecadal DIC variability is comprised of important contributions from all the basins.

There is a large long term trend of DIC variability everywhere in the ocean ($RMS > 100$ gC m^{-2}), with the largest values ($RMS > 700$ gC m^{-2}) in the South Indian Ocean Gyre, North Atlantic, and widespread, large ($100 < RMS < 700$ gC m^{-2}) carbon accumulation over the extratropical Pacific and South Atlantic (Figure 4.17d).

4.4.2 Interannual Variability

To determine which components of DIC give rise to the variability shown in Figure 4.17, the regression slope of component anomalies against total DIC anomalies is calculated at each gridpoint. Maps of the impact of each component on column DIC inventory interannual variability are shown as the regression slope at each gridpoint multiplied by the RMS of DIC anomalies at each gridpoint, Figure 4.18. This scales the contribution of each component to the size of the total DIC variability, such that the sum of all five maps in Figure 4.18 produces the map in Figure 4.17a.

Large values of the C^{soft} slope $\times$ RMS(C') in the eastern Pacific (Figure 4.18b) indicate that the soft tissue component is the major driver of variability. In addition, because the values of the other impacts in this same region (eastern Pacific)

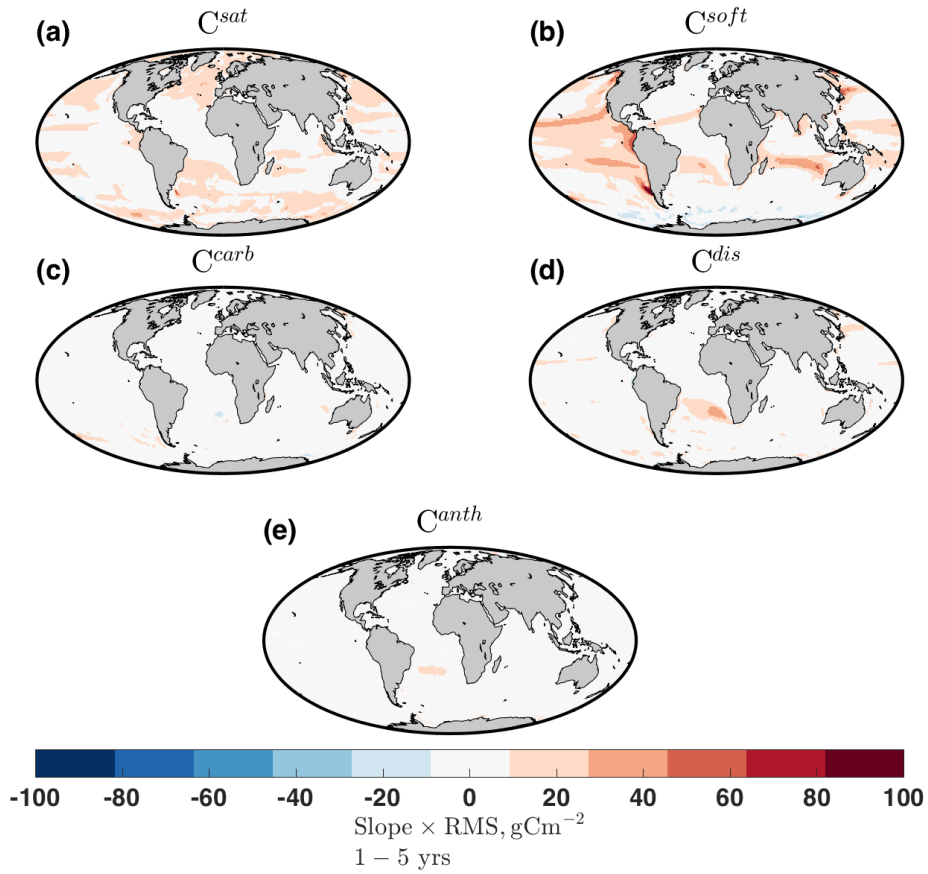

Figure 4.18: Impact of DIC components shown as slope of regression line between component and total DIC inventory anomalies scaled by RMS(C′) for interannual (1-5 year) variability, gCm^{-2}

are all small, the other components of DIC therefore are doing little to drive variability.

Note that just because a DIC component has moderate impact (slope × RMS(C′)) values over a large area (as for C^{sat} in Figure 4.18a) this does not mean that it is an important driver of DIC variability. For a component to have a large global impact, it must show strong coherent (rather than compensating) variability across a basin. Therefore, while C^{sat} is an important driver of interannual variability at many individual locations, its globally summed importance is minor because anomalies at different locations compensate eachother. Instead, C^{soft} drives most of the interannual global DIC variability. In the subtropical South Atlantic, C^{sat}, C^{soft}, and C^{dis} all drive local interannual DIC variability. In the northwestern Pacific to the east of Japan, C^{soft}, and C^{sat} are the two main drivers.

4.4.3 Decadal Variability

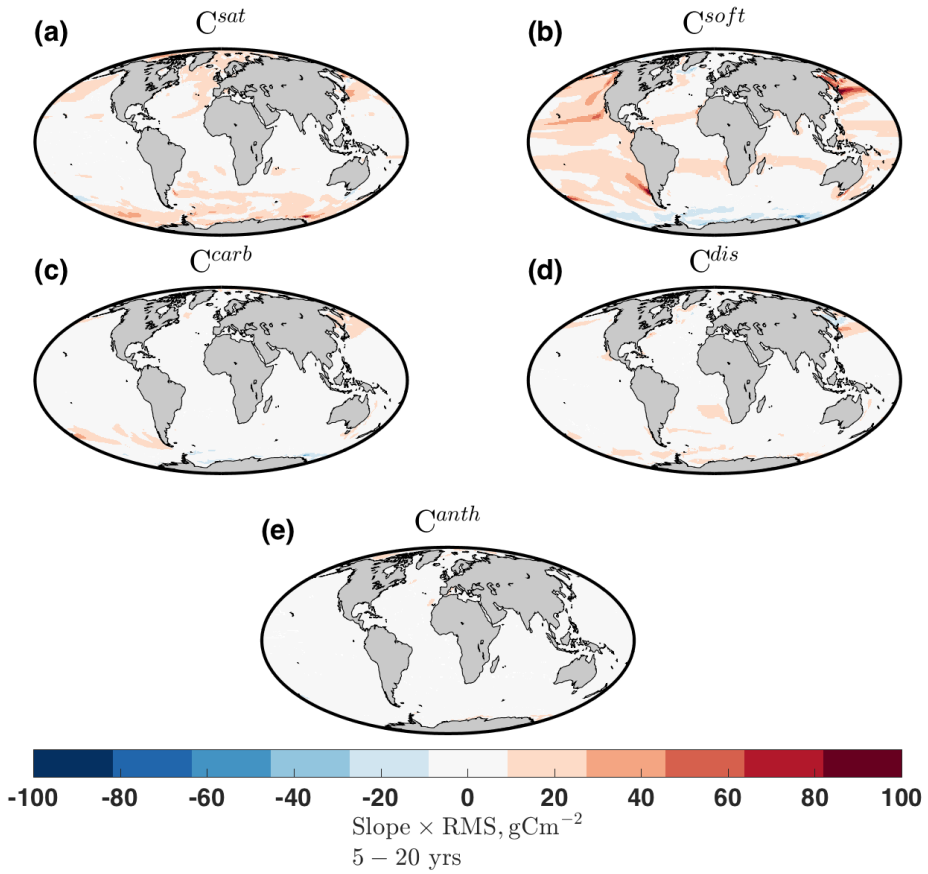

Figure 4.19: Impact of DIC components shown as slope of regression line between component and total DIC inventory anomalies scaled by RMS(C′) for decadal (5-20 year) variability, gCm^{-2}

The Pacific Ocean dominates the global decadal (5-20 year) DIC inventory variability, hosting the largest inventory anomalies per unit area (in the northwestern basin) as well as widespread moderate anomalies ($RMS > 25$ gCm^{-2}) Figure 4.17b). In these regions, C^{soft} is the dominant driver of variability, Figure 4.19b. In the northwestern Pacific the impacts of $C^{sat}$and $C^{carb}$are also important although smaller than that of C^{soft} (Figure 4.19a,c,d).

Interestingly, although the globally integrated decadal DIC variability shows a strong relationship with C^{anth} (Figure 4.16 d,e,f), this relationship is not apparent for pointwise column DIC inventories (Figure 4.19e). This can be reconciled by recognising that anomalies different gridpoints can compensate each other and sum to zero when integrated over the basin scale. Therefore, a plausible explanation is that seemingly large decadal variability of C^{soft}at the gridpoint scale (Figure 4.19b) could represent spatial redistributions within the basin that have little effect on the total basin DIC variability. On the other hand, variability in C^{anth} is likely to be coherent across a basin (everywhere responding to the monotonic atmospheric increase of atmospheric CO_2) and does not show compensating variability at different locations within a basin.

4.4.4 Multidecadal Variability

Multidecadal DIC variability is spread widely over the globe away from the tropics, with hotspots in the Arctic and northwestern Pacific (Figure 4.17c). The Arctic's multidecadal variability is strongly driven by C^{anth}, but is partly compensated by saturation effects, Figure 4.20a,e. C^{soft} variability is the dominant control in the subpolar North Atlantic and Pacific Oceans (Figure 4.20b) with strong opposing variability in C^{dis} and C^{sat} (Figure 4.20d,a). In the South and tropical Pacific, C^{soft} drives most of the variability with modest contributions from C^{sat}, and C^{carb} near the Southern Ocean. Extratropical Indian Ocean multidecadal DIC varability is driven purely by anthropogenic carbon, Figure 4.20e. In the Southern Ocean, moderate C^{sat} and C^{dis} anomalies drive multidecadal variability (Figure 4.20a, d) that are partly damped by counteracting C^{soft} anomalies (Figure 4.20b).

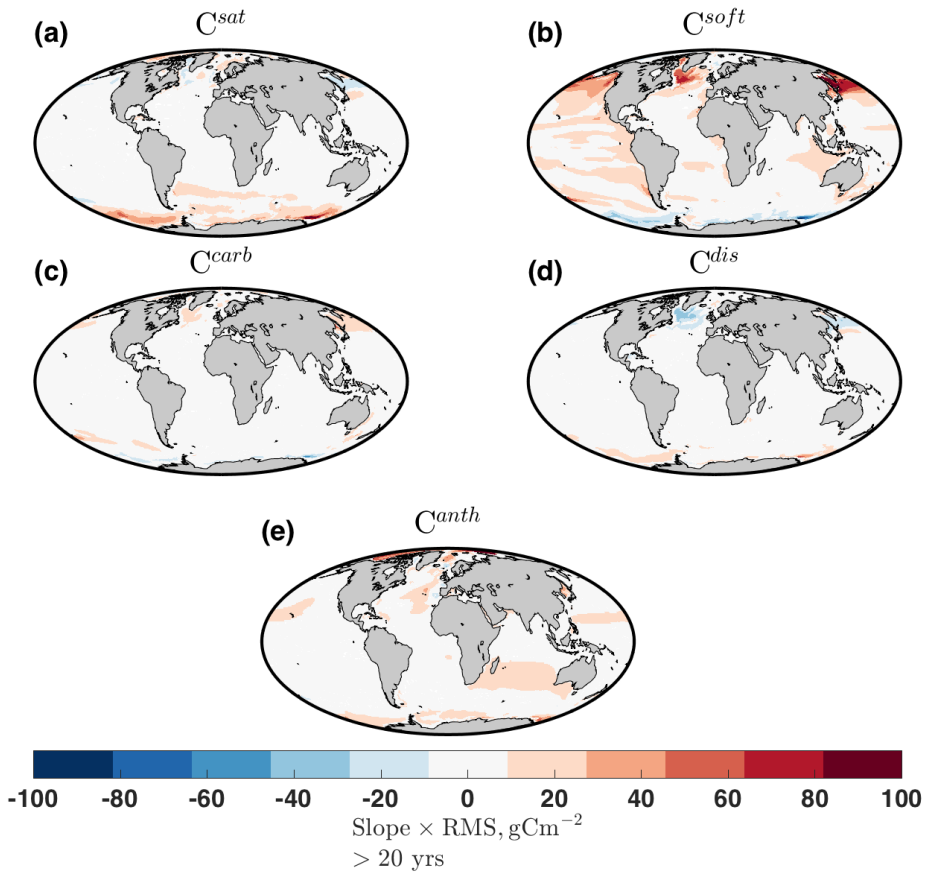

Figure 4.20: Impact of DIC components shown as slope of regression line between component and total DIC inventory anomalies scaled by RMS(C′) for multidecadal (>20 year) variability, gCm^{-2}

4.4.5 Long Term Trend

The long term response of the global ocean to anthropogenic carbon emissions by the end of the 21st Century is to store large amounts of DIC everywhere, with the largest DIC anomalies per unit area in the southern Indian Ocean and North Atlantic. Across most of the ocean, this is driven by C^{anth}, Figure 4.21e. In the eastern Pacific, subpolar North Atlantic, subpolar North Pacific and Southern Ocean, there are large accumulations of C^{soft}, Figure 4.21b. In the Pacific, this C^{soft} buildup is accompanied by an almost equal reduction in C^{dis} (Figure 4.21d). In the Southern Ocean, the long term C^{soft} increase is mostly offset by declines in saturation and disequilibrium carbon, Figure 4.21a,d. In the tropical Indian Ocean, declines in C^{soft} and C^{dis} incompletely offset some of the C^{anth} accumulation, Figure 4.21b,d.

$$I_t = \int^{global} \mathrm{C}_t \tag{4.6}$$

$$\Delta I = \overline{I_{2090:2099}} - \overline{I_{1860:1869}} \tag{4.7}$$

$$\Delta I^{CC} = \Delta I^{AN} - \Delta I^{CN} \tag{4.8}$$

The bulk global changes in each carbon component due to climate change, are calculated as follows: starting with the annual mean global inventory of each carbon component (I) for any given year (t), equation (4.6), the difference between the mean inventories of the first and last decades (1860 to 1869 and 2090 to 2099 respectively) is found (ΔI), equation (4.7). The inventory change due to climate change (ΔI^{CC}) is calculated as the difference between ΔI for the Anthropogenic (AN) simulation and the Control (CN) simulation, equation (4.8), to account for any drifts in the model.

By the end of the 21$^{\text{st}}$ Century, the global ocean accumulates 399 Pg of anthropogenic carbon. At the same time, the anthropogenic greenhouse gas perturbation drastically alters the Earth's radiative balance and widespread warming occurs. In the ocean, this manifests most prominently as a strengthening of stratification everywhere by the year 2099. The resulting decline in global overturning causes the accumulation of 44.9 Pg of soft tissue carbon. Meanwhile there are decreases in saturation (47.5 PgC), carbonate (7.63 PgC) and disequilibrium (19 PgC) carbon. The saturation carbon decline is due to thermal effects alone is 59.6 PgC, and 2.6 PgC due to salinity effects. Preformed alkalinity changes by the final decade of the 21$^{\text{st}}$ Century increase the global C^{sat} inventory by 10.9 PgC. Note that this partitioning of C^{sat} into three components does not perfectly sum to the total C^{sat} change of -47.5 PgC due to nonlinear interactions between the thermal, salinity and alkalinity effects (see Section 3.4.2 for details on the calculation of components of C^{sat}). Instead these figures provide an estimate of approximate magnitude and sign of the different effects.

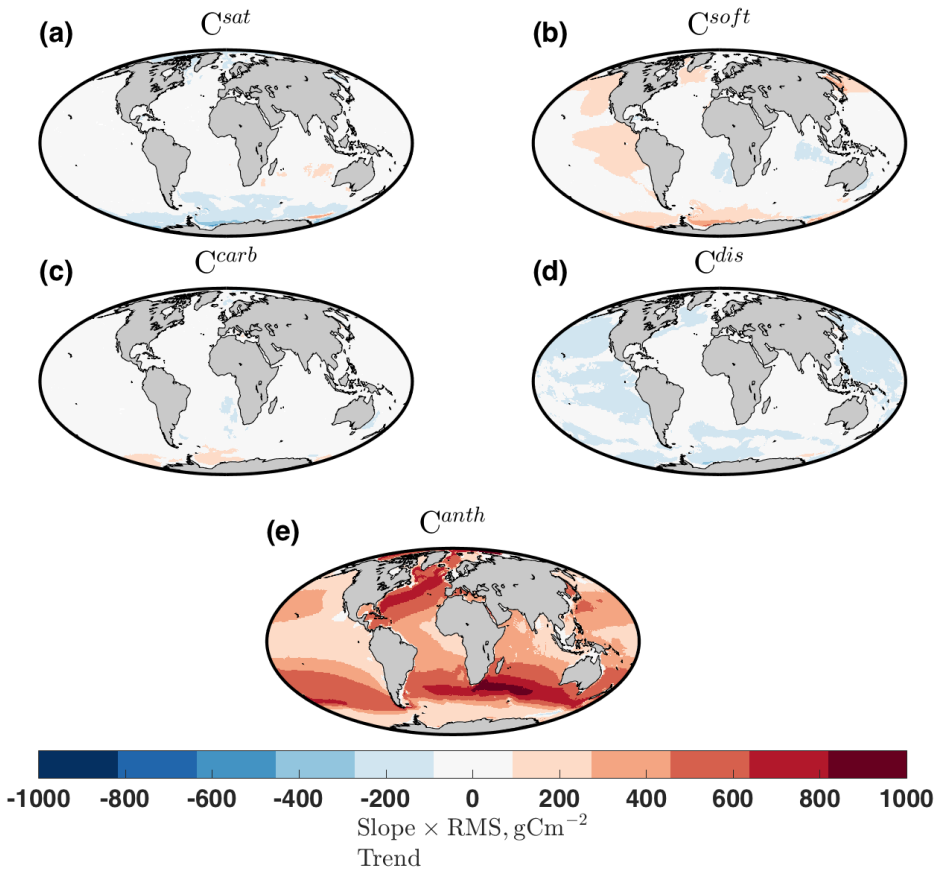

Figure 4.21: Impact of DIC components shown as slope of regression line between component and total DIC inventory anomalies scaled by RMS(C′) for the long term trend, gCm^{-2}

4.4.6 Drivers of C^{soft} Variability

Having established that interannual variability in global DIC fields is driven primarily by Pacific soft tissue carbon variability, it is worth exploring the underlying mechanisms further. The same method is used here as described in Section 3.4.3 to attribute C^{soft} variability to contributions from export production and physical redistribution.

$$\frac{dC^{soft}}{dt} = E_t - (H_t + D_t) \tag{4.9}$$

$$(H_t + D_t) = \frac{dC_t^{soft}}{dt} - E_t \tag{4.10}$$

To briefly recap, this method is performed offline using only information about the export production of C^{soft} (in gC yr^{-1}) and the total C^{soft} inventory of an ocean

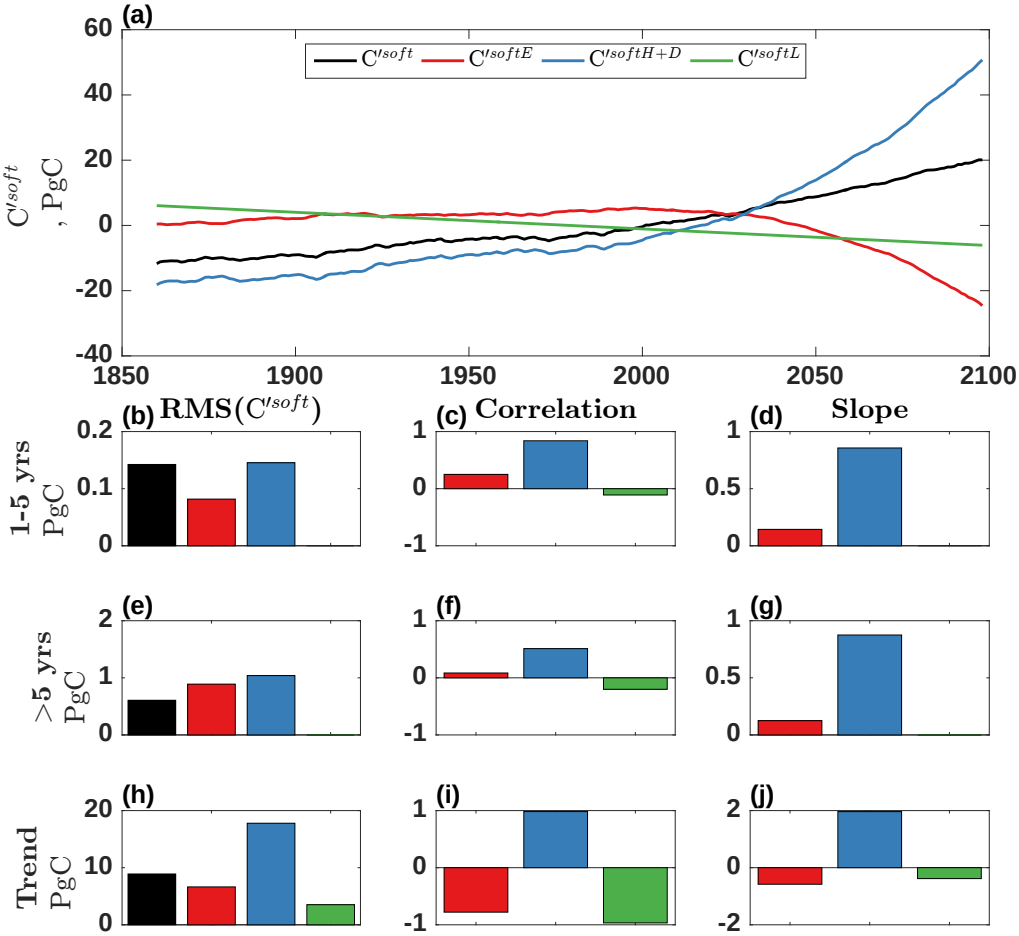

Figure 4.22: Time series of Pacific C'^{soft} with contributions from export production (E), advection plus destruction ($H + D$), and 'leak correction'(L) (a), with descriptive statistics showing the roles of each contribution on different timescales: interannual (1-5 years, b-d), decadal and multidecadal (>5 years, e-g), and the long term trend (h-j). Left: root-mean-square (RMS) of anomalies of C^{soft} inventory (black) and components (colours). Centre: Correlations between component and total C^{soft} inventory anomalies. Right: Slope of regression line between component and total C^{soft} inventory anomalies

basin (in gC) to create a simple budget. In this budget, the 'output' of C^{soft} (in gC yr^{-1}) in a given year can be solved as the difference between the creation of C^{soft} (by export production, E) since the previous year and the change in size of the C^{soft} reservoir since the previous year, equations (4.9) and (4.10). In the global ocean, the 'output' component represents the 'destruction' of C^{soft} by vertical mixing into the surface ocean (D). For any basin of the global ocean, the 'output' component corresponds to the combined effects of the horizontal advection of C^{soft} into/out of

the basin and the 'destruction' of C^{soft} by upward mixing with the surface ocean ($H + D$). By adding the time series of one process (E or $H + D$) to the long term average of the other process from the control (CN) simulation ($\overline{H + D^{CN}}$ or $\overline{E^{CN}}$), time series of anomalies due to each of the two processes can be constructed, C'^{softE} and $C'^{softH+D}$ respectively (Figure 4.22a, red and blue lines).

If the long term averages of export production and advection+destruction components are not equal in the control simulation (i.e. if the control C^{soft} inventory is still drifting), then a third 'leak correction' component (C'^{softL}) arises in this budget equal to the difference between the two processes and of opposite sign. To reiterate, there is no temporal variation in the leak component, and so it only appears in the analysis of the long term trend in C^{soft} (Figure 4.22d,g,j). The model's Pacific C^{soft} budget is still drifting slightly (gaining approximately 0.07 PgC^{soft} yr^{-1}) even after hundreds of years of spin-up, and so the leak component is a small part of the long term trend (Figure 4.22j). The millenia-long spin-up to equilibrate C^{soft} production and destruction was not feasible for this study.

In the Pacific, where interannual and decadal variability in C^{soft} drives much of the global DIC variability, physical redistribution and C^{soft} destruction, rather than biological production, are the key processes. Year-to-year variability in export production only makes small changes in the Pacific C^{soft} budget (Figure 4.22d,g). With this method alone, it is not possible to distinguish between the advection and destruction by vertical mixing components.

At the global scale the only sink of C^{soft} is through upwelling into the surface mixed layer. The Pacific (Figure 4.22b-d) and global (Figure 4.23b-d) C^{soft} variability on interannual timescales is very similar, and so it is plausible that Pacific $C'^{softH+D}$ variability is caused by ventilation rather than advection. In the long term trend, the C^{soft} anomalies due to destruction drastically increase, while anomalies due to export production decline, Figure 4.23a). This means that although the production of C^{soft} (through export production) has decreased, there is a much larger decline in the destruction of C^{soft} via upwelling into the surface ocean. The net result of climate change in a warming world under RCP8.5 on the two opposing effects is growth of the global C^{soft} inventory.

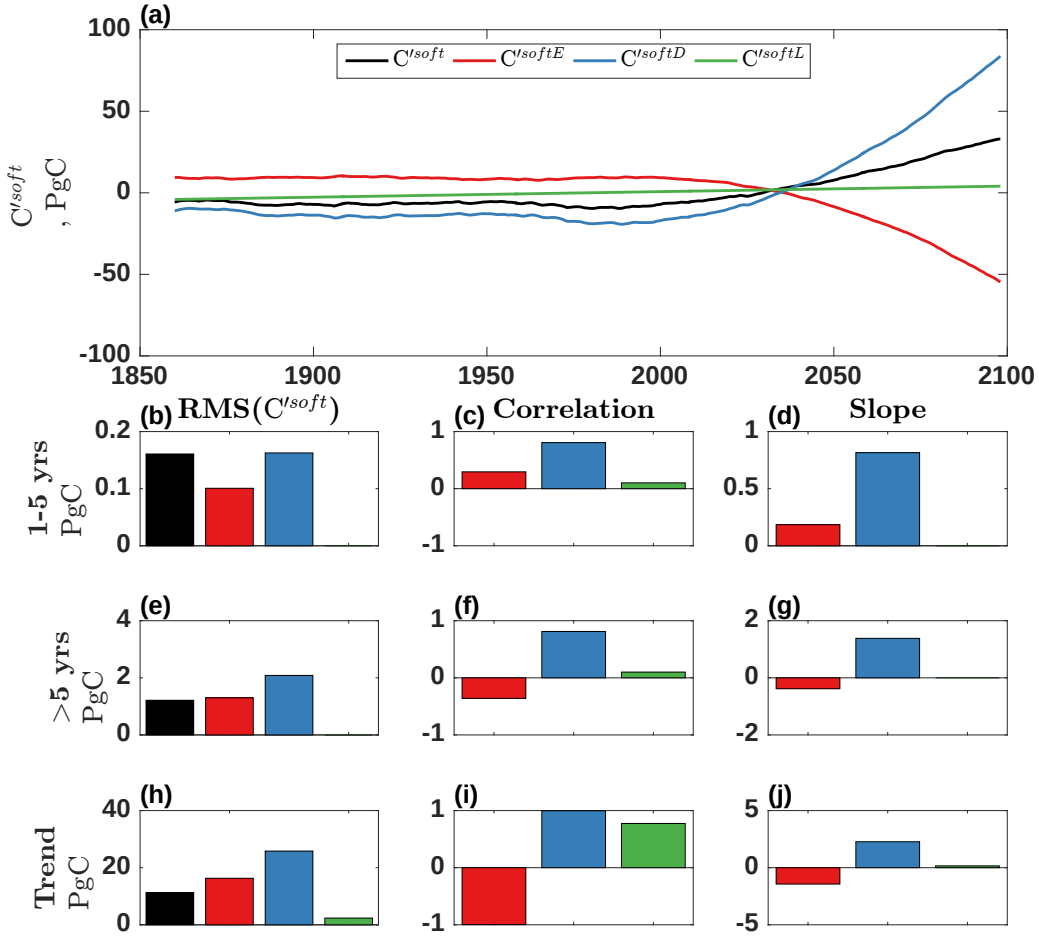

Figure 4.23: Time series of global C'^{soft} with contributions from export production (E), destruction by ventilation (D), and 'leak correction'(L) (a), with descriptive statistics showing the roles of each contribution on different timescales: interannual (1-5 years, b-d), decadal and multidecadal (>5 years, e-g), and the long term trend (h-j). Left: root-mean-square (RMS) of anomalies of C^{soft} inventory (black) and components (colours). Centre: Correlations between component and total C^{soft} inventory anomalies. Right: Slope of regression line between component and total C^{soft} inventory anomalies

4.4.7 Surface DIC Variability

The analysis of DIC inventories up to this point has considered the global integral of inorganic carbon over the full depth of the modelled ocean. This approach accounts for all DIC variability in the entire ocean, and mostly occurs in the upper 2000 m. However, the air-sea gas flux of carbon dioxide is a process necessarily focused on the ocean surface, and so it is also relevant to examine DIC variability

in the uppermost layer of the oceans. Therefore, instead of summing the ocean's inventory of DIC through the entire depth, the same analysis can also be performed on just the surface 6 m layer of the model.

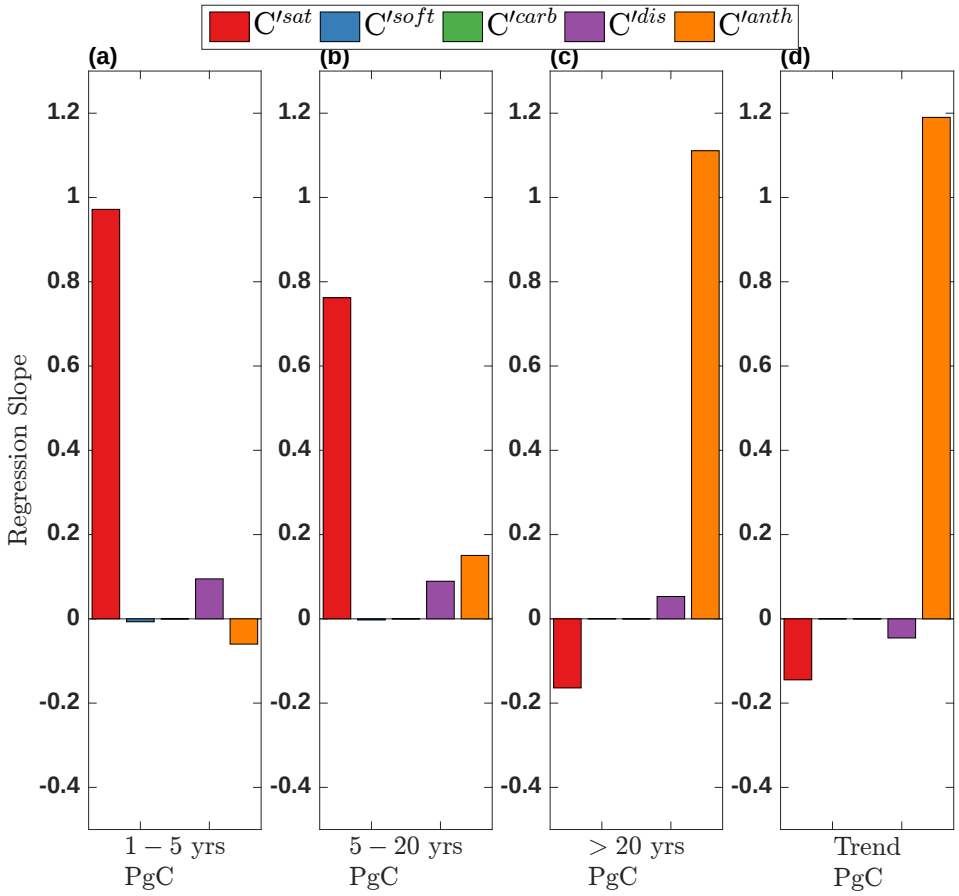

Figure 4.24: Strength of different components of DIC in controlling variability on different timescales, expressed as the slope of regression line between component and total DIC inventory anomalies in only the surface 6m layer of the global ocean for four different timescales of variability, (a) 1-5 year interannual, (b) 5-20 year decadal, (c) >20 year multidecadal, and (d) the long term trend

DIC variability in the surface 6 m strongly contrasts that of the entire oceans, and consists mainly of saturation and anthropogenic carbon variance, Figure 4.24. On interannual timescales, almost all the variability of the surface layer is driven by saturation, Figure 4.24a. Decadal variability shows small contributions from disquilibrium and anthropogenic components of DIC, however C^{sat} is again the dominant driver, Figure 4.24b. On multidecadal timescales and over the long term trend, anthropogenic carbon is the unsurprising major component, although its effect is partly dampened by opposing saturation variability, Figure 4.24c,d.

This analysis indicates that the biological pump is therefore a weak driver of DIC

variability on all timescales in the surface 6 m. This is because the configuration of regenerated C^{soft} and C^{carb} tracers (DIN^{reg} and A_T^{reg} respectively) are relaxed towards 0 in the upper 62 m of the ocean (see Section 3.2.1). Any deviations of DIC away from saturation with a preindustrial atmosphere that are not due to anthropogenic carbon are then shifted from C^{soft} and C^{carb} into the disequilibrium pool, C^{dis}. Given that C^{soft} is the critical driver of global DIC variability, one might expect that the ventilation of C^{soft} into the mixed layer would impart appreciable C^{dis} anomalies into the uppermost 6 m of the ocean but small regression slopes of C^{dis} anomalies indicate that this is not the case, Figure 4.24. Instead, a plausible explanation is that CO_2 fluxes effectively eliminate DIC disequilibria in the surface 6 m.

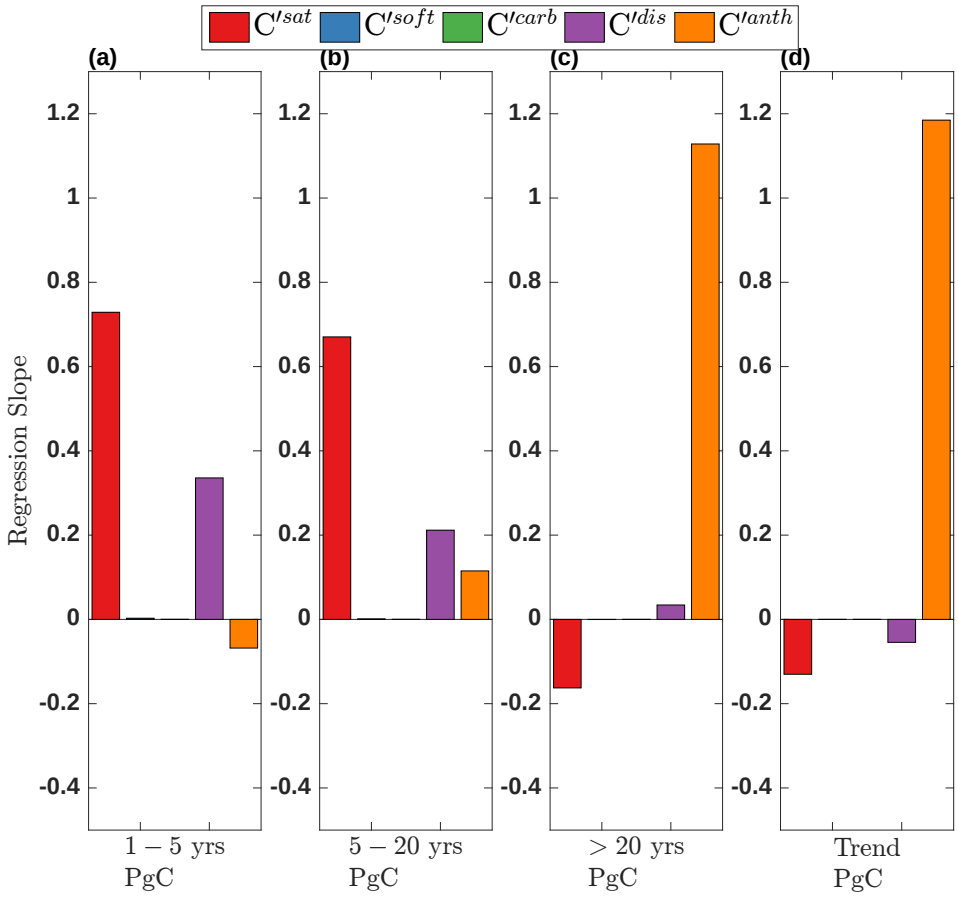

Figure 4.25: Strength of different components of DIC in controlling variability on different timescales, expressed as the slope of regression line between component and total DIC inventory anomalies in only the surface 62m layer of the global ocean for four different timescales of variability, (a) 1-5 year interannual, (b) 5-20 year decadal, (c) >20 year multidecadal, and (d) the long term trend

If a thicker surface layer is chosen (62 m), then C^{dis} emerges as a much more

important component of upper ocean DIC variability on interannual and decadal timescales, Figure 4.25a,b. However, interannual and decadal DIC variability in the upper ocean are still dominated by changes saturation rather than disequilibrium concentrations. This result contrasts the analysis of the entire ocean domain, where saturation carbon variability is minor. This analysis of multidecadal variability and long term trends is not highly sensitive to the choice of depth chosen, as these timescales are always dominated by C^{anth} with minor compensation from the other components, Figure 4.25c,d.

4.5 Discussion

The previous chapter identified variability in the saturation concentration of DIC as the main driver of the interannual variability of the North Atlantic inorganic carbon inventory. That finding led to the hypothesis that saturation is the dominant driver of interannual global DIC variability. The work described in this chapter refutes this hypothesis, identifying that Pacific Ocean hosts large interannual variability of soft tissue carbon that sets the global pattern. In particular, advection and vertical transport drive C^{soft} variability more strongly than variance in export production. The North Atlantic's strongly saturation-driven interannual variability, while important at the basin scale, is found to be a lower-order contributor to global interannual DIC variability. The processes that control decadal and multidecadal DIC variability are distinct from those operating on interannual timescales. Anthropogenic carbon uptake is instrumental in setting global variability on decadal and multidecadal timescales, and to the end of the 21st Century. Saturation and disequilibrium variability on decadal and longer timescales tends to oppose the action of C^{soft} and the degree of this incomplete compensation is what sets the natural carbon cycle variability under climate change.

Variability in carbon concentrations in the upper ocean are of first order importance in governing the global marine flux of CO_2 (*Doney et al.*, 2009; *Landschützer et al.*, 2016). Here, the importance of the Pacific is highlighted for its control of interannual variability of oceanic inorganic carbon content. In the tropical and eastern Pacific, large variability in soft tissue carbon is responsible for driving much of

the total variability of the total global DIC inventory. The equatorial Pacific hosts the ENSO phenomenon, where interannual variations in easterly tropical winds cause large swings in local upwelling. Interannual variability of Pacific upwelling affects C^{soft} in two opposing ways: 1) by modulating the supply of nutrients to surface, which subsequently controls primary production and export production of C^{soft}, and 2) by varying the destruction of C^{soft} through the upwelling of deep waters rich in remineralised carbon to the surface. In the Pacific, the effect of upwelling in bringing C^{soft}-rich waters to the surface is greater than its effect on export production. In addition, the Pacific hosts intense DIC variability North of where the Kuroshio current separates from the Japanese coast. Here, variations in the western boundary current extension modulate the upwelling of C^{soft}, as well as saturation carbon and DIC disequilibria to a lesser extent. These findings suggest that a detailed understanding of these Pacific regions is key to constraining global interannual DIC variability.

The GLODAPv2 database is crucially lacking in repeat hydrography with biogeochemistry for the Pacific Ocean. In both sections identified, only two years of data may be compared. Given that models indicate that the Pacific is likely to be an important location for interannual and decadal carbon cycle variability (*Doney et al.*, 2009; *Long et al.*, 2013), this paucity of data represents a major limitation for the scientific community's ability to validate ocean carbon cycle models. In general, most of the important variability in the Pacific is likely to be located in the tropics which are poorly represented in the observations (*Key et al.*, 2015; *Olsen et al.*, 2016).

Although moored sensors and fixed point observatory timeseries exist (*Sutton et al.*, 2014, 2017), the Pacific Ocean is crucially lacking both surface and interior carbon observations (*Ishii et al.*, 2014; *Bakker et al.*, 2016; *Olsen et al.*, 2016; *Key et al.*, 2015) necessary to constrain interannual DIC variability. In particular, mooring data from four Pacific sites show reduced CO_2 uptake over 10 years from 2004-2014 due to warm anomalies in the later years. In the model, these locations' DIC interannual variability is controlled by C^{sat} and C^{soft} and lie further north than the highly variable C^{soft}-driven tropical Pacific. While the long time series locations discussed by *Sutton et al.* (2017) may be representative of the subtropical

North Pacific, these do not capture the crucial equatorial Pacific C^{soft} variability that is identified here.

Much of the scientific understanding of the Pacific as a driver of interannual carbon flux variability stems from either numerical models or interpolated pCO_2 mapping studies. In all cases there is a consensus that the tropical and eastern Pacific underlies this variability (*McKinley et al.*, 2017). This work highlights that soft tissue carbon is the critical DIC component that drives Pacific CO_2 flux variability, but a detailed understanding of the global soft tissue pump is still lacking. While this study finds that interior redistribution and ventilation of soft tissue carbon rather than export production drives Pacific DIC variability, there is nevertheless a pressing need to ensure that ocean simulations are able to correctly model the biological pump because this is the original source of C^{soft}. Authors highlight that gaps in a mechanistic understanding of the soft tissue pump limit the ability of models to correctly predict future changes, particularly requiring more complex consideration of heterotropic processes (*Sanders et al.*, 2014; *Cavan et al.*, 2017). In another vein, models show disagreement on the sign of primary productivity changes in response to a warming ocean (e.g. *Taucher and Oschlies*, 2011). These fundamental gaps in our understanding of the biological pump leave crucial weaknesses in biogeochemical models. Until ocean models can produce soft tissue carbon confidently there will be critical uncertainties in the future evolution of the ocean carbon sink.

From an observation perspective, studies that leverage mapped pCO_2 products to quantify CO_2 flux variability also may not be responding to the processes that numerical models suggest are important. In regions like the Pacific, observations of surface pCO_2, interior DIC and the soft tissue pump are relatively scarce, and are likely insufficient to confidently constrain interannual variability (*Takahashi et al.*, 2014; *Wanninkhof*, 2014; *McKinley et al.*, 2017). Through one method or another, pCO_2 mapping techniques such as Multilinear Regression or neural networks must be trained on regularly and densely sampled predictor variable to estimate sparsely sampled pCO_2 fields (*Rödenbeck et al.*, 2013; *Landschützer et al.*, 2014; *Rödenbeck et al.*, 2015). In a simple example, *Wang et al.* (2015) discuss how subannual and interannual pCO_2 - SST relationships can differ, making empirical estimation

of pCO_2 on better sampled oceanographic parameters problematic. While these approaches clearly make the best use of the limited data presently available, modelling studies (including this one) highlight that processes (such as soft tissue carbon cycling) that are not well-observed appear to be important. While those processes remain incompletely constrained in observations, then data-based approaches to estimating carbon flux variability (as with modelling approaches) will still be critically uncertain.

The role of ENSO in driving global interannual variability is consistently highlighted in the literature (*Doney et al.*, 2009; *Park et al.*, 2010; *Rödenbeck et al.*, 2014; *Ishii et al.*, 2014; *Wang et al.*, 2015; *Landschützer et al.*, 2016). An atmospherically forced ocean-only simulation lacks the ocean-atmosphere feedbacks that underlie ENSO. A detailed validation of ENSO is not attempted here, but other work highlights that HadGEM2 simulations (which provided the atmospheric forcing for this study) show relatively good ENSO characteristics in spite of errors in the underlying feedbacks (*Bellenger et al.*, 2014). A common model error is an underestimation of ENSO amplitude owing to underestimation of upwelling (*Dong et al.*, 2017). The potential for a low bias in tropical upwelling therefore does not likely detract from the main finding of this work that the tropical Pacific C^{soft} is central to global DIC inventory variability in this model.

While this study is primarily concerned with investigating the entire ocean DIC pool, it is worth examining the variability right at the surface. In the surface 6 m, interannual and decadal DIC variability is attributable almost entirely to the saturation component. When integrated over the surface 62 m, the role of carbon disequilibria on interannual and decadal timescales become considerable, although still much smaller than saturation. Given that the air-sea carbon flux is an inherently surface-focused process, this evidence suggests that the DIC variability potentially most relevant to carbon fluxes is most strongly controlled by saturation. This result suggests that the roles of drivers of DIC variability are somewhat sensitive to the domain chosen, and warrents further investigation in the context of CO_2 fluxes. A more in-depth exploration of this result is not attempted here, but is discussed further in Section 5.2.

4.6 Conclusions

Here, the variability of the global ocean pool of dissolved inorganic carbon has been decomposed into different timescales; interannual, decadal, multidecadal and the long term trend running up to the year 2100. The contributions of saturation, the soft tissue pump, the carbonate pump, disequilibria and anthropogenic emissions to global DIC variability were identified. Global DIC interannual variability is driven chiefly by the upwelling of soft tissue carbon, C^{soft}, in the eastern and equatorial Pacific. The Pacific also hosts widespread, strong decadal variability in C^{soft}, but contributions from other basins and DIC components are important in setting the global pattern. Particularly, decadal and multidecadal variability in the invasion of anthropogenic carbon into the extratropical oceans (especially the Arctic) sets the global pattern. The 'natural' (i.e. non-anthropogenic) carbon cycle's decadal and multidecadal variability is characterised by incomplete compensation of soft tissue carbon against saturation and disequilibrium anomalies, and is small compared to the leading-order role of anthropogenic carbon. The carbon added to the deep ocean by the dissolution of sinking calcium carbonate, C^{carb}, is always a small contributor to global DIC variability. By the end of the 21st Century, the global ocean accumulates 400 Pg of anthropogenic carbon. At the same time, the natural carbon pools respond to climate change with a net decline of 30 PgC. The decrease of the saturation, carbonate and disequilibrium pools is incompletely offset by the accumulation of 48.5 PgC^{soft} through strengthening stratification.

Chapter 5

Conclusion

5.1 Review of Results

The broad aim of this thesis was to undertake a detailed examination of the mechanisms that give rise to variability in the ocean carbon sink. Since the global ocean is a major, variable sink of CO_2 for the atmosphere, it plays a key role in regulating the planetary radiation balance, and therefore climate. A knowledge of the variability of ocean carbon uptake is necessary to understand how future climate may change as a result of anthropogenic changes to Earth's greenhouse effect. More precisely, an assessment of the contributions of processes giving rise to carbon sink variability in the present and future ocean under climate change is needed to understand how future climate change may unfold. Moreover, the diversity of mechanisms that modulate the ocean carbon sink gives rise to variability on a spectrum of timescales. Therefore, the main aim of this work was to identify specifically which processes cause ocean carbon sink variablity on different timescales over recent decades up to the end of the 21st Century.

First, the drivers of North Atlantic CO_2 gas flux variability were investigated in a model simulation under strongly rising atmospheric greenhouse gas concentrations from the year 1860 to 2099 CE. This study distinguished the roles of the three components of the air-sea gas flux equation: the interfacial CO_2 concentration gradient, the gas transfer velocity, and the solubility coefficient. In the North Atlantic, both the air-sea pCO_2 gradient and gas transfer velocity contribute importantly to interannual variability of gas exchange. This shorter period variability

contrasts the longer, multiannual and decadal gas flux variability, which is dominated by the air-sea pCO_2 gradient contribution alone. As a consequence, it is possible to estimate multiannual North Atlantic CO_2 gas flux variability without well constrained estimates of fluctuations in the gas transfer velocity.

Having established the importance of oceanic pCO_2 variability in controlling North Atlantic carbon dioxide uptake, the drivers of changes in the basin's carbon content were explored. Fields of North Atlantic dissolved inorganic carbon were decomposed into contributions from solubility, the soft tissue pump, the carbonate pump, disequilibria, and anthropogenic activities using a model simulation of the global ocean experiencing climate change due to rapidly increasing greenhouse gas concentrations from the year 1860 to 2099. Interannual variability in North Atlantic DIC results almost entirely from changes in the saturation concentration of inorganic carbon. These saturation changes are caused mostly by temperature and secondarily by preformed alkalinity variance, while salinity makes effectively negligible contributions. Decadal variability in the basin is driven by both saturation and anthropogenic carbon components. The saturation component of decadal DIC is mostly thermally driven, but preformed alkalinity also plays an important role. Multidecadal variability is driven mostly by AMOC strength modulating the uptake of anthropogenic carbon, while also causing large, opposing swings in saturation and soft tissue carbon almost completely compensate each other. The long term DIC trend between 1860 and 2099 is driven almost entirely by the accumulation of anthropogenic carbon, which dwarfs the changes in the natural carbon pools up to the end of the 21st Century.

The third chapter of research expands upon the first and second, and explores the drivers of variability in the global ocean DIC pool. Using the same simulation of the global ocean's response to sharply increasing atmospheric greenhouse gas content in the 240 years leading up to the year 2100, the oceanic carbon content was partitioned in terms of components from saturation, the soft tissue and carbonate pumps, disequilibria and anthropogenic carbon. Global interannual DIC variability in the equatorial and eastern Pacific sets the global variance. Year-to-year differences in the upwelling of deep waters rich in soft tissue carbon into the surface ocean Pacific is the key mechanism driving global DIC variability. The

contribution of interannual variability in the production of soft tissue carbon by the Pacific ecosystem is found to be small in comparison with the much larger role of physical redistribution. Disequilibrium carbon variability in the Pacific also forms an important, but smaller component of total interannual DIC variability. This global result strongly contrasts that of the North Atlantic described in the previous chapter, where temperature and preformed alkalinity variability underpins interannual changes in the basin's DIC stock. The global decadal variability in DIC content stems from the anthropogenic component. On multidecadal timescales, anthropogenic carbon uptake variability is also the main driver of the global pattern, while multidecadal saturation and soft tissue carbon fluctuations mostly compensate eachother. The main response of the global ocean to human carbon emissions by the year 2100 is the accumulation of hundreds of petagrams of anthropogenic carbon. This additional carbon is much larger than the changes to the natural ocean carbon pools that result from climate change by the end of the century.

5.2 Further Outlook

Although this thesis identifies key processes that drive ocean carbon cycle variability to first order, there are still details about those underlying mechanisms which remain to be explored. For example, the boundary regions of the Kuroshio extension and North Atlantic current inter-gyre boundary appear to be sites that drive ocean carbon cycle variance, and so a focused analysis of these western boundary current separation regions is still needed. A detailed analysis of the role of western boundary current dynamics would benefit from a simulation of much higher resolution than the nominal 1-by-1° setup used here. Furthermore, a more in-depth attribution of carbon cycle variability to specific physical processes would be a salient next step. For example, models can be configured to provide much more detailed diagnostics of the roles of advection, mixing, convection, and other processes in controlling tracer budgets (e.g. *Butler et al.*, 2013; *Lauderdale et al.*, 2016).

The choice of modelling approach used in this work was largely driven by the

practicality and ease of deployment. An uncoupled ocean model is a particularly useful tool to quickly identify the response of the ocean to recent atmospheric variability or future climate change, but lacks realistic feedback dynamics. The main value of this work lies in its identification of drivers of ocean carbon cycle variability that should ideally be followed up with further study using different tools. In particular, a coupled atmosphere-ocean model, and ocean models forced with observations would be useful to expand on the findings identified here. With different model approaches, it would be possible to explore, for example, the roles of ocean-atmosphere feedbacks, or to attribute specific, observed carbon cycle variability events to underlying mechanisms. This work has highlighted the importance of the Pacific equatorial upwelling for global DIC variability, and so it is clear that further, dedicated study to examine the ocean-atmosphere phenomenon (particularly using a coupled model) would be very enlightening.

The subduction and upwelling of carbon disequilibria was identified as a second-order component of global and regional DIC variability. While DIC disequilibria never appear as a main driver of variability at the largest scales, they nevertheless plays an important role in setting the global ocean carbon sink, especially on interannual timescales and in the long term trend to the end of the 21^{st}C. While the role of C^{dis} in the context of North Atlantic and global ocean carbon variability was identified, the drivers of this component remain unexplored. Efforts are already being made to develop a more detailed understanding of disequilibrium carbon; mixed layer depth and wind speed are key controlling factors (*Jones et al.*, 2014). Furthermore, this thesis found the contribution of C^{dis} to overall North Atlantic DIC inventory variability to be small, and yet *Jones et al.* (2014) highlight the north of the basin as a hotspot for the formation of disequilibria. Future investigation into the role and drivers of C^{dis} will likely require the use of numerical simulation, and so due care should be taken to ensure model setup is appropriate. The model setup used for this study lacks coupled ocean-atmospheric feedback, and spatiotemporal variability (other than a long term increase) in atmospheric pCO_2 concentration, and therefore may not be well suited to study the disequilibrium carbon component in detail.

Two of the main results that emerged from this thesis suggest that the estimation

of the variability of the North Atlantic carbon sink could be approximated without a detailed knowledge of the underlying carbonate chemistry. In the first research chapter and (*Couldrey et al.*, 2016), it was demonstrated that carbon dioxide fluxes can be reasonably estimated using only information about $p\mathrm{CO}_2$ variability, since the gas transfer velocity contribution is often small. In the second research chapter, saturation dynamics were found to be the leading order control on North Atlantic DIC variability on interannual timescales. The third research chapter finds that while Pacific C^{soft} is the dominant driver of global interannual DIC variability, the surface ocean is much more responsive to saturation changes than the full depth. Other work finds that DIC inventory variability is the leading driver of interannual changes in surface ocean $p\mathrm{CO}_2$ in the North Atlantic (*Thomas et al.*, 2008; *Doney et al.*, 2009). All of these results indicate that it could be possible to approximate surface CO_2 flux variability in the North Atlantic using well sampled oceanographic parameters: monthly mean fields of surface ocean temperature and salinity, climatological surface alkalinity and monthly mean fields of ocean surface winds. The saturation DIC concentration is calculated using the temperature and salinity of a water parcel, an estimated preformed alkalinity (based on its salinity) and a fixed preindustrial atmospheric $p\mathrm{CO}_2$. This saturation concentration could then be used in the CO_2 flux equation to work out a 'saturation flux'. Fields of this saturation flux could be compared against observation-derived carbon flux fields such as those described by *Landschützer et al.* (2016) and *Rödenbeck et al.* (2014). Such a comparison would provide information about what amount of flux variability is driven by saturation processes, independent of the formulation of underlying neural networks or models. *Jones et al.* (2014) highlight how one can derive observation based estimates of ocean carbon disequilibria, which occur when CO_2 fluxes cannot fully eliminate air-sea gradients of $p\mathrm{CO}_2$. One could using information such as the equilibration efficiency parameters described by *Jones et al.* (2014) to identify where saturation fluxes are likely to be similar to the actual flux. Such work would not provide a comprehensive analysis of carbon flux variability, but would nonetheless provide insight using readily available observations and methods.

Chapter 6

Appendix

6.1 Alternative gas transfer velocity parameterisations

Supplementary materials to the work described in Chapter 2 and in (*Couldrey et al.*, 2016):

This appendix contains some additional investigation into alternative gas transfer velocities and the model output used in this work (attached separately). We calculated critical timescales (Figure 6.1) using different gas transfer parameterizations (Figure 6.2) and offline model output, rather than running new simulations. Although this approach means that calculated critical timescales are not directly comparable with those in the main manuscript, we find that these results are qualitatively consistent with our main findings.

To investigate the sensitivity of the critical timescale of ΔpCO_2 dominance on flux variability to the choice of gas transfer parameterization, we recalculated its value using alternative functions (Figure 6.1). To do this thoroughly, it would be necessary to run additional simulations, each with a different k. Since this is not possible within the scope of this work, we instead calculated k using offline wind speeds. This will introduce some error, since the ocean's DIC field will not accurately respond to the differences in CO_2 flux imparted by the use of a different k than that with which the model was run. As a result, this is not directly comparable with the analysis shown in the main manuscript, but it nevertheless indicates that the result is qualitatively similar. The other parameterizations chosen were

selected on the basis that they were functionally distinct from the one used in our model (*Nightingale et al.*, 2000) and commonly used: (*Wanninkhof*, 2014), (*Weiss et al.*, 2007), (*Sweeney et al.*, 2007) and (*McGillis et al.*, 2001) (shown in Figure 6.2). Broadly, the spatial structures of all five are quite similar, and there is good agreement between timescales, no matter which parameterization is used (Figure 6.1). The main difference that the choice of parameterization makes is in the magnitude of the critical timescale when the timescale is large, making the highs higher, especially when the (*McGillis et al.*, 2001) equation is used.

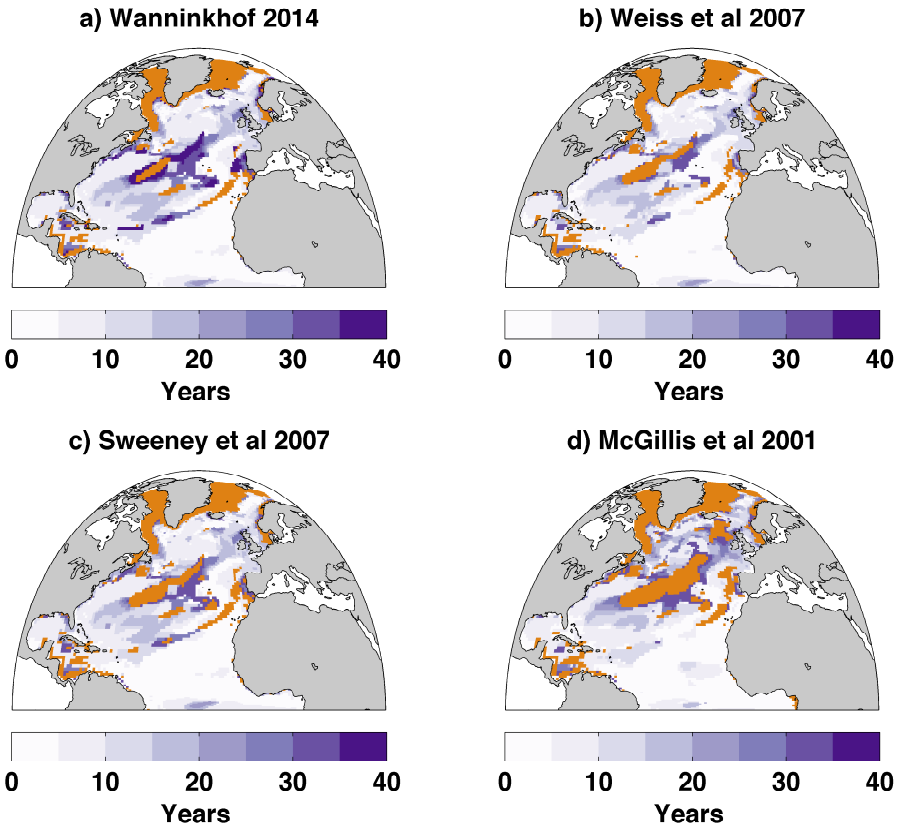

Figure 6.1: Critical timescale of flux variability (purple colors) calculated using four alternative gas transfer velocities: (*Wanninkhof*, 2014), (*Weiss et al.*, 2007), (*Sweeney et al.*, 2007) and (*McGillis et al.*, 2001). Orange: areas where k variability is important on all timescales. Compare with Figure 2.8 in the main manuscript

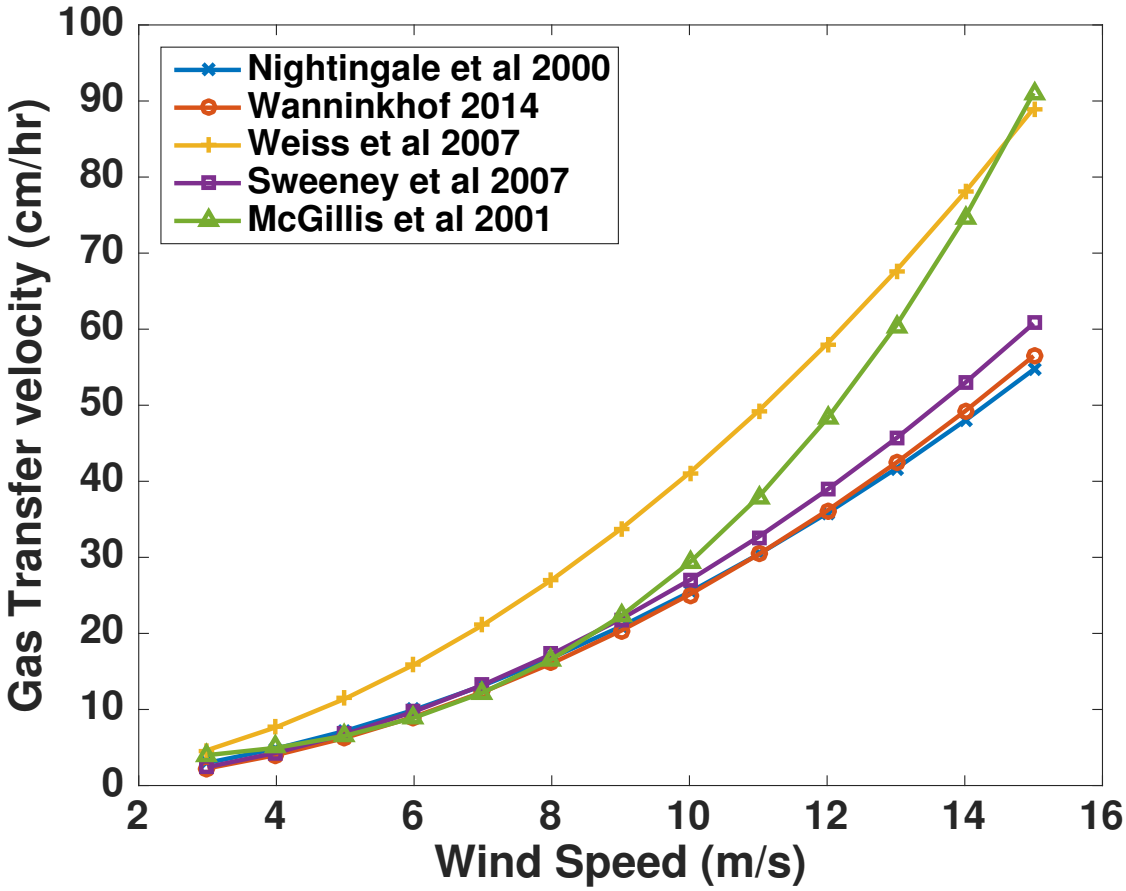

Figure 6.2: Relationships between wind speed and gas transfer velocity (k) for the parameterizations shown in Figure 6.1 and the one used in the main simulations (*Nightingale et al.*, 2000)

Bibliography

Alvarez, M., F. F. Perez, D. R. Shoosmith, and H. L. Bryden, Unaccounted role of Mediterranean Water in the drawdown of anthropogenic carbon, *Journal of Geophysical Research: Oceans*, *110*(C9), 2005.

Anderson, L. A., On the hydrogen and oxygen content of marine phytoplankton, *Deep Sea Research Part I: Oceanographic Research Papers*, *42*(9), 1675–1680, 1995.

Antonov, J., D. Seidov, T. Boyer, R. Locarnini, A. Mishonov, H. Garcia, O. Baranova, M. Zweng, and D. Johnson, *World Ocean Atlas 2009, vol. 2: Salinity, in NOAA Atlas NESDIS 69*, vol. 69, p. 184, US Government Printing Office, 2010.

Archer, D., and V. Brovkin, The millennial atmospheric lifetime of anthropogenic CO_2, *Climatic Change*, *90*(3), 283–297, 2008.

Archer, D., H. Kheshgi, and E. Maier-Reimer, Dynamics of fossil fuel CO_2 neutralization by marine $CaCO_3$, *Global Biogeochemical Cycles*, *12*(2), 259–276, 1998.

Arrhenius, S., XXXI. On the influence of carbonic acid in the air upon the temperature of the ground, *The London, Edinburgh, and Dublin Philosophical Magazine and Journal of Science*, *41*(251), 237–276, 1896.

Arrieta, J. M., E. Mayol, R. L. Hansman, G. J. Herndl, T. Dittmar, and C. M. Duarte, Dilution limits dissolved organic carbon utilization in the deep ocean, *Science*, *348*(6232), 331–333, 2015.

Arruda, R., P. H. Calil, A. A. Bianchi, S. C. Doney, N. Gruber, I. Lima, and G. Turi, Air-sea CO_2 fluxes and the controls on ocean surface pCO_2 seasonal variability in the coastal and open-ocean southwestern Atlantic Ocean: a modeling study, *Biogeosciences*, *12*(19), 5793–5809, 2015.

Atlas, R., R. N. Hoffman, J. Ardizzone, S. M. Leidner, J. C. Jusem, D. K. Smith, and D. Gombos, A cross-calibrated, multiplatform ocean surface wind velocity product for meteorological and oceanographic applications, *Bulletin of the American Meteorological Society*, *92*(2), 157–174, 2011.

Bakker, D. C. E., et al., An update to the Surface Ocean CO_2 Atlas (SOCAT version 2), *Earth System Science Data*, *6*, 69–90, 2014.

Bakker, D. C. E., et al., A multi-decade record of high-quality fCO_2 data in version 3 of the Surface Ocean CO_2 Atlas (SOCAT), *Earth System Science Data*, *8*(2), 383–413, 2016.

Bates, N., et al., A time-series view of changing ocean chemistry due to ocean uptake of anthropogenic CO_2 and ocean acidification, *Oceanography*, *27*(1), 126–141, 2014.

Bates, N. R., Interannual variability of the oceanic CO_2 sink in the subtropical gyre of the North Atlantic Ocean over the last 2 decades, *Journal of Geophysical Research*, *112*(C9), C09,013, 2007.

Bellenger, H., E. Guilyardi, J. Leloup, M. Lengaigne, and J. Vialard, ENSO representation in climate models: from CMIP3 to CMIP5, *Climate Dynamics*, *42*(7-8), 1999–2018, 2014.

Bender, M. L., S. Kinter, N. Cassar, and R. Wanninkhof, Evaluating gas transfer velocity parameterizations using upper ocean radon distributions, *Journal of Geophysical Research: Oceans (1978–2012)*, *116*(C2), 2011.

Bernardello, R., I. Marinov, J. B. Palter, J. L. Sarmiento, E. D. Galbraith, and R. D. Slater, Response of the ocean natural carbon storage to projected twenty-first-century climate change, *Journal of Climate*, *27*(5), 2033–2053, 2014.

Berner, R. A., The long-term carbon cycle, fossil fuels and atmospheric composition, *Nature*, *426*(6964), 323–326, 2003.

Böning, C. W., E. Behrens, A. Biastoch, K. Getzlaff, and J. L. Bamber, Emerging impact of Greenland meltwater on deepwater formation in the North Atlantic Ocean, *Nature Geoscience*, *9*(7), 523–527, 2016.

Brewer, P. G., Direct observation of the oceanic CO_2 increase, *Geophysical Research Letters*, *5*(12), 997–1000, 1978.

Broecker, W. S., and T.-H. Peng, Gas exchange rates between air and sea, *Tellus*, *26*(1-2), 21–35, 1974.

Buesseler, K. O., and P. W. Boyd, Shedding light on processes that control particle export and flux attenuation in the twilight zone of the open ocean, *Limnology and Oceanography*, *54*(4), 1210–1232, 2009.

Butler, E., K. Oliver, J. M. Gregory, and R. Tailleux, The ocean's gravitational potential energy budget in a coupled climate model, *Geophysical Research Letters*, *40*(20), 5417–5422, 2013.

Cavan, E. L., S. A. Henson, A. Belcher, and R. Sanders, Role of zooplankton in determining the efficiency of the biological carbon pump, *Biogeosciences*, *14*(1), 177–186, 2017.

Chipman, D., T. Takahashi, D. Breger, and S. Sutherland, Carbon Dioxide, Hydrographic, and Chemical Data Obtained During the R/V Meteor Cruise 11/5 in the South Atlantic and Northern Weddell Sea Areas (WOCE sections A-12 and A-21). ORNL/CDIAC-55, NDP-045., *Tech. rep.*, Carbon Dioxide Information Analysis Center, Oak Ridge National Laboratory, U.S. Department of Energy, Oak Ridge, Tennessee, doi:10.3334/CDIAC/otg.ndp045, 1994.

Chung, S.-N., G.-H. Park, K. Lee, R. M. Key, F. J. Millero, R. A. Feely, C. L. Sabine, and P. G. Falkowski, Postindustrial enhancement of aragonite undersaturation in the upper tropical and subtropical Atlantic Ocean: the role of fossil fuel CO_2, *Limnology and oceanography*, *49*(2), 315–321, 2004.

Ciais, P., et al., Carbon and other biogeochemical cycles, in *Climate Change 2013: The Physical Science Basis. Contribution of Working Group I to the Fifth Assessment Report of the Intergovernmental Panel on Climate Change*, edited by T. Stocker, D. Qin, G. Plattner, M. Tignor, S. Allen, J. Boschung, A. Nauels, Y. Xia, B. Bex, and B. e. Midgley, chap. 6, Cambridge University Press, Cambridge, United Kingdom and New York, NY, USA, 2013.

Collins, W., et al., Evaluation of the HadGEM2 model. Meteorological Office Hadley Centre Technical Note 74, *Technical note*, Meteorological Office Hadley Centre, Available online at http://www.metoffice.gov.uk/publications/HCTN/index.html.], 2008.

Collins, W., et al., Development and evaluation of an Earth-System model–HadGEM2, *Geoscientific Model Development*, *4*(4), 1051–1075, 2011.

Couldrey, M. P., K. I. Oliver, A. Yool, P. R. Halloran, and E. P. Achterberg, On which timescales do gas transfer velocities control North Atlantic CO_2 flux variability?, *Global Biogeochemical Cycles*, *30*(5), 787–802, 2016.

Cunningham, S., RRS Discovery Cruise 279, 04 APR - 10 MAY 2004: A transatlantic hydrographic section at 24.5N, pp. 150, *Tech. rep.*, Southampton Oceanography Centre, 2005a.

Cunningham, S., RRS Discovery Cruises 277 (26 MAR - 16 APR 2004) and 278 (19 MAR - 30 MAR 2004): Monitoring the Atlantic Meridional Overturning Circulation at 26.5N, pp. 150, *Tech. rep.*, Southampton Oceanography Centre, Southampton, 2005b.

Denman, K., et al., *Couplings between changes in the climate system and biogeochemistry. In: Climate Change 2007: The Physical Science Basis. Contribution of Working Group I to the Fourth Assessment Report of the Intergovernmental Panel on Climate Change*, 500–587 pp., Cambridge University Press, Cambridge, United Kingdom and New York, NY, USA, 2007.

DeVries, T., M. Holzer, and F. Primeau, Recent increase in oceanic carbon uptake driven by weaker upper-ocean overturning, *Nature*, *542*(7640), 215–218, 2017.

Dickson, A. G., Thermodynamics of the dissociation of boric acid in synthetic seawater from 273.15 to 318.15 K, *Deep Sea Research Part A. Oceanographic Research Papers*, *37*(5), 755–766, 1990.

Dlugokencky, E., and P. P. Tans, Trends in atmospheric carbon dioxide, `ftp://aftp.cmdl.noaa.gov/products/trends/co2/co2_annmean_gl.txt`, 2017.

Doney, S. C., S. Yeager, G. Danabasoglu, W. G. Large, and J. C. McWilliams, Mechanisms governing interannual variability of upper-ocean temperature in a global ocean hindcast simulation, *Journal of Physical Oceanography*, *37*(7), 1918–1938, 2007.

Doney, S. C., I. Lima, R. A. Feely, D. M. Glover, K. Lindsay, N. Mahowald, J. K. Moore, and R. Wanninkhof, Mechanisms governing interannual variability in upper-ocean inorganic carbon system and air–sea CO_2 fluxes: Physical climate and atmospheric dust, *Deep Sea Research Part II: Topical Studies in Oceanography*, *56*(8), 640–655, 2009.

Dong, F., Y. Li, and B. Wang, Assessment of responses of tropical Pacific air-sea CO_2 flux to ENSO in 14 CMIP5 models, *Journal of Climate*, *30*(8595 - 8613), 2017.

Dutkiewicz, S., M. J. Follows, and P. Parekh, Interactions of the iron and phosphorus cycles: A three-dimensional model study, *Global Biogeochemical Cycles*, *19*(1), doi:10.1029/2004GB002342, 2005.

Eldering, A., et al., The Orbiting Carbon Observatory-2: first 18 months of science data products, *Atmospheric Measurement Techniques*, *10*(2), 549–563, 2017.

Emerson, S., and J. Hedges, Processes controlling the organic carbon content of open ocean sediments, *Paleoceanography*, *3*(5), 621–634, 1988.

England, M. H., The age of water and ventilation timescales in a global ocean model, *Journal of Physical Oceanography*, *25*(11), 2756–2777, 1995.

Etminan, M., G. Myhre, E. Highwood, and K. Shine, Radiative forcing of carbon dioxide, methane, and nitrous oxide: A significant revision of the methane radiative forcing, *Geophysical Research Letters*, *43*(24), 2016.

Follows, M. J., R. G. Williams, and J. C. Marshall, The solubility pump of carbon in the subtropical gyre of the North Atlantic, *Journal of Marine Research*, *54*(4), 605–630, 1996.

Frew, N. M., D. M. Glover, E. J. Bock, and S. J. McCue, A new approach to estimation of global air-sea gas transfer velocity fields using dual-frequency altimeter backscatter, *Journal of Geophysical Research: Oceans (1978–2012)*, *112*(C11), 2007.

Garcia, H., R. Locarnini, T. Boyer, J. Antonov, O. Baranova, M. Zweng, and D. Johnson, *World Ocean Atlas 2009, Volume 3: Dissolved Oxygen, Apparent Oxygen Utilization, and Oxygen Saturation, edited by: Levitus S*, p. 344 pp, US Government Printing Office, U.S. Government Printing Office, Washington, D.C., 2010a.

Garcia, H., R. Locarnini, T. Boyer, J. Antonov, M. Zweng, O. Baranova, and D. Johnson, *World Ocean Atlas 2009, Volume 4: Nutrients (phosphate, nitrate, silicate saturation, in: NOAA Atlas NESDIS 71*, p. 398 pp, US Government Printing Office, U.S. Government Printing Office, Washington, D.C., 2010b.

Gent, P. R., and J. C. McWilliams, Isopycnal mixing in ocean circulation models, *Journal of Physical Oceanography*, *20*(1), 150–155, 1990.

Gloersen, P., Nimbus-7 SMMR Polar Gridded Radiances and Sea Ice Concentrations, Version 1, doi:http://dx.doi.org/10.5067/QOZIVYV3V9JP, 2006.

González-Dávila, M., J. M. Santana-Casiano, R. Fine, J. Happell, B. Delille, and S. Speich, Carbonate system in the water masses of the southeast Atlantic sector of the Southern Ocean during February and March 2008, *Biogeosciences*, *8*, 1401–1413, doi:10.5194/bg-8-1401-2011, 2011.

Good, S. A., M. J. Martin, and N. A. Rayner, EN4: Quality controlled ocean temperature and salinity profiles and monthly objective analyses with uncertainty estimates, *Journal of Geophysical Research: Oceans*, *118*(12), 6704–6716, 2013.

Gruber, N., and J. L. Sarmiento, Large-scale biogeochemical-physical interactions in elemental cycles, *The Sea*, *12*, 337–399, 2002.

Halloran, P. R., B. B. B. Booth, C. D. Jones, F. H. Lambert, D. J. McNeall, I. J. Totterdell, and C. Völker, The mechanisms of North Atlantic CO_2 uptake in a large Earth System Model ensemble, *Biogeosciences*, *12*(14), 4497–4508, doi:10.5194/bg-12-4497-2015, 2015.

Hansell, D., and C. Carlson, Dissolved organic matter in the ocean carbon cycle, *Eos*, *96*(15), 8–12, 2015.

Hansell, D. A., Recalcitrant Dissolved Organic Carbon fractions, *Annual Review of Marine Science*, *5*, 421–445, 2013.

Hansell, D. A., C. A. Carlson, D. J. Repeta, and R. Schlitzer, Dissolved organic matter in the ocean: A controversy stimulates new insights, *Oceanography*, *22*(4), 202–211, 2009.

Ho, D. T., R. Wanninkhof, P. Schlosser, D. S. Ullman, D. Hebert, and K. F. Sullivan, Toward a universal relationship between wind speed and gas exchange: Gas transfer velocities measured with 3He/SF6 during the Southern Ocean Gas Exchange Experiment, *Journal of Geophysical Research: Oceans*, *116*(C4), 2011.

Hoppema, M., Weddell Sea is a globally significant contributor to deep-sea sequestration of natural carbon dioxide, *Deep Sea Research Part I: Oceanographic Research Papers*, *51*(9), 1169–1177, 2004.

Houghton, R. A., J. House, J. Pongratz, G. Van Der Werf, R. DeFries, M. Hansen, C. L. Quéré, and N. Ramankutty, Carbon emissions from land use and land-cover change, *Biogeosciences*, *9*(12), 5125–5142, 2012.

Huhn, O., M. Rhein, M. Hoppema, and S. van Heuven, Decline of deep and bottom water ventilation and slowing down of anthropogenic carbon storage in the Weddell Sea, 1984–2011, *Deep Sea Research Part I: Oceanographic Research Papers*, *76*, 66–84, doi:10.1016/j.dsr.2013.01.005, 2013.

Humphreys, M. P., et al., Multidecadal accumulation of anthropogenic and remineralized dissolved inorganic carbon along the Extended Ellett Line in the northeast Atlantic Ocean, *Global Biogeochemical Cycles*, 2016.

Ishii, M., et al., Air-sea CO_2 flux in the Pacific Ocean for the period 1990–2009, *Biogeosciences*, *11*, 709–734, 2014.

Ito, T., and M. J. Follows, Preformed phosphate, soft tissue pump and atmospheric CO_2, *Journal of Marine Research*, *63*(4), 813–839, 2005.

Ito, T., M. Follows, and E. Boyle, Is AOU a good measure of respiration in the oceans?, *Geophysical research letters*, *31*(17), 2004.

Johnson, K., et al., Carbon Dioxide, Hydrographic, and Chemical Data Obtained During the R/V Knorr Cruises in the North Atlantic Ocean on WOCE Sections AR24 (November 2-December 5, 1996) and A24, A20, and A22 (May 30-September 3, 1997), *Tech. rep.*, Oak Ridge National Lab.(ORNL), Oak Ridge, TN (United States), doi:10.3334/CDIAC/otg.ndp082, 2003.

Johnson, K. M., et al., Carbon Dioxide, Hydrographic and Chemical Data Obtained During the Nine R/V Knorr Cruises Comprising the Indian Ocean CO2 Survey (WOCE Sections I8SI9S, I9N, I8NI5E, I3, I5WI4, I7N, I1, I10, and I2; December 1, 1994-January 22, 1996), *ORNL/CDIAC-138, NDP-080, Carbon Dioxide Inf. Anal. Cent., Oak Ridge Natl. Lab., US Dep. of Energy, Oak Ridge, Tenn.*, *10*, doi:10.3334/CDIAC/otg.ndp080, 2002.

Jones, C., et al., The HadGEM2-ES implementation of CMIP5 centennial simulations, *Geoscientific Model Development*, *4*(3), 543–570, 2011.

Jones, D. C., T. Ito, Y. Takano, and W.-C. Hsu, Spatial and seasonal variability of the air-sea equilibration timescale of carbon dioxide, *Global Biogeochemical Cycles*, *28*(11), 1163–1178, 2014.

Jouzel, J., et al., Orbital and millennial Antarctic climate variability over the past 800,000 years, *Science*, *317*(5839), 793–796, 2007.

Keil, R., Anthropogenic forcing of carbonate and organic carbon preservation in marine sediments, *Annual Review of Marine Science*, *9*, 151–172, 2017.

Kent, E. C., S. Fangohr, and D. I. Berry, A comparative assessment of monthly mean wind speed products over the global ocean, *International Journal of Climatology*, *33*(11), 2520–2541, 2013.

Key, R. M., et al., A global ocean carbon climatology: Results from Global Data Analysis Project (GLODAP), *Global Biogeochemical Cycles*, *18*(4), 2004.

Key, R. M., et al., Global Ocean Data Analysis Project, version 2 (GLODAPv2), *ORNL/CDIAC-162, NDP-093*, 2015.

Khatiwala, S., F. Primeau, and T. Hall, Reconstruction of the history of anthropogenic CO_2 concentrations in the ocean, *Nature*, *462*(7271), 346–349, 2009.

Kriest, I., and A. Oschlies, Swept under the carpet: organic matter burial decreases global ocean biogeochemical model sensitivity to remineralization length scale, *Biogeosciences*, *10*(12), 8401, 2013.

Landschützer, P., N. Gruber, D. C. E. Bakker, and U. Schuster, Recent variability of the global ocean carbon sink, *Global Biogeochemical Cycles*, *28*(9), 927–949, 2014.

Landschützer, P., N. Gruber, and D. C. E. Bakker, Decadal variations and trends of the global ocean carbon sink, *Global Biogeochemical Cycles*, *30*(10), 1396–1417, 2016.

Landschützer, P., et al., The reinvigoration of the Southern Ocean carbon sink, *Science*, *349*(6253), 1221–1224, 2015.

Lauderdale, J. M., S. Dutkiewicz, R. G. Williams, and M. J. Follows, Quantifying the drivers of ocean-atmosphere CO_2 fluxes, *Global Biogeochemical Cycles*, *30*(7), 983–999, 2016.

Le Quéré, C., J. C. Orr, P. Monfray, O. Aumont, and G. Madec, Interannual variability of the oceanic sink of CO_2 from 1979 through 1997, *Global Biogeochemical Cycles*, *14*(4), 1247–1265, doi:10.1029/1999GB900049, 2000.

Le Quéré, C., et al., Global carbon budget 2016, *Earth System Science Data*, *8*(2), 605–649, 2016.

Lee, K., et al., An updated anthropogenic CO_2 inventory in the Atlantic Ocean, *Global Biogeochemical Cycles*, *17*(4), 1116, 2003.

Lee, Y.-Y., and R. X. Black, Boreal winter low-frequency variability in CMIP5 models, *Journal of Geophysical Research: Atmospheres*, *118*(13), 6891–6904, 2013.

Lewis, E., D. Wallace, and L. J. Allison, Program developed for co $_2$ system calculations, *Tech. rep.*, Brookhaven National Lab., Dept. of Applied Science, Upton, NY (United States); Oak Ridge National Lab., Carbon Dioxide Information Analysis Center, TN (United States), 1998.

Liss, P., and P. Slater, Flux of gases across the air-sea interface, *Nature*, *247*(5438), 181–184, 1974.

Locarnini, R., A. Mishonov, J. Antonov, T. Boyer, H. Garcia, O. Baranova, M. Zweng, and D. Johnson, *World Ocean Atlas 2009, Volume 1: Temperature, in: NOAA Atlas NESDIS 68*, p. 184 pp, US Government Printing Office, 2010.

Locarnini, R. A., et al., *World Ocean Atlas 2013. Volume 1, Temperature*, vol. 1, NOAA Atlas NESDIS, 2013.

Long, M. C., K. Lindsay, S. Peacock, J. K. Moore, and S. C. Doney, Twentieth-Century oceanic carbon uptake and storage in CESM1 (BGC), *Journal of Climate*, *26*(18), 6775–6800, 2013.

Lüthi, D., et al., High-resolution carbon dioxide concentration record 650,000–800,000 years before present, *Nature*, *453*(7193), 379, 2008.

MacGilchrist, G., A. N. Garabato, T. Tsubouchi, S. Bacon, S. Torres-Valdes, and K. Azetsu-Scott, The Arctic Ocean carbon sink, *Deep Sea Research Part I: Oceanographic Research Papers*, *86*, 39–55, 2014.

Madec, G., *NEMO reference manual, ocean dynamic component: NEMO–OPA*, 27, Note du pôle de modélisation, Institut Pierre Simmon Laplace, France, Institut Pierre Simmon Laplace, France, 2008.

Madec, G., and M. Imbard, A global ocean mesh to overcome the North Pole singularity, *Climate Dynamics*, *12*(6), 381–388, 1996.

Madec, G., P. Delecluse, M. Imbard, and C. Lévy, OPA 8.1 Ocean general circulation model reference manual. Notes du pôle de modélisation de l'IPSL 11, 91 pp, *WWW Page http://www.lodyc.jussieu.fr/opa*, 1998.

Mahowald, N. M., A. R. Baker, G. Bergametti, N. Brooks, R. A. Duce, T. D. Jickells, N. Kubilay, J. M. Prospero, and I. Tegen, Atmospheric global dust cycle and iron inputs to the ocean, *Global biogeochemical cycles*, *19*(4), 2005.

Martin, G., S. Milton, C. Senior, M. Brooks, S. Ineson, T. Reichler, and J. Kim, Analysis and reduction of systematic errors through a seamless approach to modeling weather and climate, *Journal of Climate*, *23*(22), 5933–5957, 2010.

Martin, G. M., et al., The HadGEM2 family of Met Office Unified Model climate configurations, *Geoscientific Model Development*, *4*(3), 723–757, doi:10.5194/gmd-4-723-2011, 2011.

Martin, J. H., G. A. Knauer, D. M. Karl, and W. W. Broenkow, Vertex: carbon cycling in the northeast Pacific, *Deep Sea Research Part A. Oceanographic Research Papers*, *34*(2), 267–285, 1987.

McDougall, T. J., and P. M. Barker, Getting started with TEOS-10 and the Gibbs Seawater (gsw) oceanographic toolbox, *SCOR/IAPSO WG*, *127*, 1–28, 2011.

McGillis, W., J. Edson, J. Hare, and C. Fairall, Direct covariance air-sea CO_2 fluxes, *Journal of Geophysical Research: Oceans (1978–2012)*, *106*(C8), 16,729–16,745, 2001.

McGillis, W. R., et al., Air-sea CO_2 exchange in the equatorial Pacific, *Journal of Geophysical Research: Oceans*, *109*(C8), 2004.

McKinley, G. A., M. J. Follows, and J. Marshall, Mechanisms of air-sea CO_2 flux variability in the equatorial Pacific and the North Atlantic, *Global Biogeochemical Cycles*, *18*(2), 2004.

McKinley, G. A., A. R. Fay, T. Takahashi, and N. Metzl, Convergence of atmospheric and North Atlantic carbon dioxide trends on multidecadal timescales, *Nature Geoscience*, *4*(9), 606–610, 2011.

McKinley, G. A., D. J. Pilcher, A. R. Fay, K. Lindsay, M. C. Long, and N. S. Lovenduski, Timescales for detection of trends in the ocean carbon sink, *Nature*, *530*(7591), 469, 2016.

McKinley, G. A., A. R. Fay, N. S. Lovenduski, and D. J. Pilcher, Natural variability and anthropogenic trends in the ocean carbon sink, *Annual Review of Marine Science*, *9*, 125–150, 2017.

Mehrbach, C., C. Culberson, J. Hawley, and R. Pytkowicx, Measurement of the apparent dissociation constants of carbonic acid in seawater at atmospheric pressure, *Limnology and Oceanography*, *18*(6), 897–907, 1973.

Mémery, L., G. Reverdin, J. Paillet, and A. Oschlies, Introduction to the POMME special section: Thermocline ventilation and biogeochemical tracer distribution in the northeast Atlantic Ocean and impact of mesoscale dynamics, *Journal of Geophysical Research: Oceans*, *110*(C7), doi:10.1029/20005JC002976, 2005.

Millero, F. J., Thermodynamics of the carbon dioxide system in the oceans, *Geochimica et Cosmochimica Acta*, *59*(4), 661–677, 1995.

Millero, F. J., S. Fiol, D. M. Campbell, G. Parrilla, L. J. Allison, and A. Kozyr, Carbon Dioxide, Hydrographic, and Chemical Data Obtained During the R/V Hesperides Cruise in the Atlantic Ocean (WOCE Section A5, July 14 - August 15, 1992), *Tech. rep.*, ORNL/CDIAC-125, NDP-074. Carbon Dioxide Information Analysis Center, Oak Ridge National Laboratory, U.S. Department of Energy, Oak Ridge, Tennessee., doi:10.3334/CDIAC/otg.ndp074, 2000.

Munday, D., H. Johnson, and D. Marshall, Impacts and effects of mesoscale ocean eddies on ocean carbon storage and atmospheric pCO_2, *Global Biogeochemical Cycles*, *28*(8), 877–896, 2014.

Myhre, G., et al., *IPCC, 2013: Climate Change 2013: The Physical Science Basis. Contribution of Working Group I to the Fifth Assessment Report of the Intergovernmental Panel on Climate Change*, chap. 8 Anthropogenic and Natural Radiative Forcing, Cambridge University Press, 2013.

NEMO, NEMO European Consortium Community Ocean Model, `https://www.nemo-ocean.eu/`, 2017.

Nightingale, P. D., G. Malin, C. S. Law, A. J. Watson, P. S. Liss, M. I. Liddicoat, J. Boutin, and R. C. Upstill-Goddard, In situ evaluation of air-sea gas exchange parameterizations using novel conservative and volatile tracers, *Global Biogeochemical Cycles*, *14*(1), 373–387, 2000.

Obata, A., and Y. Kitamura, Interannual variability of the sea-air exchange of CO_2 from 1961 to 1998 simulated with a global ocean circulation-biogeochemistry model, *Journal of Geophysical research*, *108*(C11), 3337, 2003.

Ödalen, M., J. Nycander, K. I. Oliver, L. Brodeau, and A. Ridgwell, The influence of the ocean circulation state on ocean carbon storage and CO_2 drawdown potential in an Earth system model, *Biogeosciences Discussions*, *166*, in review, 2017.

Oeschger, H., U. Siegenthaler, U. Schotterer, and A. Gugelmann, A box diffusion model to study the carbon dioxide exchange in nature, *Tellus*, *27*(2), 168–192, 1975.

Olsen, A., et al., Global Ocean Data Analysis Project version 2 (GLODAPv2) – an internally consistent data product for the world ocean, *Earth System Science Data*, *8*, 297–323, 2016.

Parekh, P., M. J. Follows, and E. A. Boyle, Decoupling of iron and phosphate in the global ocean, *Global Biogeochemical Cycles*, *19*(2), 2005.

Park, G.-H., R. Wanninkhof, S. C. Doney, T. Takahashi, K. Lee, R. A. Feely, C. L. Sabine, J. Triñanes, and I. D. Lima, Variability of global net sea–air CO_2 fluxes over the last three decades using empirical relationships, *Tellus B*, *62*(5), 352–368, 2010.

Peltola, E., R. Wanninkhof, R. Molinari, B. Huss, et al., Chemical and hydrographic measurements from the NOAA/OACES I8 repeat section. ERL AOML-34, *Tech. rep.*, NOAA/OACES, 1998.

Peltola, E., et al., Inorganic and Organic Carbon, Nutrient, and Oxygen Data from the R/V Ronald H. Brown Repeat Hydrography Cruise in the Atlantic Ocean: CLIVAR CO2 Section A16N2003a (4 June-11 August, 2003), ed. A. Kozyr, *ORNL/CDIAC-149, NDP-085. Carbon Dioxide Information Analysis Center, Oak Ridge Natl. Lab., US Dep. of Energy, Oak Ridge, Tenn., doi*, *10*, doi:10.3334/CDIAC/otg.ndp085, 2005.

Prather, M. J., C. D. Holmes, and J. Hsu, Reactive greenhouse gas scenarios: Systematic exploration of uncertainties and the role of atmospheric chemistry, *Geophysical Research Letters*, *39*(9), 2012.

Prytherch, J., M. J. Yelland, R. W. Pascal, B. I. Moat, I. Skjelvan, and M. A. Srokosz, Open ocean gas transfer velocity derived from long-term direct measurements of the CO_2 flux, *Geophysical Research Letters*, *37*(23), 2010.

Rasmussen, S. O., et al., A new Greenland ice core chronology for the last glacial termination, *Journal of Geophysical Research: Atmospheres*, *111*(D6), doi:10.1029/2005JD006079, 2006.

Regnier, P., et al., Anthropogenic perturbation of the carbon fluxes from land to ocean, *Nature Geoscience*, *6*(8), 597–607, 2013.

Repeta, D. J., Chemical characterization and cycling of dissolved organic matter, *Biogeochemistry of Marine Dissolved Organic Matter*, pp. 21–63, 2015.

Riahi, K., S. Rao, V. Krey, C. Cho, V. Chirkov, G. Fischer, G. Kindermann, N. Nakicenovic, and P. Rafaj, RCP 8.5—A scenario of comparatively high greenhouse gas emissions, *Climatic Change*, *109*(1-2), 33–57, 2011.

Ridgwell, A., and S. Arndt, Why dissolved organics matter: DOC in ancient oceans and past climate change, *Biogeochemistry of Marine Dissolved Organic Matter, edited by: Hansell, DA and Carlson, CA, Elsevier, Amsterdam*, 2015.

Ridgwell, A., and R. E. Zeebe, The role of the global carbonate cycle in the regulation and evolution of the Earth system, *Earth and Planetary Science Letters*, *234*(3), 299–315, 2005.

Rödenbeck, C., R. Keeling, D. C. E. Bakker, N. Metzl, A. Olsen, C. Sabine, and M. Heimann, Global surface-ocean pCO_2 and sea–air CO_2 flux variability from an observation-driven ocean mixed-layer scheme, *Ocean Science*, *9*(2), 193–216, 2013.

Rödenbeck, C., D. C. E. Bakker, N. Metzl, A. Olsen, C. Sabine, N. Cassar, F. Reum, R. Keeling, and M. Heimann, Interannual sea–air CO_2 flux variability from an observation-driven ocean mixed-layer scheme, *Biogeosciences*, *11*, 4599–4613, 2014.

Rödenbeck, C., et al., Data-based estimates of the ocean carbon sink variability–first results of the Surface Ocean pCO_2 Mapping Intercomparison (SOCOM), *Biogeosciences*, *12*, 7251–7278, 2015.

Sabbaghzadeh, B., R. Upstill-Goddard, R. Beale, R. Pereira, and P. Nightingale, The Atlantic Ocean surface microlayer from 50 °N to 50 °S is ubiquitously enriched in surfactants at wind speeds up to 13 ms^{-1}, *Geophysical Research Letters*, *44*(6), 2852–2858, 2017.

Sabine, C. L., et al., The oceanic sink for anthropogenic CO_2, *Science*, *305*(5682), 367–371, 2004.

Sanders, R., et al., The biological carbon pump in the North Atlantic, *Progress in Oceanography*, *129*, 200–218, 2014.

SAVE, Chemical, Physical, and CTD Data Report, Leg 1, 23 November 1987 - 13 December 1987, Leg 2 18 December 1987 - 23 January 1988, Leg 3 29 January 1988 - 7 March 1988, *Sio reference 92-9, odf pub. no. 231, 729pp.*, SIO/ODF UCSD, 1992.

Schuster, U., et al., Measurements of total alkalinity and inorganic dissolved carbon in the Atlantic Ocean and adjacent Southern Ocean between 2008 and 2010, *Earth System Science Data*, *6*(1), 175–183, 2014.

Smeed, D., et al., Observed decline of the Atlantic meridional overturning circulation 2004–2012, *Ocean Science*, *10*(1), 29–38, 2014.

Solomon, S., D. Qin, M. Manning, Z. Chen, M. Marquis, K. Averyt, M. Tignor, and H. M. (eds) (Eds.), *Climate Change 2007-The Physical Science Basis: Working Group I Contribution to the Fourth Assessment Report of the IPCC*, Cambridge University Press, Cambridge, United Kingdom and New York, NY, USA, 2007.

Sutton, A. J., R. A. Feely, C. L. Sabine, M. J. McPhaden, T. Takahashi, F. P. Chavez, G. E. Friederich, and J. T. Mathis, Natural variability and anthropogenic change in equatorial pacific surface ocean pCO_2 and pH, *Global Biogeochemical Cycles*, *28*(2), 131–145, 2014.

Sutton, A. J., R. Wanninkhof, C. L. Sabine, R. A. Feely, M. F. Cronin, and R. A. Weller, Variability and trends in surface seawater pCO_2 and CO_2 flux in the Pacific Ocean, *Geophysical Research Letters*, *44*(11), 5627–5636, 2017.

Sweeney, C., E. Gloor, A. R. Jacobson, R. M. Key, G. McKinley, J. L. Sarmiento, and R. Wanninkhof, Constraining global air-sea gas exchange for CO_2 with recent bomb 14C measurements, *Global Biogeochemical Cycles*, *21*(2), 2007.

Takahashi, T., S. C. Sutherland, D. W. Chipman, J. G. Goddard, C. Ho, T. Newberger, C. Sweeney, and D. Munro, Climatological distributions of pH, pCO_2, total CO_2, alkalinity, and $CaCO_3$ saturation in the global surface ocean, and temporal changes at selected locations, *Marine Chemistry*, *164*, 95–125, 2014.

Takahashi, T., et al., Climatological mean and decadal change in surface ocean pCO_2, and net sea-air CO_2 flux over the global oceans, *Deep Sea Research Part II: Topical Studies in Oceanography*, *56*(8-10), 554 – 577, doi:http://dx.doi.org/10.1016/j.dsr2.2008.12.009, 2009.

Taucher, J., and A. Oschlies, Can we predict the direction of marine primary production change under global warming?, *Geophysical Research Letters*, *38*(2), 2011.

Taylor, K. E., R. J. Stouffer, and G. A. Meehl, An overview of CMIP5 and the experiment design, *Bulletin of the American Meteorological Society*, *93*(4), 485–498, 2012.

Thomas, H., A. Friederike Prowe, I. D. Lima, S. C. Doney, R. Wanninkhof, R. J. Greatbatch, U. Schuster, and A. Corbière, Changes in the North Atlantic Oscillation influence CO_2 uptake in the North Atlantic over the past 2 decades, *Global Biogeochemical Cycles*, *22*(4), 2008.

Thoning, K., D. R. Kitzis, and A. Crotwell, *Atmospheric Carbon Dioxide Dry Air Mole Fractions from quasi-continuous measurements at Mauna Loa, Hawaii.*, 2014-08 ed., National Oceanic and Atmospheric Administration (NOAA), Earth System Research Laboratory (ESRL), Global Monitoring Division (GMD), Boulder, Colorado, USA, doi:10.7289/V54X55RG, 2014.

Timmermann, R., H. Goosse, G. Madec, T. Fichefet, C. Ethe, and V. Duliere, On the representation of high latitude processes in the ORCA-LIM global coupled sea ice–ocean model, *Ocean Modelling*, *8*(1), 175–201, 2005.

Turk, D., M. J. McPhaden, A. J. Busalacchi, and M. R. Lewis, Remotely sensed biological production in the equatorial Pacific, *Science*, *293*(5529), 471–474, 2001.

Uchida, H., M. Fukasawa, and A. Murata, WHP P6, A10, I3/I4 Revisit Data Book Blue Earth Global Expedition 2003 (BEAGLE2003) Volume 1,2., *Tech. rep.*, JAMSTEC, 2005.

van Heuven, S., D. Pierrot, J. Rae, E. Lewis, and D. Wallace, *MATLAB Program Developed for CO_2 System Calculations. ORNL/CDIAC-105b.*, Carbon Dioxide Information Analysis Center, Oak Ridge National Laboratory, US Department of Energy, Oak Ridge, Tennessee, 2011a.

van Heuven, S. M., M. Hoppema, O. Huhn, H. A. Slagter, and H. J. de Baar, Direct observation of increasing CO_2 in the Weddell Gyre along the Prime Meridian during 1973–2008, *Deep Sea Research Part II: Topical Studies in Oceanography*, *58*(25-26), 2613–2635, 2011b.

Volk, T., and M. I. Hoffert, *The Carbon Cycle and Atmospheric CO_2: Natural Variations Archean to Present*, chap. Ocean carbon pumps: Analysis of relative strengths and efficiencies in ocean-driven atmospheric CO_2 changes, pp. 99–110, American Geophysical Union, Washington, D. C, 1985.

Wang, C., L. Zhang, S.-K. Lee, L. Wu, and C. R. Mechoso, A global perspective on CMIP5 climate model biases, *Nature Climate Change*, *4*(3), 201, 2014.

Wang, X., R. Murtugudde, E. Hackert, J. Wang, and J. Beauchamp, Seasonal to decadal variations of sea surface pCO2 and sea-air CO_2 flux in the equatorial oceans over 1984–2013: A basin-scale comparison of the pacific and atlantic oceans, *Global Biogeochemical Cycles*, *29*(5), 597–609, 2015.

Wanninkhof, R., Relationship between wind speed and gas exchange over the ocean, *Journal of Geophysical Research: Oceans (1978–2012)*, *97*(C5), 7373–7382, 1992.

Wanninkhof, R., Relationship between wind speed and gas exchange over the ocean revisited, *Limnology and Oceanography: Methods*, *12*(6), 351–362, 2014.

Wanninkhof, R., S. C. Doney, T. Takahashi, and W. R. McGillis, The effect of using time-averaged winds on regional air-sea CO_2 fluxes, *Gas transfer at water surfaces*, pp. 351–356, 2002.

Wanninkhof, R., W. E. Asher, D. T. Ho, C. Sweeney, and W. R. McGillis, Advances in quantifying air-sea gas exchange and environmental forcing, *Annual Review of Marine Science*, *1*, 213–244, 2009.

Wanninkhof, R., S. C. Doney, J. L. Bullister, N. M. Levine, M. Warner, and N. Gruber, Detecting anthropogenic CO_2 changes in the interior Atlantic Ocean between 1989 and 2005, *Journal of Geophysical Research: Oceans (1978–2012)*, *115*(C11), 2010.

Wanninkhof, R., et al., Global ocean carbon uptake: magnitude, variability and trends, *Biogeosciences*, *10*(3), 1983–2000, doi:10.5194/bg-10-1983-2013, 2013.

Watanabe, Y. W., T. Ono, K. Harada, and M. Fukasawa, A preliminary study of oceanic bomb radiocarbon inventory in the North Pacific during the last two decades, *Journal of oceanography*, *55*(6), 705–716, 1999.

Weiss, A., J. Kuss, G. Peters, and B. Schneider, Evaluating transfer velocity-wind speed relationship using a long-term series of direct eddy correlation CO_2 flux measurements, *Journal of Marine Systems*, *66*(1), 130–139, 2007.

Weiss, R., Carbon dioxide in water and seawater: the solubility of a non-ideal gas, *Marine Chemistry*, *2*(3), 203–215, 1974.

Welch, P., The use of Fast Fourier Transform for the estimation of power spectra: a method based on time averaging over short, modified periodograms, *IEEE Transactions on Audio and Electroacoustics*, pp. 70–73, 1967.

Williams, R. G., and M. J. Follows, *Ocean Dynamics and the Carbon Cycle: Principles and Mechanisms*, chap. 11: Cycling and Transport of Nutrients and Carbon, pp. 280–287, Cambridge University Press, Cambridge, United Kingdom and New York, NY, USA, 2011.

WOCE, WOCE observations 1990-1998; a summary of the WOCE global data resource. woce report no. 179/02, *Tech. rep.*, WOCE International Project Office, Southampton, UK, 2003.

Wolf-Gladrow, D. A., R. E. Zeebe, C. Klaas, A. Körtzinger, and A. G. Dickson, Total alkalinity: The explicit conservative expression and its application to biogeochemical processes, *Marine Chemistry*, *106*(1), 287–300, 2007.

Woolf, D. K., Parametrization of gas transfer velocities and sea-state-dependent wave breaking, *Tellus B*, *57*(2), 87–94, 2005.

Yool, A., E. Popova, and T. Anderson, MEDUSA-1.0: a new intermediate complexity plankton ecosystem model for the global domain, *Geoscientific Model Development*, *4*(2), 381–417, 2011.

Yool, A., E. Popova, and T. Anderson, MEDUSA-2.0: an intermediate complexity biogeochemical model of the marine carbon cycle for climate change and ocean acidification studies, *Geoscientific Model Development*, *6*, 1767–1811, 2013a.

Yool, A., E. Popova, A. Coward, D. Bernie, and T. Anderson, Climate change and ocean acidification impacts on lower trophic levels and the export of organic carbon to the deep ocean, *Biogeosciences*, *10*, 5831–5854, 2013b.

Yool, A., E. Popova, and A. Coward, Future change in ocean productivity: Is the Arctic the new Atlantic?, *Journal of Geophysical Research: Oceans*, *120*(12), 7771–7790, 2015.

Yool, A., A. P. Martin, T. R. Anderson, B. J. Bett, D. O. Jones, and H. A. Ruhl, Big in the benthos: Future change of seafloor community biomass in a global, body size-resolved model, *Global Change Biology*, *23*(9), 3554–3566, 2017.

Zweng, M. M., et al., *World Ocean Atlas 2013. Volume 2, Salinity*, p. 39 pp, NOAA Atlas NESDIS, U.S. Government Printing Office, Washington, D.C., 2013.